UNIVERSITÀ DEGLI STUDI DI GENOVA

DOCTORAL THESIS

A Scenario-Based Eulerian–Lagrangian Framework for the Management of Semi-Enclosed Basins

---

Author:
Mattia SCOVENNA

Supervisor:
Prof. Giovanni BESIO

A thesis submitted in fulfillment of the requirements
for the degree of Doctor of Engineering

in

Engineering for Marine and Coastal Environments
Dipartimento di Ingegneria Civile, Chimica, Ambientale

April 15, 2026

Declaration of Authorship

I, Mattia SCOVENNA, declare that this thesis titled, "A Scenario-Based Eulerian–Lagrangian Framework for the Management of Semi-Enclosed Basins" and the work presented in it are my own. I confirm that:

- This work was done wholly or mainly while in candidature for a research degree at this University.
- Where any part of this thesis has previously been submitted for a degree or any other qualification at this University or any other institution, this has been clearly stated.
- Where I have consulted the published work of others, this is always clearly attributed.
- Where I have quoted from the work of others, the source is always given. With the exception of such quotations, this thesis is entirely my own work.
- I have acknowledged all main sources of help.
- Where the thesis is based on work done by myself jointly with others, I have made clear exactly what was done by others and what I have contributed myself.

Signed:

Date:

UNIVERSITÀ DEGLI STUDI DI GENOVA

Abstract

DICCA
Dipartimento di Ingegneria Civile, Chimica, Ambientale

Doctor of Engineering

A Scenario-Based Eulerian–Lagrangian Framework for the Management of Semi-Enclosed Basins

by Mattia SCOVENNA

Semi-enclosed basins such as lagoons and harbors are often ecologically or economically valuable, yet they are characterised by weak water exchange with the open sea and a high sensitivity to contamination. This thesis proposes an end-to-end methodology to support their management and protection, linking long-term metocean variability, hydrodynamics and pollutant dispersion in a single, scenario-based framework.

The approach begins by condensing a multi-decadal hindcast of wind and waves into a limited number of representative metocean scenarios using clustering techniques. These scenarios are then used to drive three-dimensional hydrodynamic simulations, whose velocity fields feed Lagrangian particle tracking models for passive tracers and, in one case, for oil and hazardous and noxious substances. Single- and multiple-particle statistics are applied to the resulting trajectories to quantify water renewal, retention and mixing over a range of spatial and temporal scales.

The methodology is applied to two contrasting semi-enclosed systems: a coastal lagoon and a large commercial port. In the lagoon, results reveal extremely limited connectivity with the open sea, with water renewal largely controlled by wind rather than tides. Simulations of lagoon-wide releases and of a sewage plume both indicate a strong tendency to retain tracers, underscoring the system's vulnerability to nutrient and contaminant accumulation. In the port, spills released at accident-prone locations frequently remain confined within the harbour for days, as basin geometry and local circulation favour trapping over export.

Overall, the thesis shows that a library of precomputed metocean–hydrodynamic scenarios, coupled with Lagrangian diagnostics, can provide a practical and transferable tool to assess flushing, retention and contamination risk in semi-enclosed basins, supporting both contingency planning and informed environmental management.

Contents

List of Figures

List of Tables

List of Abbreviations

ACF	**A**uto**C**orrelation **Function CPA**
Centred **P**eak **A**lgorithm	
ETA	**E**stimated **T**ime of **A**rrival
FSLE	**F**inite **S**ize **L**yapunov **E**xponent
HH	**H**anna–**H**einold statistic
HNS	**H**azardous and **N**oxious **S**ubstances
MDA	**M**aximum **D**issimilarity **A**lgorithm
NCLS	**N**ormalized **C**umulative **L**agrangian **S**eparation
NRMSE	**N**ormalized **R**oot **M**ean **S**quare **E**rror
PTM	**P**article **T**racking **M**odel
SS	**S**kill **S**core
WUI	**W**eb **U**ser **I**nterface

Physical Constants

Gravitational acceleration	$g = 9.81\,\mathrm{m\,s^{-2}}$
Reference seawater density	$\rho_0 = 1025\,\mathrm{kg\,m^{-3}}$
Air density	$\rho_a = 1.225\,\mathrm{kg\,m^{-3}}$
Chezy bottom-friction coefficient	$C_{2D} = 65\,\mathrm{m^{1/2}/s}$
Turbulence constant (k–ϵ)	$C_\mu = 0.09$

List of Symbols

C_{2D}	$\mathrm{m^{1/2}\,s^{-1}}$	Chézy coefficient for bottom friction
C_D	–	Air–sea drag coefficient for wind stress
C_d	–	Windage coefficient
C_μ	–	Empirical constant in k–ϵ closure
C_s	–	Smagorinsky coefficient for sub-grid diffusivity
d	m	Still-water depth
g	$\mathrm{m\,s^{-2}}$	Gravitational acceleration
H_s	m	Significant wave height
k	$\mathrm{m^2\,s^{-2}}$	Turbulent kinetic energy (in k–ϵ model)
ϵ	$\mathrm{m^2\,s^{-3}}$	Dissipation rate of turbulent kinetic energy
ν_t	$\mathrm{m^2\,s^{-1}}$	Turbulent (eddy) viscosity
$R_\pm$	$\mathrm{m\,s^{-1}}$	Riemann invariants at the open boundary
τ_b	$\mathrm{N\,m^{-2}}$	Bottom stress vector
τ_s	$\mathrm{N\,m^{-2}}$	Surface wind stress vector
u, v	$\mathrm{m\,s^{-1}}$	Horizontal velocity components (eastward, northward)
u_{10}	$\mathrm{m\,s^{-1}}$	Wind speed at 10 m above sea level
$\boldsymbol{U}_b$	$\mathrm{m\,s^{-1}}$	Depth-averaged horizontal velocity vector near the bed
U_n	$\mathrm{m\,s^{-1}}$	Depth-averaged velocity normal to an open boundary
w	$\mathrm{m\,s^{-1}}$	Vertical velocity component
ζ	m	Free-surface elevation
ρ_0	$\mathrm{kg\,m^{-3}}$	Reference water density
ρ_a	$\mathrm{kg\,m^{-3}}$	Air density
θ_w	deg	Mean wave direction
T_p	s	Peak wave period

C_D	–	Wind drag coefficient used in the Lagrangian model
Δt	s	Time step for Lagrangian integration
$\Delta x, \Delta y$	m	Horizontal grid spacing in x and y
K	$\mathrm{m^2\,s^{-1}}$	Horizontal diffusion coefficient (Smagorinsky parametrisation)
N_p	–	Number of particles in a simulation
$\boldsymbol{R}$	–	Random vector with components $\mathcal{N}(0,1)$
$\boldsymbol{u}(\boldsymbol{x}, t)$	$\mathrm{m\,s^{-1}}$	Advecting velocity at particle position
$\boldsymbol{v}_c$	$\mathrm{m\,s^{-1}}$	Current velocity vector
$\boldsymbol{v}_w$	$\mathrm{m\,s^{-1}}$	10 m wind velocity vector
$\boldsymbol{x}(t)$	m	Particle position vector at time t

A	$\mathrm{m^2}$	Slick surface area (oil/HNS–water interface)
C_i^s	$\mathrm{mol\,m^{-3}}$	Solubility of pure component i in water
C_i^w	$\mathrm{mol\,m^{-3}}$	Concentration of component i in the water phase
ΔF	–	Increment of evaporated fraction over Δt
F	–	Evaporated mass fraction
K_d	$\mathrm{m\,s^{-1}}$	Dissolution mass-transfer coefficient
k_e	$\mathrm{m\,s^{-1}}$	Mass-transfer coefficient for evaporation

$n_{i,d}$	mol	Dissolved moles of component i in the water phase
T	°C	Environmental (air or water) temperature
T_0, T_G	°C	Distillation-related constants in the Stiver–Mackay model
V_0	m^3	Initial spilled volume of oil (or HNS)
x_i	–	Mole fraction of component i in the oil phase
$A^2(t)$	m^2	Absolute dispersion
c	–	FSLE amplification factor ($r \to cr$)
FSLE	s^{-1}	Finite-Size Lyapunov Exponent (scalar notation)
$K(r)$	$m^2\ s^{-1}$	Scale-dependent relative diffusivity
$\boldsymbol{r}$	m	Separation between two particles
r_0	m	Initial separation between a particle pair
T_L	s	Lagrangian decorrelation time
τ	s	First-passage time for a pair to grow from r_0 to cr_0
$\lambda(r)$	s^{-1}	Finite-Size Lyapunov Exponent at scale r
HH	–	Hanna–Heinold statistic
n	–	Number of data points in a time series
N_i	–	Number of time steps in trial i
NRMSE	–	Normalized Root Mean Squared Error
p	–	Exponent in the weighting function $w_i = N_i SS_i^p$
ρ	–	Pearson correlation coefficient
Skill	–	Skill score relative to mean-observation baseline
σ_η	m	Standard deviation of observed water level
σ_w	m	Standard deviation of modeled water level
SS_i	–	Skill score for trial i (drifter calibration)
v_i	–	Weight assigned to trial i in drag calibration
w_i (water level)	m	Modeled water level at time step i
$\bar{w}$	m	Mean modeled water level
$\bar{\eta}$	m	Mean observed water level
η_i	m	Observed water level at time step i

Introduction

The growing awareness of the critical state of the oceans has highlighted the need for effective strategies to protect and restore marine ecosystems, and to promote a more sustainable relationship with the ocean. Planning the protection of the marine environment requires a clear understanding of how water masses move and how this motion influences the transport and spreading of substances in the ocean, from nutrients to pollutants. In this context, the literature on global- and regional-scale studies is extensive and diverse. It includes work on the dispersion of pollutants such as plastics (Huck et al., 2022; Hardesty et al., 2017; Van Sebille, England, and Froyland, 2012) and oil (French-McCay et al., 2021; Ainsworth et al., 2021; Abascal et al., 2010), the behaviour and dispersal of marine organisms such as juvenile sea turtles (Le Gouvello et al., 2024; Gaspar and Lalire, 2017; Putman et al., 2014) and tuna-like fish (Lehodey, Senina, and Murtugudde, 2008), the transport of eggs and larvae (Palatella et al., 2014), and coral reef connectivity (Wang et al., 2022), among many other topics.

Large-scale studies are generally very robust, as we now have a relatively high level of confidence in the main mesoscale structures of the global ocean. However, they are typically based on coarse spatial resolutions, at which small-scale dynamics are not explicitly resolved. By contrast, local-scale studies (few kilometers in size) introduce additional complexity by explicitly representing the interaction of currents with the coastline, bathymetry and small-scale features. These studies are essential to support the conservation and management of specific environments, such as lagoons, estuaries and ports. Because the interaction between currents and topography plays a primary role in shaping local circulation, each coastal area has its own peculiarities and behaves differently from others, so a specific local assessment is required.

A particularly relevant class of coastal environments is that of semi-enclosed basins, characterized by a limited exchange of water with the open sea, which makes them especially sensitive to external pressures. These transitional ecosystems frequently serve as natural nurseries for fish, breeding grounds for birds, and refuges for both aquatic and terrestrial organisms. Beyond their ecological significance, semi-enclosed basins also offer critical ecosystem services, such as nutrient cycling, water purification, carbon sequestration and natural protection against coastal erosion, which are essential not only for biodiversity conservation but also for the well-being of adjacent human populations (Pérez-Ruzafa and Concepción, 2012; Newton et al., 2018; Pérez-Ruzafa et al., 2019; D'Alpaos and D'Alpaos, 2021; El Mahrad, Newton, and Murray, 2022).

Because they concentrate valuable resources and services, semi-enclosed basins are also subject to intense human use and, consequently, strong anthropogenic pressures. Anthropogenic activities such as fisheries, tourism, agriculture and maritime transport play a central role in the economies and livelihoods of coastal populations, but they also act as major drivers of environmental stress in these ecosystems (Neumann et al., 2015). As a result, today semi-enclosed basins are increasingly threatened by pollution, eutrophication, habitat loss and degradation, and overexploitation of resources (Raicevich et al., 2018).

Lagoons are a prime example of such environments. These coastal systems are among the most dynamic and ecologically valuable, providing critical habitats for a wide range of species and sustaining high biodiversity. Similarly, ports are semi-enclosed environments in which local hydrodynamics are strongly influenced by the configuration of man-made structures. They are vital to coastal economies but are also recognized as hotspots for marine pollution, given the intensity of maritime traffic, industrial operations and frequent small-scale discharges that collectively degrade water quality. It is estimated that 31% of oil spills from large tankers, and up to 44% for medium and small tankers, occur during routine port operations such as loading, unloading and bunkering (Chen et al., 2019). Moreover, previous studies have shown that the frequency of port-related accidents is increasing, as port infrastructure upgrades have failed to keep pace with rising vessel sizes and marine traffic volumes driven by economies of scale (EMSA, 2025; Abreu et al., 2019; Darbra and Casal, 2004), making ports handling oil and chemical cargo especially vulnerable (Polinov, Bookman, and Levin, 2021).

Both lagoons and ports require continuous monitoring and management efforts to ensure that water exchange with the open sea effectively promotes water renewal. Inadequate water exchange can lead to eutrophication, habitat degradation and a loss of ecological resilience (Martín et al., 2020). Conversely, efficient exchange promotes the flushing of excess nutrients and contaminants, supporting the ecological balance and stability of the system. However, management needs may differ depending on the type of pressure. Following an accidental pollutant release, for example, longer retention times may increase local ecological damage but at the same time limit the spatial extent of contamination by confining it to a smaller area. Ports are typically less rich in biodiversity than lagoons, but as continuous sources of pollution they can easily affect the surrounding marine environment. For ports, therefore, the focus often shifts towards designing targeted and rapid contingency plans to limit the impact of accidental spills. In this context, depending on the scenario, efficient exchange can be desirable to renew port waters, but in some cases limited exchange may help contain contaminants (Kjerfve and Magill, 1989; Alba et al., 2014; Umgiesser et al., 2014; Fiandrino et al., 2017; Lambert and Solari, 2022).

Regardless of the spatial scale of the domain under study, or wether the domain benefits from a rapid or slow flushing rate, the transport mechanisms governing the movement of water are investigated using a Lagrangian perspective. By following the trajectories of individual particles, this approach is particularly well suited to capture the dynamics that control transport in complex coastal environments. Knowing the position of particles at any time opens up a wide range of diagnostic tools that are not accessible from a purely Eulerian point of view. The Eulerian approach describes quantities at fixed locations, providing snapshots of concentration fields, whereas the Lagrangian approach reconstructs the history of each particle. This makes it possible, for example, to identify preferential transport pathways, quantify residence and exposure times, and characterize the spatial and temporal scales of motion.

Nevertheless, studying the fate of particles in the sea is only possible if the underlying ocean circulation is known, and ocean currents are typically described in an Eulerian framework. For this reason, a modeling chain that couples a hydrodynamic (Eulerian) model with a Lagrangian Particle Tracking Model (PTM) has become the standard approach to investigate how currents transport substances in the ocean.

The implementation of a hydrodynamic model requires knowledge of all the environmental variables that play a role in generating ocean currents, including tides, wind, waves and large-scale circulation. These variables can come from two main sources: measurements and numerical models. Direct measurements can be gathered using oceanographic buoys. For example, ODAS (Ocean Data Acquisition System) buoys are equipped with a wide range of sensors and can provide accurate metocean information with high temporal resolution, but only at single points in space. Given that coastal hydrodynamic models are normally forced along open boundaries, such point-wise data limit the use of buoys for boundary condition specification. A similar limitation arises when combining different instruments, such as ADCPs (for waves and currents) and meteorological stations (for wind), which again provide sparse spatial coverage.

An alternative to direct measurements is the use of global or regional numerical models. However, because of their coarse resolution, data from these models cannot be directly used for local-scale studies. It is therefore necessary to increase the effective spatial resolution through downscaling techniques. By nesting high-resolution coastal models within coarser regional models and interpolating the large-scale outputs to the local model boundaries, global and regional products can be used to force coastal simulations (see, e.g., Ferrari et al., 2020). In this way, the large-scale circulation and metocean conditions are consistently transferred to the local domain.

Another fundamental aspect concerning boundary conditions is the choice of strategy for local-scale simulations. Two main methodologies can be identified: implementing forecasting systems that perform daily, ad hoc simulations based on real-time environmental data (Abascal et al., 2017a; Pisano et al., 2016; Cucco et al., 2012), or building precomputed scenario libraries that capture the full range of metocean variability (Daliri et al., 2025; He et al., 2024; Núñez et al., 2019).

The two approaches address different operational needs and are therefore complementary rather than competing. Forecast-based modeling frameworks are primarily designed for real-time or near–real-time emergency response, where the objective is to predict the evolution of a specific ongoing event under the most up-to-date environmental conditions. In this context, the continuous ingestion of atmospheric and oceanic forecasts and the on-demand execution of hydrodynamic and dispersion models are essential to support prompt decision-making during accidental releases.

By contrast, the scenario-based approach adopted in this study is intended for mitigation, preparedness, and management planning. Instead of reproducing a specific future event, it aims to characterize the range of circulation patterns and transport pathways that are likely to occur under representative metocean conditions. By precomputing a limited but statistically meaningful set of scenarios, the most computationally demanding component, the hydrodynamic simulation, can be performed offline. This enables rapid dispersion assessments through Lagrangian simulations once an event occurs, by selecting the scenario that best matches the prevailing conditions.

While real-time forecasting provides tactical responses to ongoing events, the scenario-based framework provides a strategic assessment of potential environmental risk. By precomputing a library of representative metocean scenarios, we isolate the fundamental transport mechanisms (e.g., windage contribution, retention duration) that are often obscured in real-time forecast outputs. This methodological novelty allows managers to identify 'worst-case' pathways and bottlenecks in flushing before an event occurs, providing a robust tool for site-specific mitigation and infrastructure planning.

This strategy is particularly well suited to semi-enclosed and sensitive environments. In ports, accurate dispersion modeling requires high spatial resolution and the combined effects of wind, waves, tides, and regional circulation, making real-time forecasting complex and resource-intensive. In lagoons, where hydrodynamics are often controlled by a smaller set of forcings, primarily wind and tide, and where variability is more constrained, a reduced number of representative scenarios may be sufficient to capture the dominant circulation regimes. In both cases, precomputed scenarios provide a robust and efficient framework for risk awareness, contingency planning, and long-term management, complementing real-time forecasting tools used during emergencies.

Against this backdrop, this study proposes a methodology that captures the essential range of metocean variability while remaining suitable for rapid deployment in coastal environments. A representative set of scenarios is extracted from a 40-year hindcast dataset through clustering approaches and used to drive high-resolution hydrodynamic models. The resulting velocity fields are then used to simulate either passive tracer transport or oil and HNS dispersion, depending on the case study. Finally, statistical post-processing frameworks are implemented to analyse the physical processes that govern water circulation and transport mechanisms in the domains.

This modeling chain is applied to two local-scale case studies: a coastal lagoon (Narta Lagoon) and a commercial port (the Port of Genoa).

Several configurations are considered. For Narta Lagoon, the transport of particles uniformly released inside the lagoon is simulated to estimate the fraction of particles that are able to leave the system under different scenarios. In a second configuration, a cloud of particles is released in a limited area corresponding to the outfall of the sewage system collecting wastewater from the nearby village, in order to assess how such discharges may affect the lagoon. For the Port of Genoa, virtual particles are uniformly released inside the port to investigate its ability to renew its waters under different metocean scenarios. In addition, oil and HNS spills are simulated along the main vessel routes and at two chemical storage sites, to raise awareness of the potential impact of small, routine discharges in port areas.

Along the way, different analyses are presented, including an assessment of the sensitivity of dispersion models to the choice of slip condition at the boundaries, and the calibration of a suitable wind drag coefficient by comparing virtual and observed drifter trajectories inside the port. A full chapter is devoted to the evaluation of mixing properties, using single- and multiple-particle statistics to examine transport mechanisms in greater detail.

The findings are intended to inform targeted management actions and contribute to the preservation of ecologically and culturally significant coastal systems. By integrating hydrodynamic variability, Lagrangian analysis and statistical diagnostics, the proposed framework provides a scalable and operationally adaptable tool to evaluate pollutant transport in semi-enclosed basins. By shifting the computational effort offline through the use of precomputed velocity fields, the proposed approach enables fast, scenario-based dispersion analyses that can effectively support preparedness and management decisions in the event of accidental releases.

The document is structured as follows. Chapter 1 presents the study areas and the data used to implement the models. Chapter 2 describes the general methodology. Chapter 3 defines how and where the boundary conditions used to force the hydrodynamic models are obtained. Chapter 4 presents the hydrodynamic models and the associated post-processing analyses. Chapter 5 describes the PTMs and the statistical tools applied to gain insights from them. Chapter 6 focuses on mixing properties. Finally, Chapter 7 presents the discussion and Chapter 8 the conclusions.

Chapter 1

Study Areas and Data

Semi-enclosed basins, such as coastal lagoons, estuarine embayments and ports, occupy a relatively small fraction of the global ocean surface but play an important ecological and socio-economic role. They are typically characterized by a restricted connection with the open sea, complex coastlines and shallow bathymetry, which together lead to circulation patterns and water exchange markedly different from those of the adjacent shelf. These systems often host productive habitats, serve as nursery areas for many marine species, and support a wide range of human activities, including fisheries, navigation, tourism and urban development. At the same time, their limited flushing capacity makes them particularly sensitive to external pressures such as nutrient enrichment, contaminant inputs and morphological alterations.

From a physical perspective, the weak and geometrically constrained exchange with the open sea implies that local hydrodynamics are strongly controlled by the interplay between tides, wind forcing, and the shape and configuration of inlets and man-made structures. Small changes in forcing or geometry can therefore produce large differences in residence times, pathways of transport and the spatial distribution of tracers. As a result, semi-enclosed basins are prone to long-lasting retention of pollutants and to the development of water quality problems, but they can also, under certain conditions, act as partial buffers that limit the export of contaminants to the wider coastal ocean.

In this context, studying semi-enclosed basins is essential for at least three reasons. First, their ecological and economic value makes them priority areas for conservation and risk reduction, where failures in management have immediate local consequences. Second, their hydrodynamics are highly site-specific: the combination of local morphology, forcing and human modifications means that results from one system cannot be directly transferred to another without dedicated analysis. Third, their confined nature and relatively small spatial scales make them ideal testbeds for the development and application of high-resolution hydrodynamic and Lagrangian models, and for linking physical transport to exposure, impact and support decision-making. The two case studies considered in this thesis, Narta Lagoon and the Port of Genoa, are representative of these issues in two different settings: a shallow, ecologically valuable lagoon with very limited natural exchange, and a large commercial port where engineered structures and intense maritime activity strongly shape circulation and pollutant dispersion.

1.1 Narta Lagoon

Along the Albanian Adriatic coastline, lagoon systems play a prominent ecological, cultural, and socio-economic role. These coastal water bodies, including the Narta

Lagoon, are essential stopover sites for migratory birds and support a variety of ecosystem services, from artisanal fisheries and salt production to tourism and traditional livelihoods (see e.g., Cullaj et al., 2005; Tsujio, Asano, and Hoxha, 2024). Despite their value, Albanian lagoons face escalating pressures from coastal development, pollution, and land-use changes, which highlight the urgency of integrated scientific approaches to support sustainable management (Fraschetti et al., 2011).

The Narta Lagoon is located along the southern Albanian coast, near the coastal city of Vlorë (Figure 1.1, Panels A and B). This area is of considerable interest due to its ecological, historical, and socio-economic value. It hosts the centuries-old Zvernec Monastery, serves as a critical habitat for migratory birds, European eels, and nesting sea turtles, and supports the local economy by providing suitable conditions for fish farming and other economic activities that sustain the livelihoods of over a hundred workers in the region (Elmazi and Bazini, 2011; Kane et al., 2015; Mladenov et al., 2017; Topi, Saliaj, and Mersinaj, 2013).

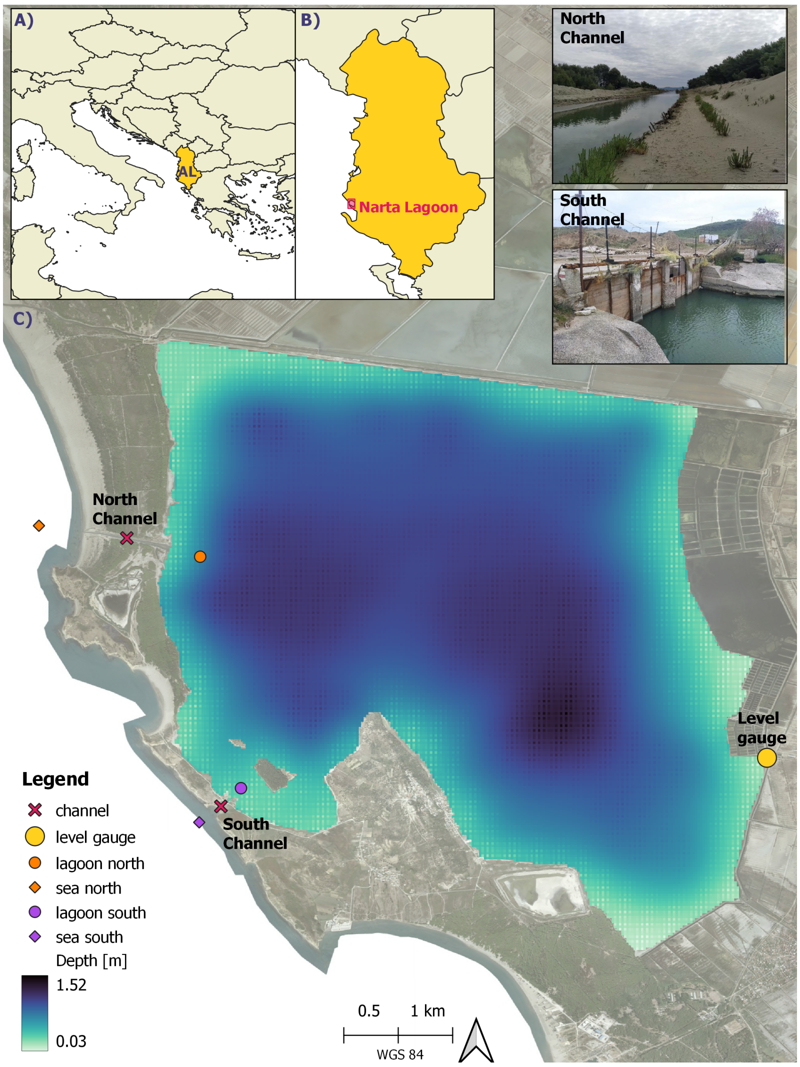

FIGURE 1.1: Panels A and B: Localization of Albania and Narta Lagoon; Panel C: Narta Lagoon bathymetry, localization of MeteOcean level gauge (yellow point) the north and south channels (red crosses), numerical monitoring station (orange and purple circle and diamond). Top right corner: pictures of the north and south channels.

Despite its ecological and cultural significance, the Narta Lagoon is increasingly threatened by various anthropogenic pressures. These include the nearby municipal landfill serving Vlorë and surrounding towns, industrial activities such as salt production and leather tanning (Kane et al., 2015; Çako et al., 2014; Beqaj, 2023; Vaso, Miho, and Alain, 1996), illegal fishing practices (Topi, Saliaj, and Mersinaj, 2013), and the recent construction of a regional airport. Many of these activities are located in close proximity to the lagoon, and their associated wastewater is not always properly treated, raising concerns about contamination through surface runoff and groundwater leaching.

Previous water quality assessments have identified strong seasonal variability in salinity, hypersaline conditions in summer and salinity levels closer to those of the Adriatic Sea in winter, alongside a general tendency toward oligotrophic conditions and overall acceptable physico-chemical parameters (Çomo et al., 2018; Topi, Saliaj, and Mersinaj, 2013; Kane et al., 2015).

At present, the exchange of water between the lagoon and the Adriatic Sea is primarily controlled by two main inlets, which differ significantly in geometry and operational management, as shown in Figure 1.1, Panel C. The southern channel (lon/lat: 19.395647 / 40.514683, WGS84) is approximately 200 meters long and has a minimum width of 10 meters. It is equipped with manually operated sluice gates located at its narrowest point. The northern channel (lon/lat: 19.379781 / 40.545369), in contrast, is longer (about 800 meters) and slightly wider (just over 10 meters), but it is subject to seasonal closure due to sediment accumulation from littoral transport. Local sources report that it is manually reopened by fishermen approximately twice a year (Topi, Saliaj, and Mersinaj, 2013). The operation of these channels is largely unregulated and managed informally by local stakeholders, primarily fishermen. No consistent or scheduled procedures are in place for the opening and maintenance of the inlets, often leading to stagnation and associated ecological stress.

Part of the work carried out in Narta Lagoon was developed within the project "BLUE coAL-ITion: Eco-sustainable Development for Albanian coast-sea natural capital", funded by CELIM (Centro Laici Italiani per le Missioni ONLUS).

1.2 Port of Genoa

Coastal industrial areas and major ports are recognised hotspots for marine pollution, particularly accidental or operational spills of oil and HNS. In semi-enclosed basins such as the Mediterranean Sea, limited water exchange and intense maritime traffic can enhance the persistence and impact of these contaminants on coastal ecosystems and human activities. Within this regional context, the Gulf of Genoa and the Port of Genoa form a key maritime hub in the northwestern Mediterranean, where complex hydrodynamics and dense shipping interact to control the fate and transport of spilled substances.

The Gulf of Genoa is located in the Ligurian Sea (Northwestern Mediterranean) at approximately 44° 4′ 03" N and 8° 86′ 2" E. At the heart of the Gulf lies the Port of Genoa, one of the largest commercial port in the Mediterranean Sea and a major hub for maritime traffic. The port experiences high vessel density, including cargo ships, oil tankers, and passenger ferries, making it a critical area for environmental risk assessment. Due to its strategic importance, understanding pollutant dispersion in this region is essential for mitigating potential hazards associated with shipping activities and industrial operations.

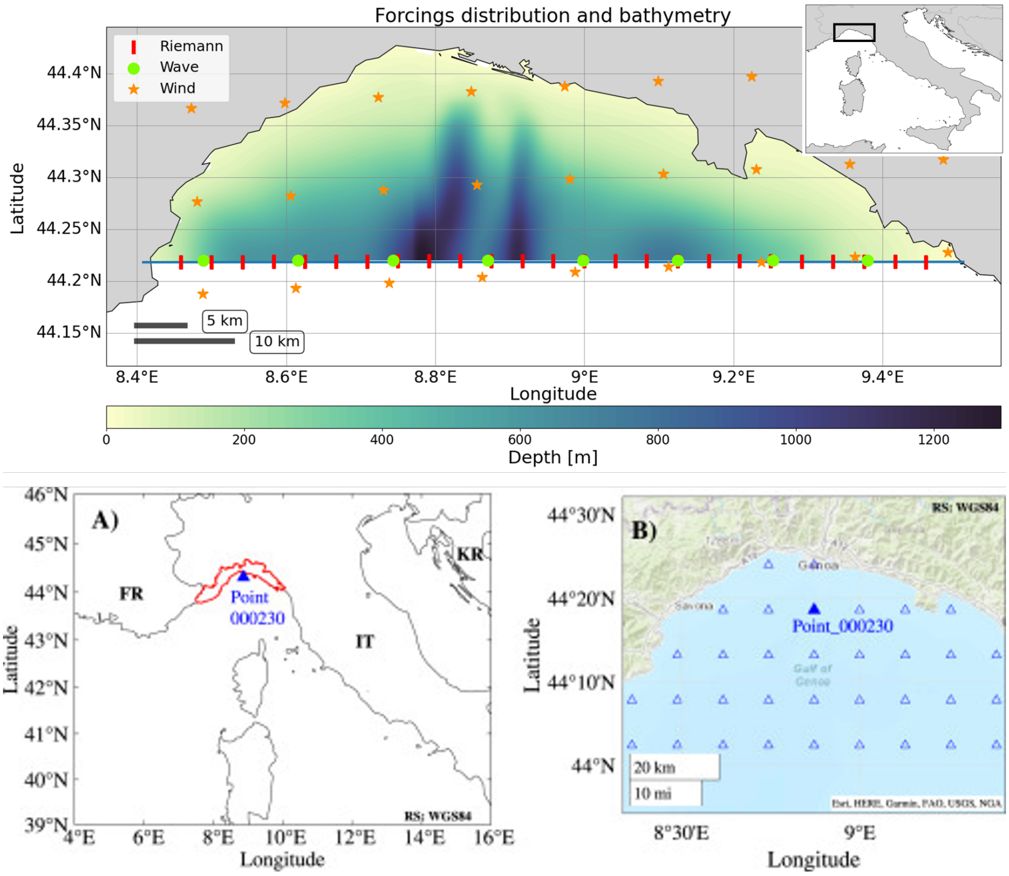

FIGURE 1.2: Top panel: gulf of Genoa bathymetry with the position of the variables used to force the hydrodynamic model. Down panel: A) Ligurian region; B) Hindcast nodes available.

From a hydrodynamic perspective, the upper Tyrrhenian Sea is characterized by complex processes influenced by the combination of tides, winds, waves and large-scale circulation patterns. As part of the Mediterranean Sea, the Gulf is dominated by a semi-diurnal tidal regime, with relatively small tidal amplitudes (Lozanos and Canela, 1995). Circulation is part of the Liguro-Provençal circulation (Molcard et al., 2002; Castellari, Pinardi, and Leaman, 2000), primarily driven by a cyclonic current system, which weakens during summer (Iacono and Napolitano, 2020) and it is locally influenced by seasonal wind variability (Manzella and Esposito, 1982). The dominant winds include northerly Tramontana, enhancing offshore transport, and southerly Libeccio and Scirocco, with Libeccio responsible of generating the most extreme wave events, particularly during winter (Ferrari et al., 2024; Cavaleri et al., 2022; Corrales-Gonzalez, Lavidas, and Besio, 2023). The bathymetry also adds complexity to the system, with steep underwater topography and two prominent submarine canyons located off the coast of Genoa (Figure 1.2). These canyons influence local circulation, acting as pathways for deep water transport and affecting mixing processes (Ramos-Musalem and Allen, 2019; Allen, Somerfield, and Gilbert, 2007).

Within this complex hydrodynamic setting, the port's geometry, with multiple docks, basins, and breakwaters, plays a dominant role in shaping local currents, confinement, and exchange with the outer sea. These features make the Port of Genoa an ideal case study for analyzing dispersion, retention, and renewal processes in semi-enclosed coastal environments.

The oil and HNS spill simulations for the Port of Genoa were developed in the framework of the European project PROMPT (Preparedness for Operational Monitoring and Prediction of contaminant Transport in the Sea). In this thesis, the PROMPT modeling system is used and further exploited to analyse pollutant dispersion and support scenario-based risk assessment.

1.3 Data

1.3.1 Environmental Forcing

The environmental variables used to force Narta lagoon hydrodynamic model are: astronomical tide and wind. Waves are neglected because they cannot propagate into the lagoon through either inlet: the northern channel is too long and shallow, while the southern inlet is constrained by man-made structures. For the same reason, also the regional currents are not taken into account. While Genoa model is forced with: astronomical tide, wind, waves and regional currents. In both cases the sources of the variables are the same. Astronomical tide are extracted from the TPXO global tide model 7.2 (Egbert and Erofeeva, 2002); this model offers global coverage of tidal constituents and is widely used in hydrodynamic simulations of coastal and estuarine systems due to its reliability and resolution. The regional currents are downloaded from Copernicus Marine Service; in this case, the Sea Physics Reanalysis dataset is used (Escudier et al., 2021). Both wind and wave data come from a 40-year hindcast produced by the MeteOcean research group of the University of Genoa (MeteOcean) (Lira-Loarca et al., 2022; Cassola, Ferrari, and Mazzino, 2015; Mentaschi et al., 2013). The hindcast provides data with an hourly resolution and a spatial resolution of ≈10 km, covering the entire Mediterranean area. Finally, the bathymetry data come from GEBCO Compilation Group 2024 (GEBCO, 2024) for the Gulf of Genoa, while for Narta lagoon they are measured as described in §1.3.2.

1.3.2 Bathymetric Surveys

A bathymetric survey of the Narta Lagoon was conducted in October 2021 using a low-cost, portable sonar system (Deeper Smart Sonar CHIRP+; v1.deepersonar.com) in combination with high-precision GNSS-RTK positioning (as recently applied in Casella, Scicchitano, and Rovere, 2024). The sonar device was mounted on a small fishing vessel, which followed pre-defined transects across the lagoon designed to maximize spatial coverage (Figure 1.3). Survey results revealed that the lagoon bathymetry is relatively homogeneous, with minimal bottom elevation variability. Over the majority of the lagoon, depths range between 1.0 and 1.5 meters, gradually decreasing toward the edges, and no significant morphological irregularities were observed (Figure 1.1, Panel C).

1.3.3 Hydrometric analysis

Water levels within the lagoon were continuously monitored from October 2021 to July 2022 (Figure 1.4a). The measurement system was eventually decommissioned due to persistent technical issues related to energy supply at the hosting station.

To isolate possible oscillations associated with tidal forcing, the raw signal was first cleaned by removing spurious spikes and then subjected to a two-day low-pass filter, following recommendations from Ray and Foster (2016). The filtered series, shown in Figure 1.4b, highlights key trends in lagoon levels over the observation period. A pronounced rise occurred in December 2021, with water level increasing

FIGURE 1.3: Bathymetric transects to reconstruct the Narta Lagoon bathymetry.

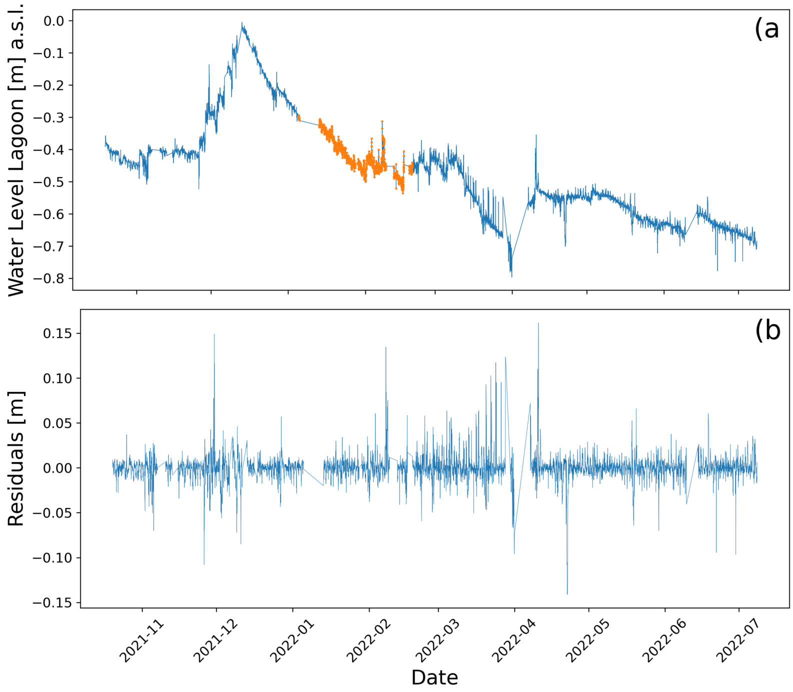

FIGURE 1.4: (a) Time series of observed water levels in the Narta Lagoon. (b) High-pass filtered signal isolating short-term variability. The highlighted segment was selected for autocorrelation analysis.

by nearly 40 cm (from 1.15 m to 1.55 m) due to intense regional precipitation. This was followed by a gradual return to baseline conditions by February 2022. Conversely, a sharp decline in water level occurred starting in March 2022, attributed to the temporary opening of the lagoon inlets, with a recorded minimum in April. After the inlets were closed again, levels rose to approximately 1.0 m, with subsequent fluctuations likely driven by seasonal evaporation and sporadic rainfall during the transition to warmer months.

To explore the potential influence of tidal signals on the water level dynamics, an autocorrelation analysis (ACF) on the residual high-frequency signal was conducted (Figure 1.4b). The ACF quantifies the degree of similarity between the time series and lagged versions of itself and is commonly employed to detect cyclic patterns, such as those arising from tidal forcing (e.g., Ze-Guo Zhang and Liu, 2018; Kareem et al., 2022).

Given the mixed semi-diurnal tidal regime of the Adriatic Sea (Guarnieri et al., 2013), significant autocorrelation at 12-hour intervals (or multiples thereof) would be expected if tidal influence were effectively transmitted into the lagoon. However, as illustrated in Figure 1.5 (right panel), no such periodic signal was identified within any uninterrupted subset of the lagoon's water level data. For comparison, the autocorrelation of the open-sea tide (left panel) shows a clear semi-diurnal signature.

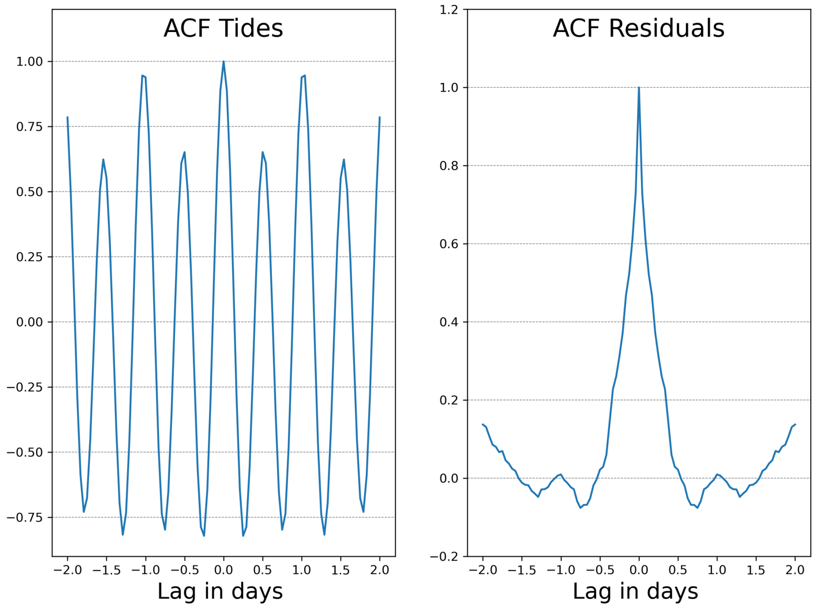

FIGURE 1.5: Autocorrelation functions (ACFs) for (left) sea-level data along the Vlorë coast, and (right) residual water levels inside the Narta Lagoon. The absence of periodicity in the lagoon signal suggests weak tidal influence.

This lack of detectable tidal periodicity suggests two possible scenarios: (i) tidal energy is not transmitted into the lagoon due to the closure or restriction of the connecting channels, or (ii) the strong bottom friction and shallow depths within the lagoon attenuate the tidal signal before it can propagate inward. Given the relatively small mean tidal range ($\sim$ 30 cm), characteristic of a microtidal system, and the known channel configurations, the results point toward limited hydrological exchange between the lagoon and the Adriatic Sea. These observations provide a strong rationale for the numerical modeling approach discussed in subsequent sections.

1.3.4 Calibration and Validation data

To validate Genoa hydrodynamic model, water levels measured inside the port are used. Data are provided by ISPRA and available to the public Marine Monitoring

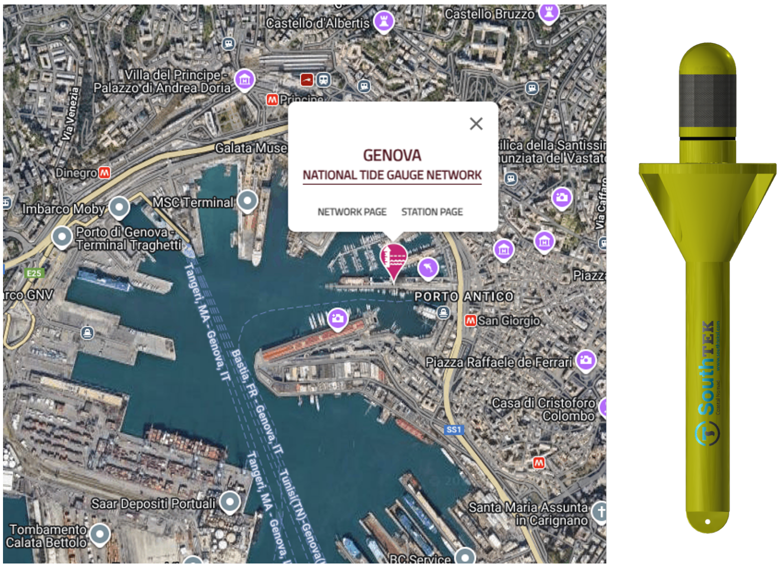

FIGURE 1.6: On the left: location of the gauge station inside the port of Genoa; on the right: drifter used to calibrate the PTM inside the port of Genoa.

Network. The gauge station is placed inside the port (44° 24′ 36.46" N, 8° 55′ 31.86" E, Figure 1.6) and provides the water level every 10 minutes.

Drifters are used to calibrate the PTM, namely the Coastal Nomad drifters from SouthTEK. The Coastal NOMAD is a compact surface drifter designed for short-term experiments in coastal waters under GSM coverage. It is equipped with a multi-GNSS positioning chip that can track up to 32 satellites simultaneously and can use GPS, GLONASS, Galileo and SBAS signals to provide a robust and accurate position.

Chapter 2

Methodology

The overall methodology is summarized in Figure 2.1, where the pink boxes indicate the main steps of the workflow, the yellow boxes represent inputs (on the left) and outputs (on the right), and the green boxes highlight calibration/validation steps, which apply only to the port models.

The process begins with the selection of representative climate scenarios. Based on the assumption that, in a statistical sense, future conditions tend to resemble past ones, a clustering algorithm is applied to a long-term hindcast dataset to extract a reduced set of N representative boundary conditions. This approach captures the dominant metocean variability while significantly reducing computational demands, and provides a structured and reusable dataset for rapid response.

The selected scenarios are then used to force a high-resolution three-dimensional hydrodynamic model. Given that the horizontal length scale is much larger than the vertical one, the model solves the hydrostatic shallow-water Navier–Stokes equations and yields one current velocity field for each scenario. These velocity fields serve as input for two PTMs. The first PTM simulates the dispersion of passive tracers by integrating the advection–diffusion equation governing their motion. For Narta Lagoon, in one configuration virtual particles are released throughout the lagoon to simulate surface tracer dispersion, while in a second configuration particles are released at the location of the sewage system outfall. In the Port of Genoa, virtual particles are uniformly released within the port domain. The second PTM includes a weathering module and is used to simulate oil and HNS spills along the main vessel routes and at two chemical storage sites in the Port of Genoa.

A statistical post-processing is carried out for both study cases. For Narta Lagoon, the lagoon's response to external forcings is examined through: (i) an energetic analysis of the current fields, (ii) the temporal evolution of water levels at both ends of the inlet channels, and (iii) the net water discharge between the lagoon and the sea. To further assess the lagoon's capacity to retain or exchange water masses, the fate of particles released inside the lagoon is tracked to identify their trajectories and quantify the proportion exiting the lagoon through the inlets. For the sewage discharge configuration, the sensitivity of plume dispersal to the release timing is also investigated.

For the Genoa case study, post-processing analyses quantify the influence of the slip condition by evaluating the fraction of virtual particles leaving the port through its main exits with and without slip condition. Then, the Renewal Time map (for passive tracers) measures the time required for water to leave the port. The ensemble of all scenarios is condensed into two key descriptors: (i) the Hazard and (ii) the minimum Estimated Time of Arrival (both for passive tracers and oil and HNS), which, by identifying the coastal areas most exposed to port-related pollution, provide a reference framework for mitigation planning and emergency preparedness.

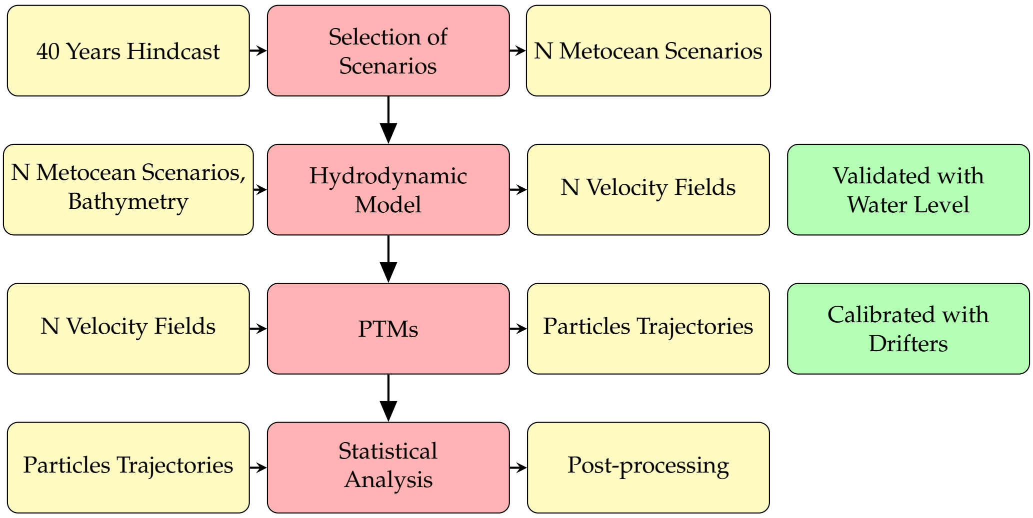

FIGURE 2.1: Methodology proposed: the pink boxes represent the main steps, the yellow the input (on the left) and output (on the right), while the green ones indicates if the process on the same row has been validate.

Finally, single- and multiple-particle statistical descriptors are computed to characterize the spatial and temporal scales of dispersion, highlighting differences among different scenarios and between particles that remain inside or exit the port. These descriptors are applied only to trajectories that do not beach during the simulations.

The combination of Eulerian and Lagrangian diagnostics offers an integrated perspective on flushing dynamics, water retention and the physical vulnerability of the systems under different environmental scenarios. In practical terms, it links the underlying circulation patterns to concrete indicators of exposure, renewal and spill impact, providing information that is directly relevant for management and contingency planning. Because the workflow is scenario-based and relies on precomputed velocity fields, it can be readily transferred to other semi-enclosed basins and used as a fast-response decision-support tool in case of accidental releases.

Chapter 3

Boundary Conditions

As mentioned in the introduction, the approach adopted in this work is based on a pre-defined set of metocean scenarios used to force the hydrodynamic models. This choice is motivated by the overarching goal of the study: to support contingency planning and management decisions in the event of accidental releases in sensitive coastal areas. Working with a finite number N of scenarios extracted from a hindcast dataset means working with the same finite number of representative velocity fields. In practice, this allows the hydrodynamic models, where most of the computational cost lies, to be run once and for all. Thereafter, pollutant dispersion can be simulated efficiently and on demand by running PTMs on the velocity field associated with the scenario that most closely resembles the current metocean conditions. At the same time, analysing dispersive behaviour under the most representative metocean scenarios provides a comprehensive picture of the dominant transport mechanisms within the domain, thereby supporting long-term mitigation and management planning. The temporal window of the scenarios is set to one week. This choice reflects both practical and physical considerations: in case of a spill, response actions are concentrated in the first days following the event, particularly in semi-enclosed environments such as ports and lagoons, and storm events in the Mediterranean typically last only a few days, meaning that weekly scenarios, if properly defined, can eventually cover the whole storm.

Sea currents at local scale are driven by several environmental variables, including tide, wind, waves and large-scale currents. Tides are deterministic, meaning that tidal elevations and phases can be predicted with high accuracy at any location in the ocean for present and future dates. Large-scale currents are resolved by robust regional ocean models, which provide freely available gridded products (see Section 1.3); these can be directly downloaded and used as boundary conditions. In contrast, wind and wave forcing are more challenging, as they exhibit strong spatial and temporal variability and must be described in a way that captures extremes as well as more frequent, moderate conditions.

In this study, wind and wave data are taken from a 40-year hindcast produced by the MeteOcean research group of the University of Genoa (MeteOcean) (Lira-Loarca et al., 2022; Cassola, Ferrari, and Mazzino, 2015; Mentaschi et al., 2013). The hindcast provides hourly data on a grid with a spatial resolution of approximately 10 km, covering the entire Mediterranean Sea (a zoom over the Ligurian Sea is shown in panel B of Figure 1.2).

Different algorithms are employed to extract one-week wind-only scenarios (for the Narta case study) and combined wind–wave scenarios (for the Genoa case study) from the hindcast: the Maximum Dissimilarity Algorithm (MDA) and the Centered Peak Algorithm (CPA). Once the representative weeks have been selected, the corresponding tidal signals (for both Narta and Genoa) and regional currents (for Genoa) are downloaded from the providers described in §1.3. Together, these datasets define the complete set of boundary conditions required to force the hydrodynamic models under a manageable number of metocean scenarios.

3.1 Maximum Dissimilarity Algorithm (Narta Lagoon)

The scenarios for the Narta Lagoon case are selected by applying the Maximum Dissimilarity Algorithm (MDA) (Camus et al., 2011) to the wind hindcast at the grid node closest to the study area, located inside the lagoon, at the position marked by white 'X' in Figure 4.1. The goal of this procedure is to maximize the diversity of the selected events, so as to capture the full range of wind conditions that influence the lagoon hydrodynamics.

The 40-year wind hindcast is first divided into consecutive one-week periods. Each week is then characterized in terms of wind speed and direction, which define its position in a multi-dimensional feature space, defined as the space spanned by the variables used to describe each week. The MDA iteratively selects the weeks that are most dissimilar from those already chosen, starting from the rarest and most extreme events and progressively adding more common situations. In this way, the final set of selected weeks covers the full variability domain of the original dataset. These selected weeks act as centroids, and the remaining weeks are assigned to the cluster associated with their closest centroid.

To determine the optimal number of scenarios, a sensitivity analysis is performed by evaluating the mean inter-centroid distance across clusters. This metric quantifies the average distance, in feature space, between the centroids of different clusters. As the number of clusters increases, the mean inter-centroid distance decreases, indicating that the clusters become less distinct from one another. The ideal number of scenarios is identified at the "elbow" of this curve, where further increasing the number of clusters yields only marginal gains in distinctiveness, thereby balancing variability representation and computational feasibility.

Given the relatively low variability of the regional wind field, the analysis yields six one-week scenarios, which are representative of the most divergent wind conditions within the initial dataset. For each selected scenario, the corresponding tidal signals are derived using the TPXO model, as described in §1.3.

Figures 3.1 and 3.2 show, respectively, the tidal signals and the wind rose plots for each scenario. As expected, the tidal forcing exhibits a mixed semi-diurnal regime, consistent with regional oceanographic conditions along the Albanian coast. The typical tidal range does not exceed 15 cm, placing the system within the micro-tidal classification.

Regarding the wind, scenarios 02, 03, 04 and 06 are characterized by easterly to southeasterly winds, while scenarios 01 and 05 display prevailing northwesterly to southwesterly winds. Given the geographic orientation of Narta Lagoon, with both inlets located along the western shoreline, winds from the east–southeast are expected to enhance outflows from the lagoon toward the Adriatic Sea. Conversely, winds from the west and northwest are likely to promote inflows into the lagoon, pushing marine waters landward through the channels.

3.2 Centered Peak Algorithm (Port of Genoa)

To select the scenarios for Genoa study case, an ad-hoc clustering algorithm is implemented. The clustering procedure uses significant wave height as the primary

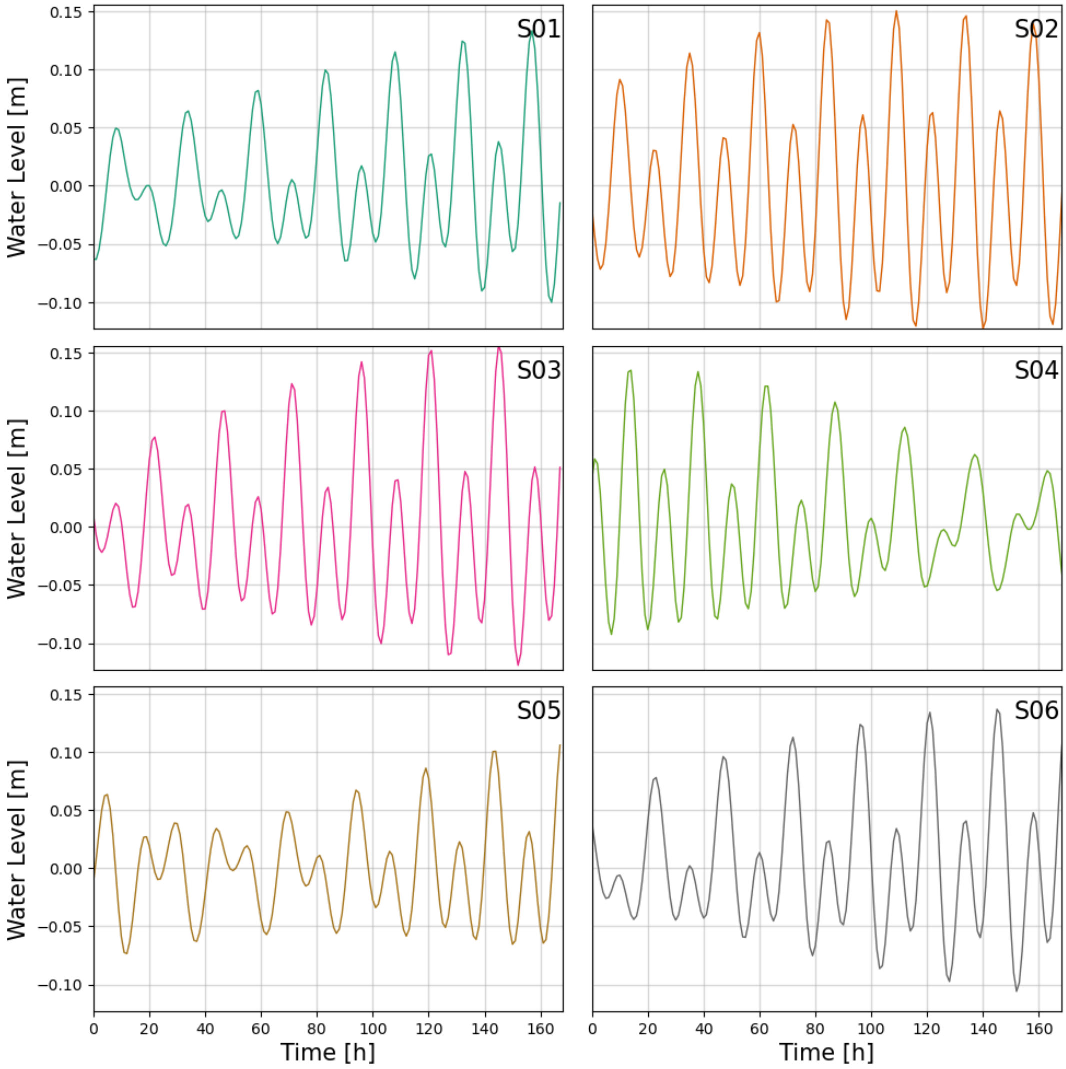

FIGURE 3.1: Tidal forcing signal at the seaside boundary of the model for the selected mete-ocean scenarios.

reference variable. This choice is motivated by the fact that regional currents and tides exhibit relatively low variability over time and are therefore not suitable for defining distinct metocean states, whereas wind is highly variable and would tend to produce an excessive number of clusters unless very short time windows were used. Waves, on the other hand, integrate the wind forcing over space and time and provide a more stable descriptor of sea state. Using waves as the reference allows to adopt a weekly temporal window, which represents a good compromise between the needs of contingency planning and computational cost. The algorithm therefore analyses the hindcast data on a week-by-week basis, identifying peaks in wave height when they fall at the center of each window. If a peak is found, the corresponding week is retained, otherwise, the algorithm moves forward by one day (or any temporal lag defined by the user) and reassesses the next week. This procedure yields a preliminary set of weekly time windows centered around wave height peaks. These weeks are then classified based on four key wave characteristics:

- Wave Energy: the sum of squared wave heights during the week is calculated

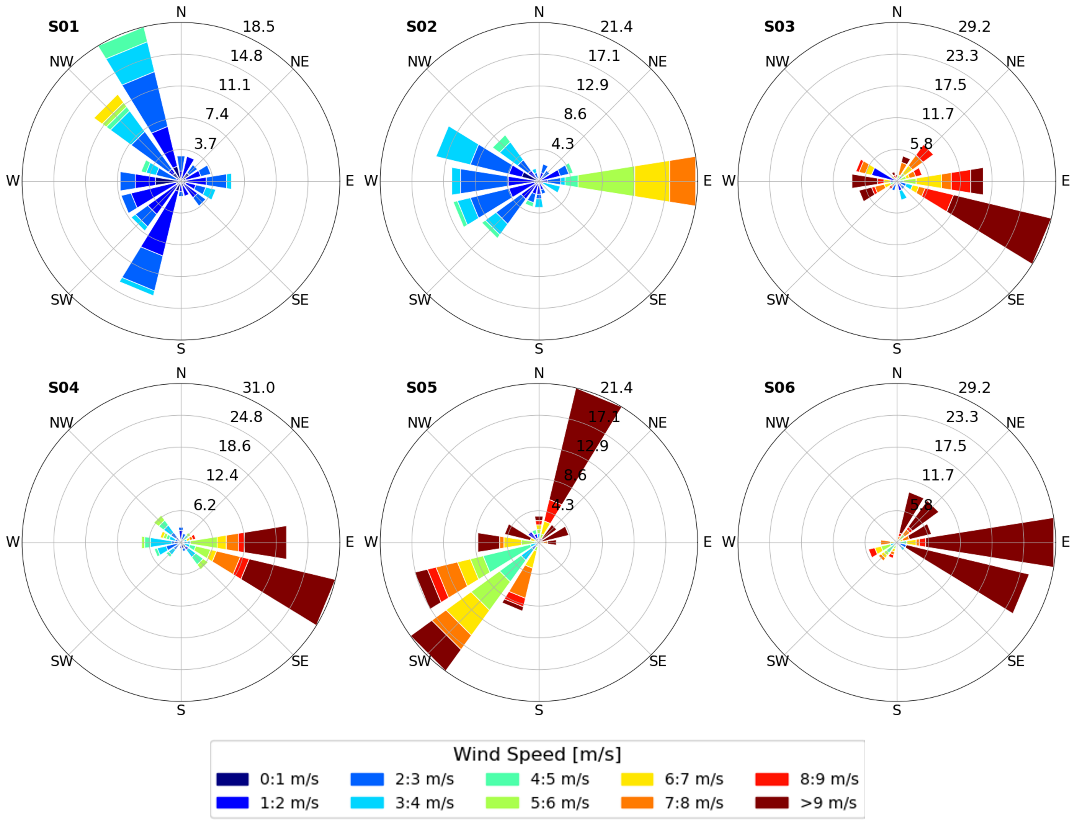

FIGURE 3.2: Rose plot for the wind used as forcing, for the six scenarios analyzed.

and normalized between 0 and 1, allowing classification into three energy levels: low (< 0.3, LE), medium (0.3–0.7, ME), and high (> 0.7, HE).

- Wind-Wave Correlation: if wave heights rise in response to increasing wind velocity, and their mean directions are close, the two signals are considered correlated, reflecting wind-driven waves (WW). A lack of correlation suggests the presence of swell or random waves not directly driven by local winds (RW).
- Directional Spread: the standard deviation of wave direction during the week distinguishing between low-spread events ($< 45^\circ$ spread, LS) and high-spread events ($> 45^\circ$ spread, HS).
- Mean Wave Direction: this parameter categorizes the predominant wave direction into one of eight possible directional bins (North NO, North-East NE, East ES, South-East SE, South SO, South-West SW, West WE, North-West NW), each one covering a 45° angle.

By combining all the above metrics, the maximum theoretical number of combination is 96 ($3 \times 2 \times 2 \times 8$) but, when applied to Genoa domain, the algorithm identifies only 23 scenarios. Finally, from each scenario, the most representative week is selected as the closest, in terms of Euclidean distance, to the mean of all weeks within the cluster. As an example, Figure 3.3 shows the significant wave height time series for each week (thin gray lines) in two clusters: one highly populated (scenario 01, left panel) relative to a common event and one represented by a single week (scenario 20, right panel), corresponding to an extreme event. The number of weeks in

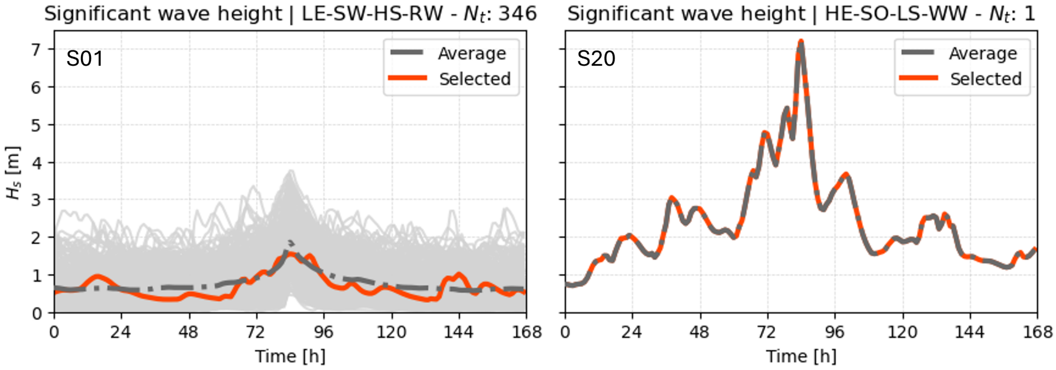

FIGURE 3.3: Significant wave height time series for two cluster, one highly populated (left panel), one represented by a single week (right panel). Thin gray lines represent H_s for each week, bold gray lines shows H_s averaged over all weeks and red lines represent the selected week.

each cluster is reported in the title as N_t. The thick gray line indicates the mean significant wave height over all weeks in the cluster, while the red line highlights the selected representative week.

Because all selected weeks are centered on wave peaks (see the almost bell-shaped signals in Figure 3.3), each scenario fully captures both the onset and decay of storm conditions. Importantly, the method also retains frequent calm sea states, ensuring a balanced representation of both extreme and typical conditions. Each scenario is associated with its probability of occurrence, determined by the number of weeks present in the relative cluster, and detailed in Figure 3.4 in descending order, along with the wave height peak (H_p) annotated within the orange circles. The diameter of the circle is a function of the wave height to reveal how the highest wave events tend to be positioned on the right tail of the histogram.

A resume of all clusters main characteristics is reported in Table 3.1. As an example, wind (top panel) and wave (bottom panel) rose plots corresponding to two scenarios are shown in 3.5, specifically scenario 01 (left column) and scenario 20 (right column). Both scenarios represent uncorrelated wind and wave states, as their directions do not align. Scenario 01, the most frequent in the domain (see 3.1), represents a mild sea state, with sporadic wave heights less than 1.5 m and an average wave height around 0.8 m. In contrast, scenario 20 represents a storm event that occurred in October 2018, with peak wave heights greater than 6 m (see Figure 3.3).

Finally, tide and large-scale currents for each scenario are obtained from the providers described in §1.3. Since Copernicus Marine Service (CMEMS) provides three-dimensional velocity profiles only for a limited time window, the vertical structure of the boundary currents must be reconstructed from the available CMEMS dataset. The dataset used here covers the period from 2024-10-14 to 2025-07-28. Data are extracted along the two rows of grid points closest to the model open boundary (Figure 3.6). These data are averaged in time and along latitude to obtain a single section. The resulting vertical profiles of velocity are shown in the top panel of Figure 3.7. The right panel clearly illustrates the Liguro–Provençal current, with red lines indicating flow entering the domain in its eastern sector and blue lines indicating flow exiting the domain in its western sector.

At the depths corresponding to the sigma layers used in the hydrodynamic model, a vertical shape coefficient α_{d_i} is computed, relating the time-averaged velocity at

scn	**label**	**initial date**	**f [%]**	H_s **[m]**	Dir_p **[°]**	U_w **[m/s]**	Dir_w **[°]**
1	LE-SW-HS-RW	1999-01-14T12:00	43.13	0.78	217.12	5.86	200.34
2	LE-SO-HS-RW	1993-06-20T11:00	17.72	0.65	194.87	4.30	176.43
3	LE-SO-LS-RW	2006-06-15T10:00	9.62	0.66	158.37	4.04	190.97
4	LE-SW-LS-RW	2014-06-26T15:00	8.63	0.75	204.06	4.31	157.10
5	LE-WE-HS-WW	2013-02-20T09:00	5.24	1.09	254.69	7.79	261.32
6	LE-WE-HS-RW	2016-11-30T07:00	4.91	0.90	262.42	6.46	203.92
7	ME-SW-HS-RW	1996-01-30T00:00	2.65	1.73	232.22	10.84	260.12
8	ME-SW-LS-RW	1998-04-03T06:00	1.99	1.58	208.07	7.96	97.41
9	LE-SW-HS-WW	1988-01-11T17:00	1.46	1.11	235.81	7.68	262.83
10	LE-NW-HS-WW	1987-11-26T09:00	1.26	1.09	307.99	8.93	275.96
11	ME-SO-HS-RW	2017-01-14T08:00	0.73	1.76	163.27	11.06	262.23
12	ME-SO-LS-RW	2016-02-06T09:00	0.66	1.90	195.78	8.20	183.58
13	ME-WE-HS-RW	1997-01-01T12:00	0.60	1.66	257.88	8.74	267.04
14	LE-SE-HS-RW	2011-10-16T17:00	0.40	0.86	144.00	6.33	201.06
15	ME-SE-HS-RW	2010-03-06T11:00	0.20	1.46	143.99	8.64	220.72
16	LE-NW-HS-RW	2006-01-05T10:00	0.20	1.00	331.10	8.18	262.73
17	HE-SW-LS-RW	1989-02-23T07:00	0.13	2.65	203.08	9.34	104.37
18	LE-SE-LS-RW	1989-05-07T18:00	0.13	0.61	152.00	4.70	164.83
19	HE-SW-HS-RW	1999-12-24T15:00	0.07	2.26	217.06	9.92	187.70
20	HE-SO-LS-RW	2018-10-26T12:00	0.07	2.36	194.35	10.37	119.33
21	ME-NW-HS-WW	2004-02-20T01:00	0.07	1.56	299.70	9.97	257.42
22	ME-WE-HS-WW	2005-12-08T09:00	0.07	1.71	271.70	11.94	269.12
23	ME-SW-HS-WW	2001-12-10T16:00	0.07	1.44	216.28	9.43	257.81

Table 3.1: List of wind–wave scenarios obtained from the clustering algorithm, sorted in decreasing order of probability of occurrence f. From left to right, columns show: scenario index (scn); scenario label (four two-letter codes indicating, respectively, energy level, directional sector, sea-state class, and wind–wave correlation); initial dates of the scenario; probability of occurrence (f); mean significant wave height (H_s); mean wave direction (Dir_p); mean wind speed (U_w); and mean wind direction (Dir_w).

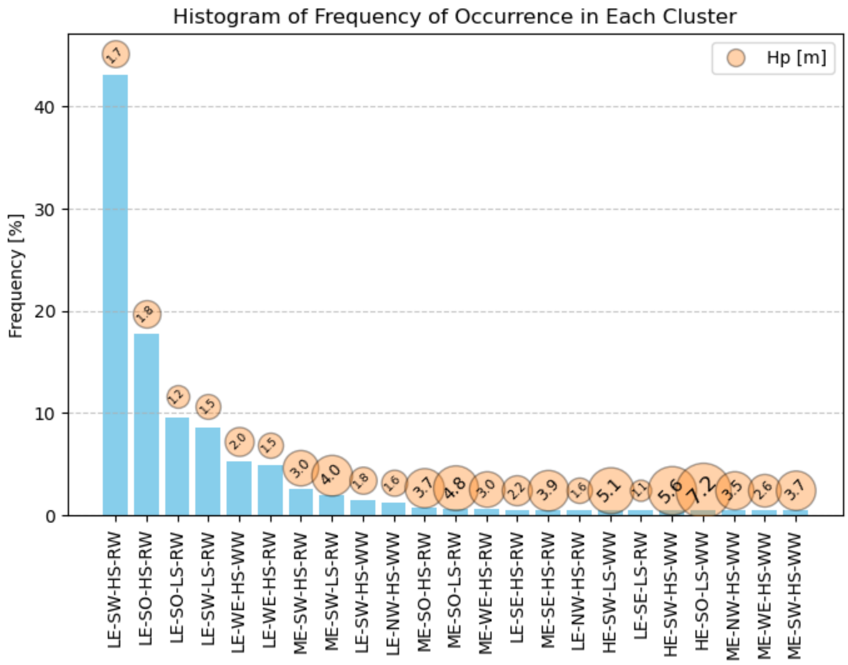

FIGURE 3.4: Histogram of the frequency of occurrence for each cluster. Wave height peak are annotated withing the orange circles, the diameter of which are a function of the wave height peak.

layer i to the corresponding surface velocity:

$$\alpha_{d_i} = \overline{\boldsymbol{u}}(d_i)/\overline{\boldsymbol{u}}_s, \tag{3.1}$$

where $\overline{\boldsymbol{u}}(d_i)$ is the time-averaged horizontal velocity vector at depth d_i, $\overline{\boldsymbol{u}}_s$ is the time-averaged surface velocity vector, and α_{d_i} is a scalar coefficient. The resulting α_{d_i} values, computed separately from the u- and v-components, are plotted in the lower panels of Figure 3.7.

Using these coefficients, the vertical velocity profile for each scenario is reconstructed from the scenario-specific surface velocity as

$$\boldsymbol{u}(d_i, t) = \alpha_{d_i}\,\boldsymbol{u}_s(t), \tag{3.2}$$

which imposes a fixed vertical structure scaled by the time-varying surface currents of each scenario.

To resume, we have now 6 wind and tides scenarios for Narta lagoon and 23 wind, wave, tide and regional currents for the Gulf of Genoa, ready to be used to force two hydrodynamic models.

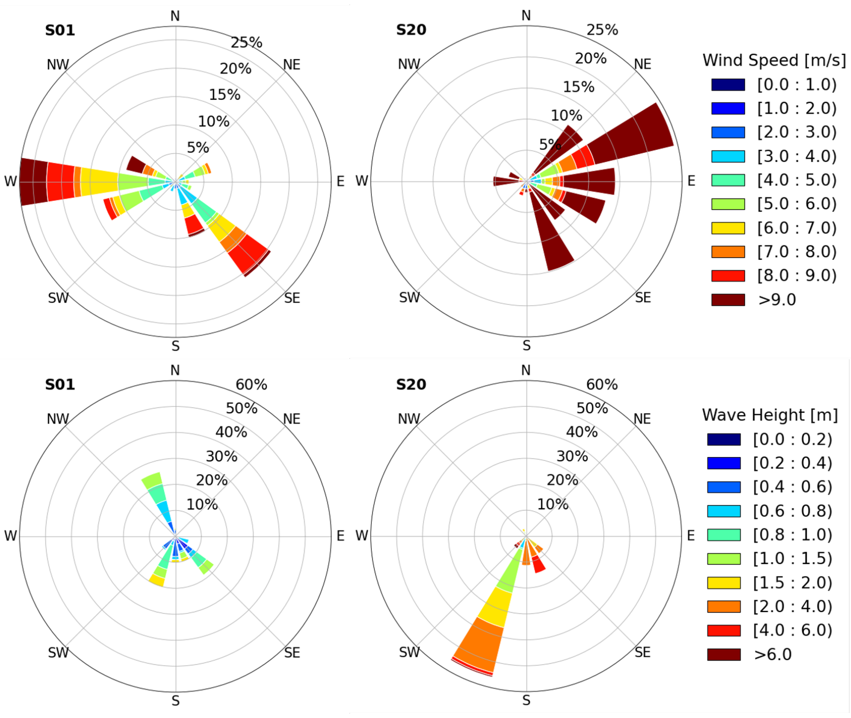

FIGURE 3.5: Rose plots of wind (top panel) and wave (bottom panel) for two scenarios. Both scenarios show uncorrelated wind and waves, with scenario 01 describing a non energetic wave event, while scenario 20 a high energetic wave event.

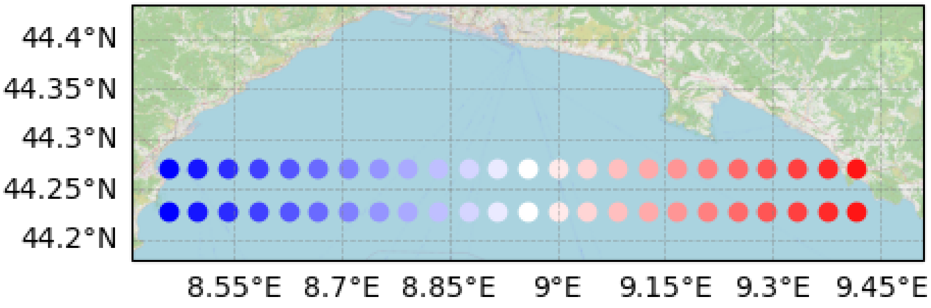

FIGURE 3.6: Position of the grid rows where velocity data are extracted.

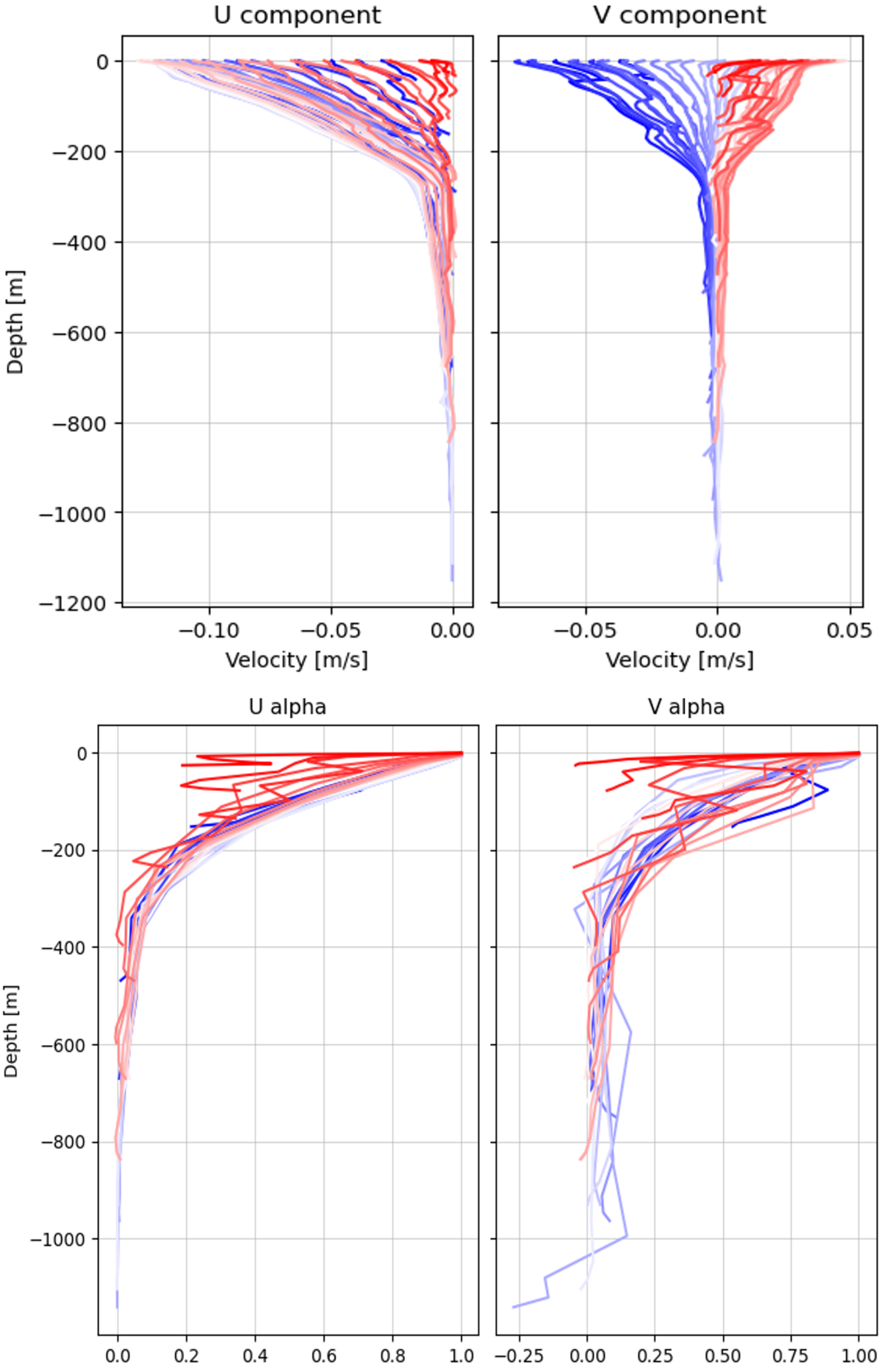

FIGURE 3.7: Vertical profiles of velocity components at different depths, with computed alpha coefficients for each component.

Chapter 4

Hydrodynamic Modeling

A hydrodynamic model integrates environmental variables and topographic features of the study domains to generate velocity fields and other key hydrodynamic properties, such as temperature, salinity, and pressure gradients. Simulations for this study are carried out using Delft3D 4 (Lesser et al., 2004; Delft-Hydraulics, 2007), a widely used numerical model designed to simulate flow, sediment transport and water quality in coastal and estuarine environments. The model solves the hydrostatic, incompressible shallow-water Navier–Stokes equations in a fully three-dimensional (3D) configuration. The horizontal grids employed feature variable spatial resolution, allowing for a refined description of hydrodynamic processes in regions of complex geometry and flow patterns, while the vertical domain is discretized using a sigma-layer approach, which provides an accurate representation of the water-column stratification with higher resolution close to the surface and the bottom.

Under the assumption that the water depth is much smaller than the horizontal length scales, vertical accelerations in the vertical momentum equation are neglected, reducing it to the hydrostatic pressure relation. In this framework, the horizontal velocity components are prognostic variables and are obtained by solving the horizontal momentum equations, whereas the vertical component is diagnosed from the continuity equation. In Delft3D-FLOW these equations are solved in curvilinear horizontal coordinates and sigma (σ) vertical coordinates, as detailed in the Delft3D-FLOW user manual (Delft-Hydraulics, 2007), but they are formally equivalent to the expressions presented here.

In Cartesian coordinates, the three-dimensional, hydrostatic shallow-water momentum equations for the horizontal velocity $\boldsymbol{u} = (u, v)$ can be written as

$$\frac{\partial \boldsymbol{u}}{\partial t} + (\boldsymbol{u} \cdot \nabla)\, \boldsymbol{u} + f\, \boldsymbol{k} \times \boldsymbol{u} = -g\nabla\zeta + \frac{\partial}{\partial z}\left(\nu_t \frac{\partial \boldsymbol{u}}{\partial z}\right) + \boldsymbol{F}, \tag{4.1}$$

where ζ is the free-surface elevation, g the gravitational acceleration, f the Coriolis parameter (computed from the model latitude), $\boldsymbol{k}$ the vertical unit vector, ν_t the vertical eddy viscosity, and $\boldsymbol{F}$ represents external forcing terms.

Under the Boussinesq and incompressible-flow assumptions, mass conservation is expressed by the three-dimensional continuity equation

$$\frac{\partial u}{\partial x} + \frac{\partial v}{\partial y} + \frac{\partial w}{\partial z} = 0, \tag{4.2}$$

where w is the vertical velocity.

To diagnose w from 4.2, kinematic boundary conditions are applied at the free surface and at the seabed. At the seabed $z = -h(x, y)$, impermeability implies

$$w_b = w\big|_{z=-h} \approx 0, \tag{4.3}$$

for mild bottom slopes. At the free surface $z = \zeta(x, y, t)$, the kinematic boundary condition links the vertical velocity to the evolution of the free surface:

$$w_s \equiv w\big|_{z=\zeta} = \frac{\partial \zeta}{\partial t} + u_s \frac{\partial \zeta}{\partial x} + v_s \frac{\partial \zeta}{\partial y}, \tag{4.4}$$

where u_s and v_s are the horizontal velocities evaluated at the free surface. Integrating 4.2 from $z = -h$ to z and using the bottom condition allows w to be diagnosed from the horizontal divergence and the surface motion.

Additional boundary conditions are needed to close the momentum equations. Starting from the bottom stress, the bed shear stress is parameterized using a Chézy-type formulation:

$$\boldsymbol{\tau}_b = \rho_0 \, g \, \frac{\boldsymbol{u}_b \, |\boldsymbol{u}_b|}{C_{2D}^2}, \tag{4.5}$$

where ρ_0 is the reference water density, $\boldsymbol{u}_b$ is the horizontal velocity in the first layer just above the bed, and C_{2D} is the Chézy coefficient, here taken as a constant $C_{2D} = 65 \text{ m}^{1/2}\,\text{s}^{-1}$, which is the default value implemented in Delft3D. The Chézy coefficient depends on water depth and bottom roughness. In the absence of field data on bottom roughness, using the default value provides a reasonable approximation. While the Chézy approach does not account for bedforms, making it less suitable for sediment transport studies, it is still a reasonable method for assessing hydrodynamics in environments with sandy beds.

To represent turbulence, the standard k–ϵ closure scheme is adopted. By solving two additional advection–diffusion equations for the turbulent kinetic energy k and its dissipation rate ϵ, the scheme computes the eddy viscosity ν_t as

$$\nu_t = C_\mu \, \frac{k^2}{\epsilon}, \tag{4.6}$$

where C_μ is an empirical constant, typically taken as $C_\mu = 0.09$ (Launder and Spalding, 1974).

The forcing term $\boldsymbol{F}$ in 4.1 includes all the boundary and surface forces defined in Chapter 3. At the free surface, the wind stress is computed from the 10 m wind speed as

$$|\boldsymbol{\tau}_s| = \rho_a \, C_D \, \boldsymbol{u}_{10}^2, \tag{4.7}$$

where ρ_a is the air density, $\boldsymbol{u}_{10}$ is the wind speed 10 m above sea level, and C_D is the (dimensionless) air–sea drag coefficient. In Delft3D, C_d is specified through a bulk formulation that depends on wind speed and is introduced as a surface stress term in the horizontal momentum equations.

At the open boundaries, tidal forcing is prescribed as time series of water levels. In the Narta domain, a Neumann condition is applied along the lateral boundaries (indicated by yellow arrows in Figure 4.1), imposing a zero normal gradient of sea level. This prevents the development of artificial cross-boundary pressure gradients and effectively avoids spurious inflow or outflow across those boundaries.

Tide and wind are sufficient to reproduce the lagoon dominant hydrodynamics. In contrast, the Gulf of Genoa domain also requires the specification of waves and regional currents at the open boundary. The normal component of the current velocity is applied together with water level via a Riemann-type boundary condition, which is designed to prevent outgoing signals from being spuriously reflected back into

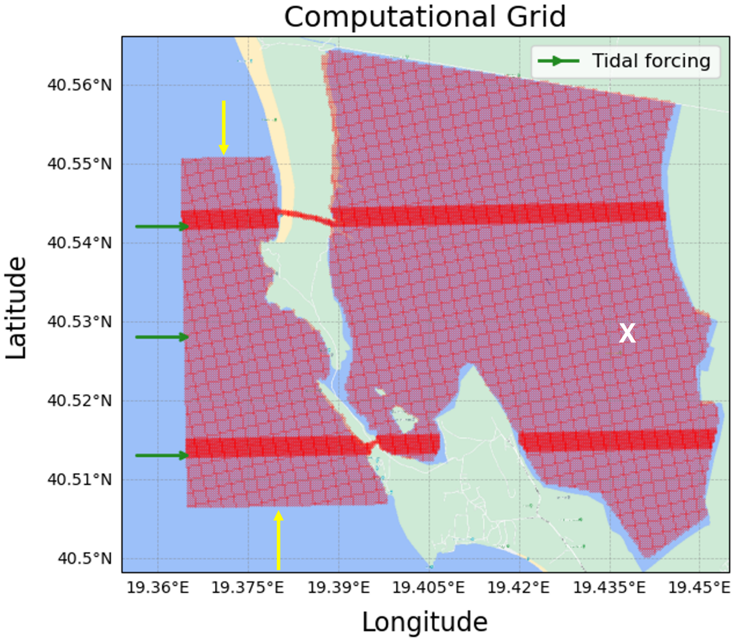

FIGURE 4.1: Narta Lagoon computational grid. Tide signal is placed along the external boundary, as indicated by the green arrows, while the Neumann condition is placed along the horizontal boundaries, indicated by the yellow arrows. The white 'X' marks the hindcast point where the wind forcing is extracted.

the domain. This is achieved by decomposing the flow into two Riemann invariants moving in opposite directions normal to the boundary:

$$R_{\pm} = U_n \pm 2\sqrt{gd} + \zeta\sqrt{\frac{g}{d}}, \tag{4.8}$$

where U_n is the depth-averaged velocity normal to the boundary and d is the still-water depth. In practice, one invariant is determined from the interior solution (outgoing characteristic), while the other is specified from external data (incoming characteristic), thereby allowing outgoing signals to leave the domain with minimal reflection.

Waves are simulated with SWAN (Simulating WAves Nearshore), a third-generation, fully spectral wave model that resolves the full two-dimensional wave energy spectrum as a function of frequency and direction. In its standard form, SWAN solves the spectral action balance equation,

$$\frac{\partial N}{\partial t} + \nabla_{\boldsymbol{x}} \cdot (\boldsymbol{c}_x N) + \frac{\partial}{\partial \sigma}(c_\sigma N) + \frac{\partial}{\partial \theta}(c_\theta N) = \frac{S_{\text{tot}}}{\sigma}, \tag{4.9}$$

where $N(\boldsymbol{x}, \sigma, \theta, t)$ is the wave action density, σ is the intrinsic angular frequency, θ is the wave direction, $\boldsymbol{c}_x$, c_σ and c_θ are the propagation velocities in physical, frequency and directional space, and S_{tot} is the total source term, that includes the effects of generation, dissipation and non linear wave-wave interaction (a detailed definition of each contribution can be found in the relative manual: SWAN User Manual, 2004). In this study, SWAN is dynamically coupled with Delft3D-FLOW, so that both the effect of currents on waves and the effect of waves on currents are taken into account. Time- and space-varying wave conditions are imposed along the open boundary by specifying significant wave height, peak period and mean direction.

A 12-hour spin-up period is included at the beginning of each simulation to allow the flow to adjust to the imposed forcing and to minimize the influence of transient effects associated with the initial conditions. Table 4.1 resumes the main differences between the two hydrodynamic models implemented.

TABLE 4.1: Main differences between the hydrodynamic models of Narta Lagoon and the Gulf of Genoa. Forcings and open boundary conditions: W (wind), T (tide), W_v (wave), C (regional currents).

	Narta Lagoon	Gulf of Genoa
Domain length x [km]	7	80
Domain length y [km]	7	20
Number of σ layers	7	11
Horizontal resolution [m]	30–5	250–50
Integration time step [s]	2.4	3
Forcing and boundary conditions (F/BC)	W, T	W, T, W_v, C
Time-varying F/BC	Yes	Yes
Spatially varying F/BC	No	Yes

4.1 Results: Narta Lagoon

An idealized configuration with open, permanently wet channels is adopted, assuming average inlet depths of approximately 0.2 m for the northern channel and 1 m for the southern channel. Man-made structures and dry conditions induced by sediment transport are therefore neglected. A spatially-varying grid is used, with resolution ranging from 5 m inside the inlets, to 30 m. The hydrodynamic response of the Narta Lagoon is evaluated by analyzing the time-averaged velocity fields at the surface and bottom layers over the duration of each one-week scenario. These simulations represent the combined effects of a uniform in space wind and tidal forcing on the lagoon circulation. The objective is to characterize prevailing flow patterns and assess the system's capacity for water renewal and transport processes under different environmental conditions (Figures 4.2 and 4.3).

Analysis of the surface velocities (left panels) shows that currents generally flow along the lagoon boundaries with higher speed. Consistent with wind intensity, surface velocities are generally low in the first scenarios (e.g. 01 and 02) and increase in the subsequent ones, reaching peak values of around 0.1 m/s in scenario 06.

At the bottom layer (right panels), no clear counter-rotating structures relative to the surface flow are evident. This does not necessarily imply the absence of vertical shear; rather, it is a consequence of the weekly averaging applied to the velocity fields, which tends to smooth out transient features. As a result, the relatively homogeneous patterns in the averaged fields are more representative of the dominant flow direction over the week than of the full instantaneous flow complexity. Overall, the central part of the lagoon is dominated by more uniform currents, while eddy-like structures preferentially develop near the boundaries.

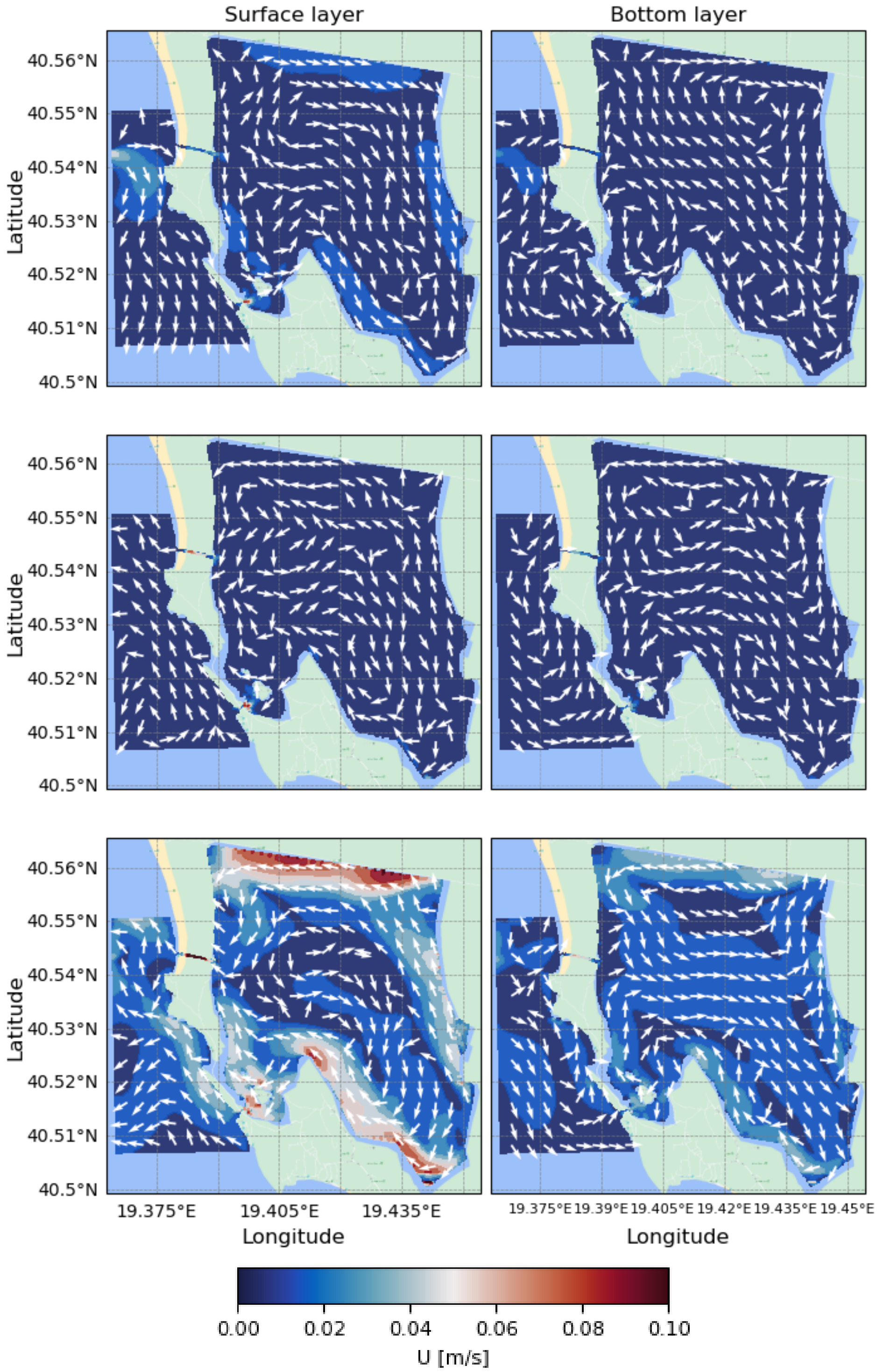

FIGURE 4.2: Weekly-averaged velocity fields in the Narta Lagoon: surface layer (left) and bottom layer (right) for scenarios 01, 02, and 03.

4.1.1 Vortex Energy and Eddy Occupation

The formation of surface eddies, localized rotating structures in the central lagoon, may contribute to water retention and mixing. To quantify these features, the Okubo-Weiss parameter (W) is calculated, following the methodology of Chang and Oey

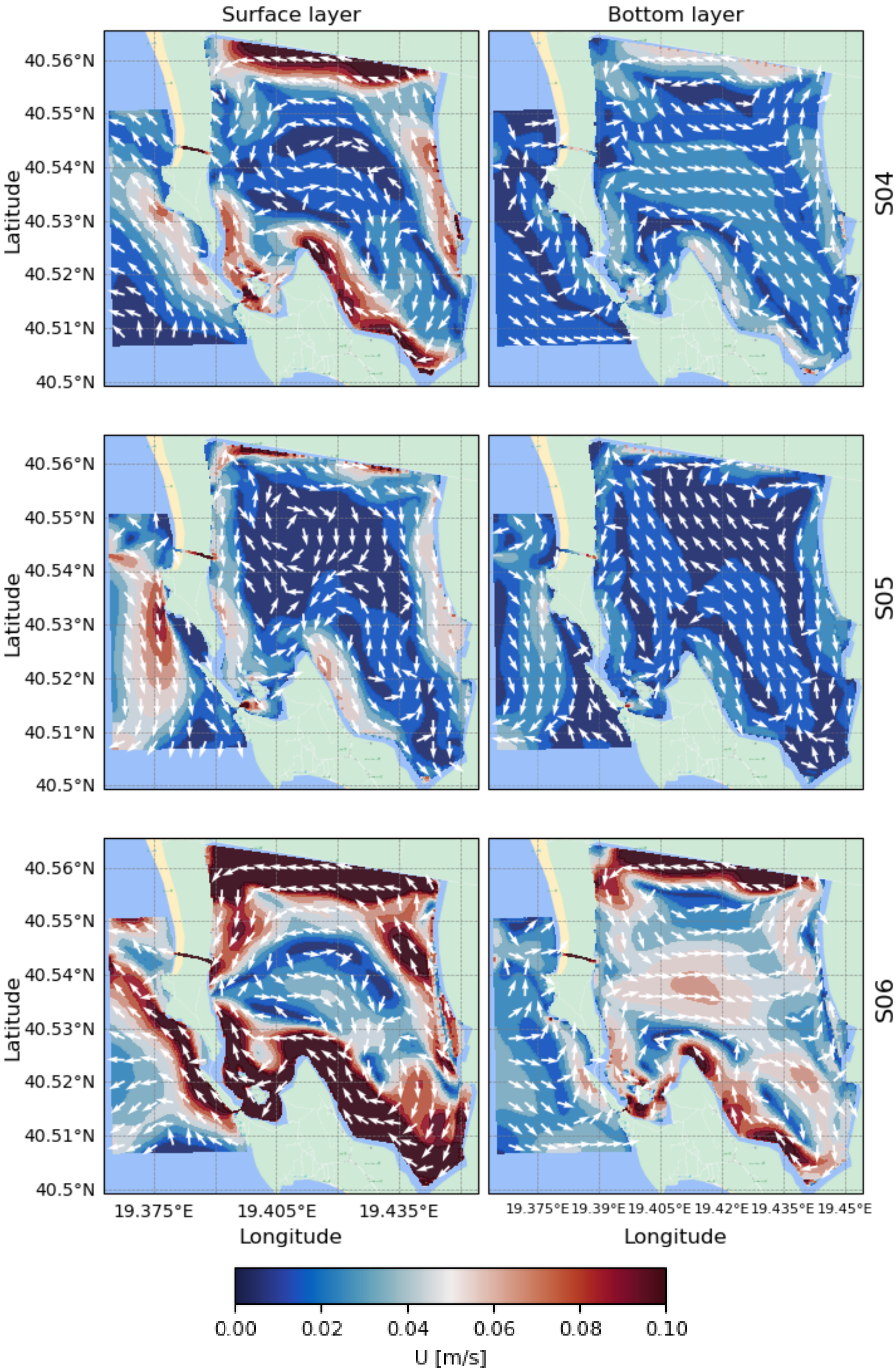

FIGURE 4.3: Weekly-averaged velocity fields in the Narta Lagoon: surface layer (left) and bottom layer (right) for scenarios 04, 05, and 06.

(2014):

$$W = s_n^2 + s_s^2 - w^2, \tag{4.10}$$

where $s_n = \partial u/\partial x - \partial v/\partial y$ and $s_s = \partial v/\partial x + \partial u/\partial y$ are the normal and shear components of strain, and $w = \partial v/\partial x - \partial u/\partial y$ is the vorticity. Regions where $W < 0$

are identified as vortical zones, where vorticity dominates over strain deformation. From this, two eddy characteristics are derived: the vortex energy and eddy occupation.

The vortex energy, defined as:

$$E = \sum_{n=1}^{M} \frac{0.5 \cdot \left(u^2 + v^2\right)}{A_{eddy}}, \tag{4.11}$$

measures the intensity of circulation within the vortical area, where A_{eddy} is the area of the grid cells (M) which satisfies the $W < 0$ condition. The corresponding eddy occupation quantifies the fraction of the lagoon covered by such vortical structures:

$$P_{eddy} = 100 \times A_{eddy} / A_{total}, \tag{4.12}$$

where A_{total} is the full surface area of the computational domain.

As shown in Figure 4.4, vortex energy increases progressively from scenario 01 to scenario 06, consistent with the velocity field results, which display more energetic flow under stronger or more coherent wind conditions in the latter scenarios. In addition, each scenario exhibits substantial temporal variability, with alternating phases of high and low vortex energy. This indicates that the eddies are short-lived, typically forming and dissipating within time scales of approximately 24 hours. This transient behavior highlights the dynamic nature of the lagoon's hydrodynamics and the influence of wind variability on eddy development.

Interestingly, the spatial coverage of eddies (Figure 4.5) shows no clear correlation with the vortex energy. In fact, scenarios with high vortex energy do not necessarily correspond to larger eddy-covered areas, suggesting that stronger eddies may be more compact, while weaker but spatially extensive structures may appear under calmer conditions. This decoupling between eddy energy and spatial occupation underscores the complexity of the flow patterns and further supports the need for localized analysis of lagoon dynamics.

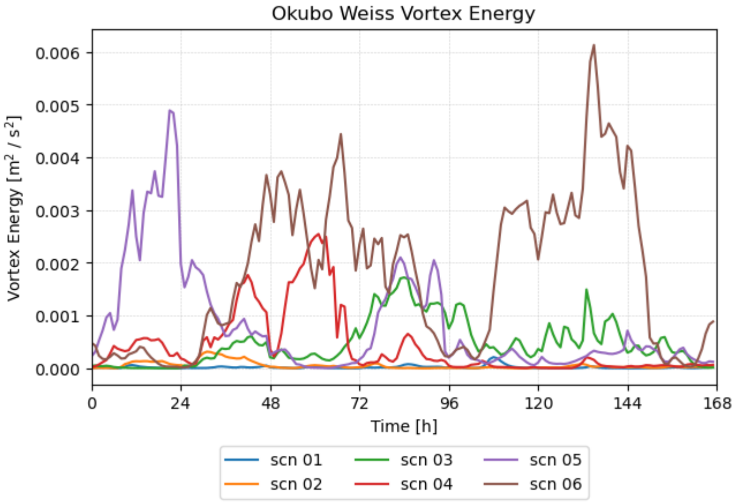

FIGURE 4.4: Time evolution of the Okubo-Weiss vortex energy.

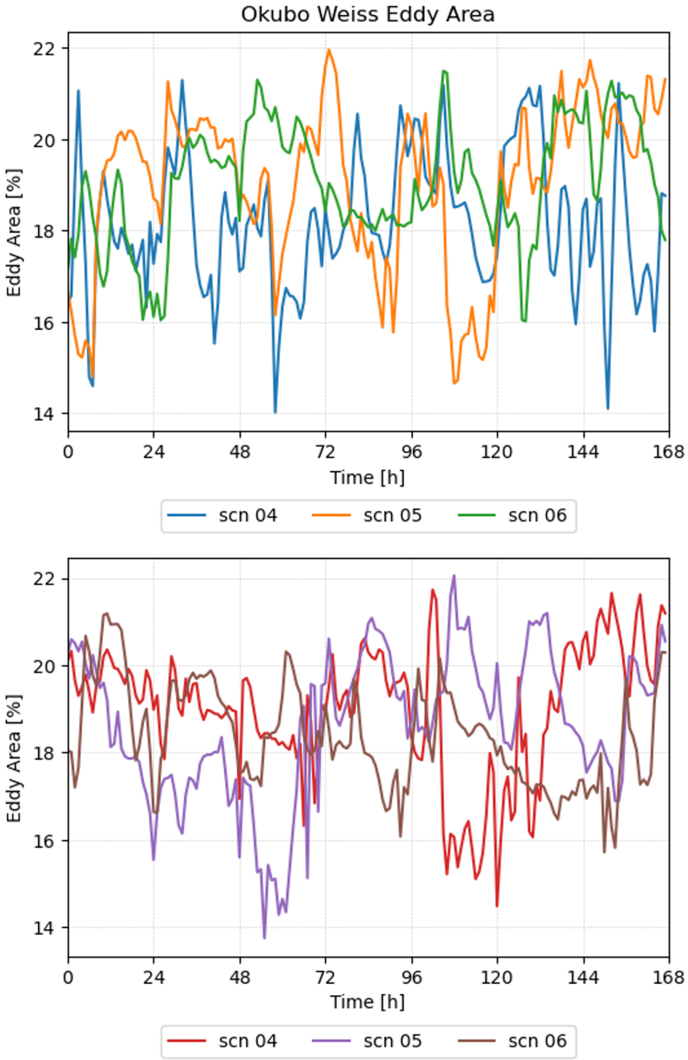

FIGURE 4.5: Okubo-Weiss occupation factor in time for scenario 01, 02, 03 (top panel) and scenario 04, 05, 06 (bottom panel).

4.1.2 Water Exchange Between the Lagoon and the Sea

To evaluate the capacity of the Narta Lagoon to renew its waters and maintain acceptable water quality, two complementary analyses are conducted. The first assesses the influence of tidal forcing on lagoon hydrodynamics by analyzing water level variations, while the second quantifies the water exchange through the inlets, thereby evaluating the degree of connectivity with the Adriatic Sea and the relative importance of wind-driven dynamics.

Water level outputs from the hydrodynamic model are extracted at both ends of the lagoon's inlets, that is, from locations within the lagoon and at their seaward boundaries (Figure 1.1, Panel C). The resulting time series, shown in Figure 4.6, reveal a marked lack of correlation between internal (solid lines) and external (dashed lines) water level fluctuations. Tidal oscillations are barely discernible during scenarios characterized by mild wind conditions, and they completely vanish in the most energetic scenarios (05 and 06). This pattern confirms that tidal signals from the open sea are not effectively transmitted into the lagoon, further supporting the hypothesis of poor hydraulic connectivity through the existing inlets.

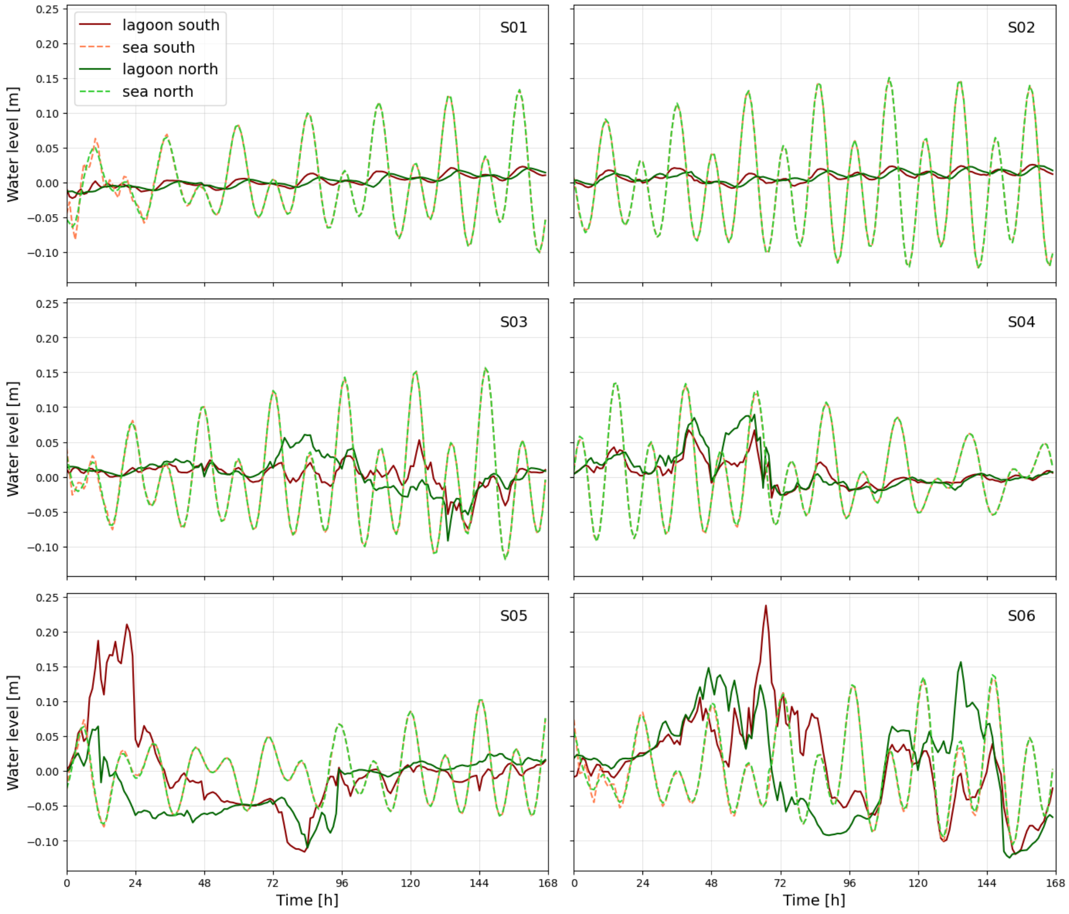

FIGURE 4.6: Simulated water level time series at the sea-lagoon interface for different scenarios. Dashed line: open-sea side; continuous line: inner-lagoon side. Green lines: north channel; red lines: south channel.

TABLE 4.2: Summary of net water exchange for each metocean scenario. Negative values indicate net outflow from the lagoon.

Scenario	01	02	03	04	05	06
Net Exchange (%)	+0.6	+0.4	−0.1	+0.2	+1.0	−3.7

The analysis of water discharge through the inlets (Figure 4.7) provides quantitative confirmation of these findings. The net water exchange across all scenarios remains limited, ranging from -3.7% (net outflow from the lagoon) to +0.6% (net inflow). These values are summarized in Table 4.2. Negative exchange rates are predominantly associated with scenarios featuring easterly winds, which promote lagoon outflow, whereas positive exchange is occasionally observed under opposing wind conditions. Importantly, the tidal signal, detectable in low-energy scenarios, disappears entirely under strong wind forcing, suggesting that wind stress dominates the exchange dynamics in such conditions.

These findings reinforce the conclusions drawn from both field observations and modeling: the hydraulic isolation of the lagoon, even in ideal condition of open inlets, results in limited water renewal and poses a risk to water quality and ecosystem health. Moreover, they highlight the dominant role of wind over tides in driving hydrodynamic processes in this shallow and micro-tidal environment.

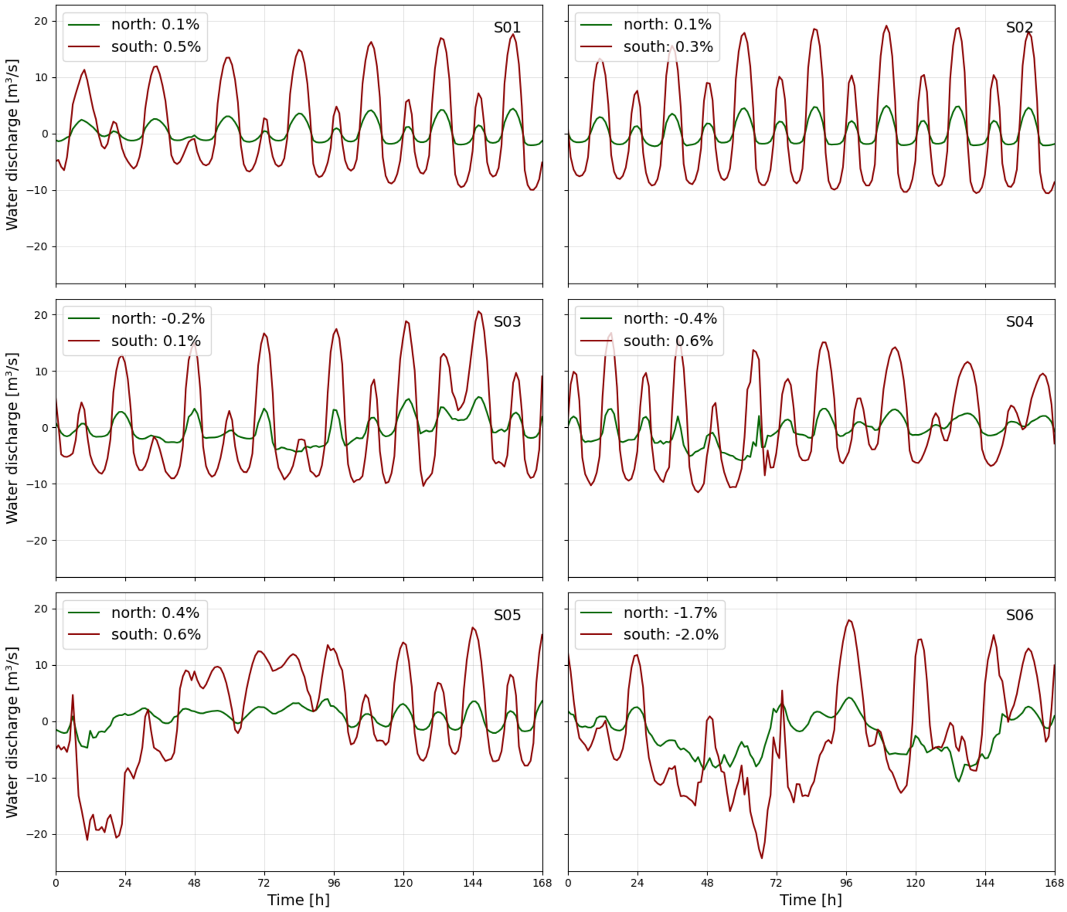

FIGURE 4.7: Net water discharge through the lagoon inlets for each scenario. Green line: north channel; red lines: south channel.

4.2 Results: Gulf of Genoa

The computational mesh used to discretize the Gulf of Genoa (Figure 4.8) has a spatially varying resolution, ranging from approximately 250 m offshore to 50 m inside the port.

In Figure 4.9, the surface velocity fields averaged over one week are shown for two representative scenarios. The top panel, corresponding to scenario 01, illustrates the typical Liguro–Provençal circulation pattern, with a cyclonic (counterclockwise) current entering from the east and exiting to the west. In contrast, the bottom panel, corresponding to scenario 20 and associated with the storm that affected the Ligurian coast in October 2018, shows a net inflow of water into the domain. In this case, intense wind and wave forcing dominate over the background regional current.

To assess the reliability of the model outputs, in-situ water level observations, as described in 1.3, are used for validation. Only the scenarios covered by the water level dataset are considered for validation, resulting in a total of 8 scenarios being used for this analysis. The model's performance is evaluated against these observations through a series of statistical indicators. The Normalized Root Mean Squared Error (NRMSE) and Hanna-Heinold Statistic (HH) both provide a measure of the discrepancies between model predictions and observed values:

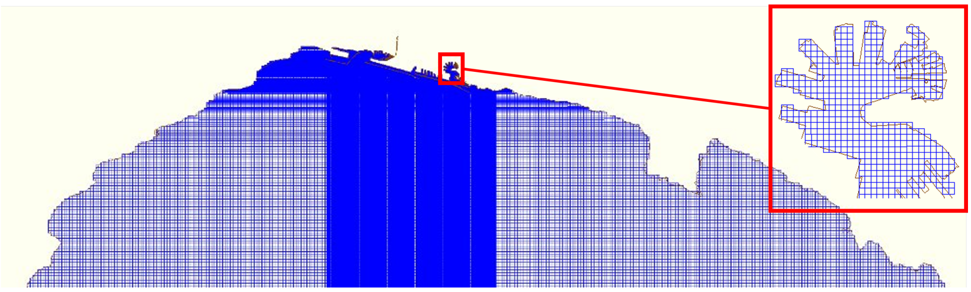

FIGURE 4.8: Computational grid of the Gulf of Genoa, with a zoom inside Porto Antico.

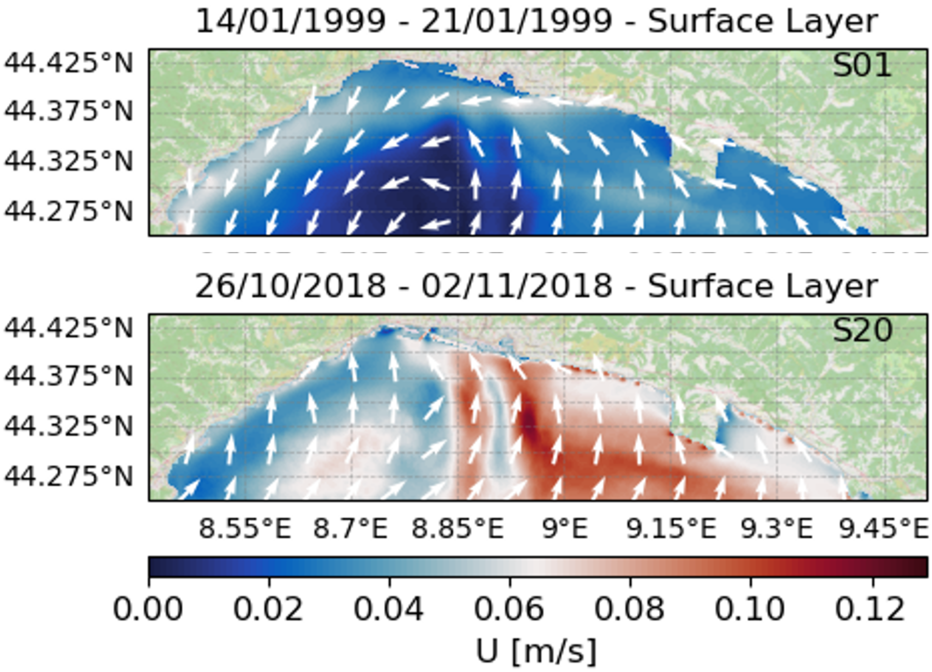

FIGURE 4.9: Surface velocity fields averaged over the week for two scenarios

$$\mathrm{NRMSE} = \sqrt{\frac{\sum_{i=1}^{n}(w_i - \eta_i)^2}{\sum_{i=1}^{n}\eta_i^2}}, \tag{4.13}$$

$$\mathrm{HH} = \sqrt{\frac{\sum_{i=1}^{n}(w_i - \eta_i)^2}{\sum_{i=1}^{n}\eta_i w_i}}, \tag{4.14}$$

where w_i represent the predicted values, η_i the observed values and n the number of data points. Both of these metrics provide insight into the error between the model and the observations, but they differ in their normalization approach. The NRMSE normalizes the error by the variance of the observed values, making it particularly useful for assessing the magnitude of error relative to the overall data variability. On the other hand, the HH statistic normalizes by the product of the observed and predicted values, making it more sensitive to the relationship between these values, especially when their magnitudes differ. The results (first two boxes in Figure 1.6, left panel) indicate that the median NRMSE and HH values are less than 0.4 and 0.5, respectively, suggesting that the model provides relatively accurate predictions.

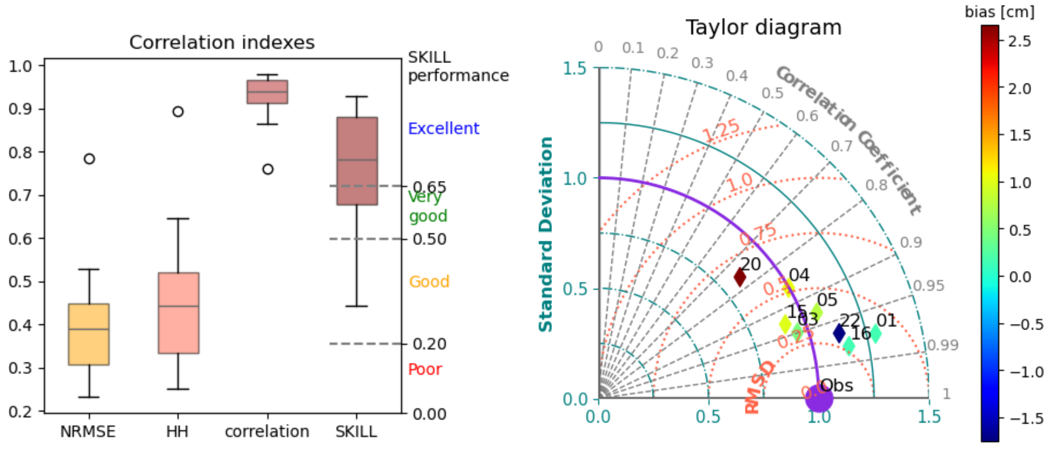

FIGURE 4.10: Model validation against observed water levels inside the Port of Genoa. Top panel: boxplots of the statistical indicators computed for all scenarios. Bottom panel: Taylor diagram summarizing, for each scenario, the correlation, normalized standard deviation and centered RMSE.

The correlation between model predictions and observations is further assessed using Pearson's Correlation Coefficient (ρ) and the Skill Score:

$$\rho = \frac{\sum_{i=1}^{n}(w_i - \bar{w})(\eta_i - \bar{\eta})}{\sigma_w \sigma_\eta} \cdot \frac{1}{n}, \tag{4.15}$$

$$\text{Skill} = 1 - \frac{\sum_{i=1}^{n}(w_i - \eta_i)^2}{\sum_{i=1}^{n}(w_i - \bar{w})^2}, \tag{4.16}$$

where the overbar denotes the average values, σ_w represents the standard deviation of the predicted values and σ_η represents the standard deviation of the observed values. The Pearson's correlation coefficient, ρ, provides a measure of how well the model captures the overall trend and variability in the data. Meanwhile, the Skill Score evaluates the model's performance in comparison to simply predicting the mean of the observed values, with a score of 1 representing perfect skill and a score of 0 indicating no improvement over the baseline. For this study, the median values of ρ and Skill are close to 1 and 0.8 respectively (third and fourth boxes in Figure 4.10, left panel) which indicates a high degree of agreement between the model predictions and the observed data. In line with previous literature, the Skill Score is interpreted as follows: $Skill > 0.65$ excellent; > 0.50 very good; > 0.2 good, and < 0.2 poor (Allen, Somerfield, and Gilbert, 2007; Warner, Geyer, and Lerczak, 2005; Maréchal, 2004; Willmott, 1981).

A prompt assessment of the goodness of fit is provided by the Taylor diagram (Figure 4.10, right panel). In this diagram, the violet circle represents the observed data, while model results are displayed as diamonds, colored according to the bias. The closer these diamonds are to the violet circle, the better the model's performance, indicating a smaller error and higher correlation with the observed data. The black numbers near the diamonds represent the corresponding scenario for each model result.

The Taylor diagram provides a comprehensive visual summary of multiple statistical metrics, such as correlation, standard deviation, and RMSE, allowing for a quick comparison of model performance across different scenarios. The arrangement of the diamonds relative to the violet circle reveals both the consistency of the model's performance across scenarios and how well it captures the observed variability and mean water levels.

Overall, the results demonstrate that the model effectively reproduces the observed water levels, with a good agreement across the majority of scenarios. Keeping in mind the geometric complexity of the Gulf of Genoa, the heterogeneous bathymetry, and the combined influence of several forcings, the model shows strong skill in capturing the key features of the water levels, with smaller discrepancies observed in scenarios with more extreme conditions or greater complexity (e.g. scenario 20).

Chapter 5

Lagrangian Modeling

With the velocity fields available, it is possible to study the dispersion of particles in the sea using Particle Tracking Models (PTMs). This study focuses on floating particles; hence, only the surface velocity layer is used from this point onward. By integrating the 2D velocity at the particle positions in time, Lagrangian models solve the advection of passive tracers, which simply follow the flow. To account for sub-grid dynamics that are not resolved by the hydrodynamic model, a diffusive component is added to the particle motion:

$$\boldsymbol{x}(t+\Delta t) = \boldsymbol{x}(t) + \int_{t}^{t+\Delta t} \boldsymbol{u}\big(\boldsymbol{x},t\big)\,dt + \boldsymbol{R}\,\sqrt{2K\Delta t}, \tag{5.1}$$

where $\boldsymbol{x}$ is the particle position, $\boldsymbol{u}(\boldsymbol{x},t)$ is the velocity at that position (obtained by linear interpolation of the surrounding grid velocities), K is the horizontal diffusion coefficient, $\boldsymbol{R}$ is a random number drawn from a Gaussian distribution with zero mean and unit variance, $\mathcal{N}(0,1)$, and Δt is the integration time step. Time integration is performed using a fourth-order Runge–Kutta scheme. Depending on the simulation, the advecting velocity can be given by the current velocity alone, or by a linear combination of currents and wind at 10 m above the sea surface:

$$\boldsymbol{u}(\boldsymbol{x},t) = \boldsymbol{u}_c(\boldsymbol{x},t) + C_d\,\boldsymbol{u}_w(\boldsymbol{x},t), \tag{5.2}$$

where $\boldsymbol{u}_c$ is the current velocity, $\boldsymbol{u}_w$ is the 10 m wind velocity and C_d is the windage coefficient. Including windage in the advection equation is fundamental when modeling the transport of floating substances, as it accounts for the direct physical forcing exerted by the wind on the surface area of the object exposed to the atmosphere.

Following the Smagorinsky approach, the diffusion coefficient K is parameterized in terms of the local shear of the flow:

$$K = C_s\,\Delta x\,\Delta y\,\sqrt{\left(\frac{\partial u}{\partial x}\right)^2 + \left(\frac{\partial v}{\partial y}\right)^2 + \frac{1}{2}\left(\frac{\partial u}{\partial y} + \frac{\partial v}{\partial x}\right)^2}, \tag{5.3}$$

where $\Delta x \Delta y$ is the grid-cell area and C_s is the Smagorinsky coefficient, chosen to ensure realistic spreading without excessive artificial diffusion.

For the Narta case study, only passive tracer dispersion is considered. For Genoa, the analysis begins with passive tracers and is then extended to oil and hazardous and noxious substances (HNS). To predict the dispersal behavior of these specific substances, the Lagrangian model is coupled with a weathering module, which represents the main physicochemical processes governing the fate of oil and HNS once they enter the marine environment. These processes depend on both substance properties and environmental conditions and are described by well-established formulations. Some of them act on time scales longer than one week, while others take place immediately after the spill. Given the weekly scenarios analyzed here, the most relevant processes are evaporation (for oil and some HNS) and dissolution (for HNS).

Evaporation is calculated using the analytical model proposed by Stiver and Mackay (1984):

$$\Delta F = \exp\left[6.3 - \frac{10.3}{T_0}\left(T_0 + T_G F\right)\right]\left(\frac{k_e A \Delta t}{V_0}\right), \tag{5.4}$$

where F is the evaporated fraction, k_e is the mass-transfer coefficient, A is the oil slick surface area, V_0 is the spilled oil volume, T is the environmental temperature, and T_0 and T_G are distillation-related constants.

For dissolution, the rate of change of the number of dissolved moles $n_{i,d}$ of the i-th component is given by Mackay and Leinonen (1977):

$$\frac{dn_{i,d}}{dt} = K_d\left(x_{mi}C_i^s - C_i^w\right)A, \tag{5.5}$$

where A is the slick–water interface area, K_d is the dissolution mass-transfer coefficient, x_{mi} is the mole fraction of the i-th component in the oil phase, C_i^s is its pure-component solubility, and C_i^w is its actual concentration in the water phase.

Along solid boundaries, one of the following slip conditions is applied:

- **No-slip condition**: particles entering land cells are considered beached and are removed from the simulation.
- **Slip condition**: a displacement correction of 0.01 $\mathrm{m\,s^{-1}}$ is applied, shifting any particle intersecting a solid boundary towards the nearest ocean cell along the local normal direction, effectively preventing beaching. A visual representation of the slip condition inside the Port of Genoa is shown in Figure 5.1. The length of the arrows in the figure is not proportional to the actual displacement magnitude, but is chosen to enhance visibility.

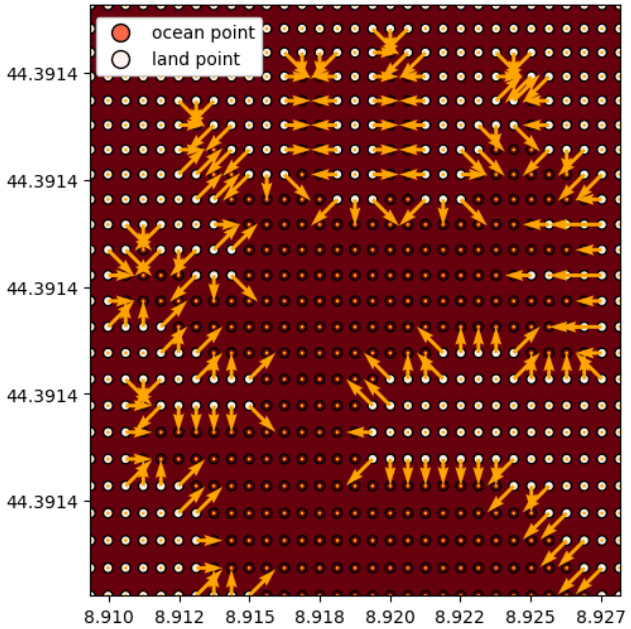

FIGURE 5.1: Visual representation of the slip condition moving particles toward the internal waters.

5.0.1 Windage Calibration with Drifters

For oil and HNS simulations, wind forcing is included in the particle dynamics (see Equation 5.2). Ideally, the associated windage coefficient C_d would be calibrated directly against oil or HNS observations. However, in the absence of such data for the Port of Genoa, C_d is here estimated using surface drifter trajectories. This calibration is directly applicable to neutral, surface-following virtual particles and therefore provides a robust basis for future passive-tracer simulations. In the present work, it is also used as a first-order approximation for the wind contribution to the transport of oil and HNS, acknowledging that these substances do not behave identically to drifters.

In total, N_d drifters (the number of which changes from day to day because some drifters loose their GPS signal during each campaign) are released on six different days, between 2022-11-18 and 2025-03-20, covering different seasons but, for logistics and safety, only under calm sea conditions. Releases takes place in the Porto Antico area of the Port of Genoa (Figure 5.3). During each field day, drifters are deployed in the morning and tracked for a few hours until they ground against docks or breakwaters and are recovered. Of all releases, only 23 drifters are usable for calibration; units are excluded when trajectories are too short (less than 1 hour) or the GPS failed.

As shown in Figure 5.4, these 23 usable drifters are split into a training set (16 drifters, 70%) and a testing set (7 drifters, 30%). For each training drifter, a series of virtual-particle simulations is performed with different trial values of C_d, and a skill score is computed for each run. This produces, for each drifter, an ensemble of candidate trajectories with associated skill scores. The best-performing runs are then combined to obtain a single calibrated value of C_d, which is subsequently used to simulate the independent test drifters and evaluate the robustness of the calibration.

Hydrodynamics for the field days are simulated with the same model described in Chapter 4, using forcings and boundary conditions corresponding to the specific dates of the drifter experiments. The Lagrangian model releases virtual particles at the observed drifter start positions and moves them using only advection–diffusion (no weathering). The horizontal diffusivity is set to $0.2\,\mathrm{m^2\,s^{-1}}$, consistent with values commonly adopted in operational oil-spill tools for port applications (Liubartseva et al., 2021), and the model output interval is set to 5 minutes to match the drifter sampling frequency. Simulations end when the virtual drifter enters a land cell, or at the last recorded time of the corresponding real drifter.

The optimal trajectories for the 23 training drifters are determined via Bayesian optimisation (using the Optuna Python package) over $C_d \in [0.01, 0.04]$. Trials with fewer than 12 valid time steps (i.e. shorter than 1 hour) are discarded, and for each drifter 20 valid trials are retained.

Model–data comparison uses the Normalized Cumulative Lagrangian Separation (NCLS) and a corresponding skill score SS (Liu and Weisberg, 2011). For a single trajectory with N_t time steps, NCLS is defined as

$$\mathrm{NCLS} = \frac{\sum_{k=1}^{N_t} d_k}{\sum_{k=1}^{N_t} l_k}, \tag{5.6}$$

where d_k is the separation between simulated and observed locations at time step k, and l_k is the observed path increment between time steps $k-1$ and k (see Figure 5.2 for a visual representation of NCLS).

The associated skill score is

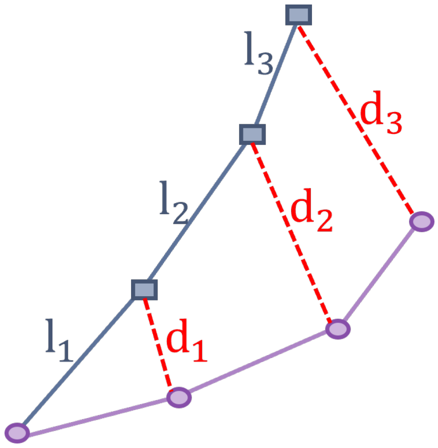

FIGURE 5.2: Normalized Cumulative Lagrangian Separation scheme. The gray line represents the observed path, while the violet line represents the simulated path.

$$SS = \begin{cases} 1 - \dfrac{\mathrm{NCLS}}{n}, & \text{if NCLS} \leq n, \\ 0, & \text{if NCLS} > n, \end{cases} \tag{5.7}$$

where $n = 3$ is a non-dimensional tolerance threshold for the non-skill criterion. This metric penalises growing trajectory discrepancies while capping the score at zero when the separation becomes too large. In Figure 5.3, colored virtual tracks show the best-scoring simulations for each case taken as example; observed tracks are in red, release points in yellow and virtual positions are colored in function of the SS.

For drifter m, each trial j has an associated skill score $SS_{m,j}$ and number of time steps $N_{m,j}$. To give more weight to higher scores and longer comparisons, a weight is defined for each trial

$$\Upsilon_{m,j} = N_{m,j}\, SS_{m,j}^{p}, \tag{5.8}$$

where $SS_{m,j}$ is the skill score for drifter m and trial j, $N_{m,j}$ the relative number of time steps and $p = 2$ controls how strongly high-score runs are emphasised.

For each drifter, a single "best" trial is then selected as the one maximising $\Upsilon_{m,j}$, yielding an optimal coefficient $C^*_{d,m}$ and its associated (N^*_m, SS^*_m).

In a second step, the final calibrated windage coefficient is obtained as a weighted average of these per-drifter optimal values:

$$C_d = \frac{\sum_{m=1}^{N_{\text{train}}} \Upsilon_m\, C^*_{d,m}}{\sum_{m=1}^{N_{\text{train}}} \Upsilon_m}, \qquad \Upsilon_m = N^*_m\, (SS^*_m)^p\,, \tag{5.9}$$

where N_{train} is the number of drifters in the training set. This two-step weighting scheme ensures that (i) for each drifter, the most reliable trajectory is chosen, and (ii) drifters with longer and better-matched trajectories exert a stronger influence on the final calibrated value. The analysis yields a calibrated windage coefficient $C_d = 0.02$.

The blue curve in Figure 5.4 shows the best training SS values associated with the optimisation, while the orange dashed curve shows the corresponding C_d trials. Test results (green markers in Figure 5.4) are obtained by rerunning the model with

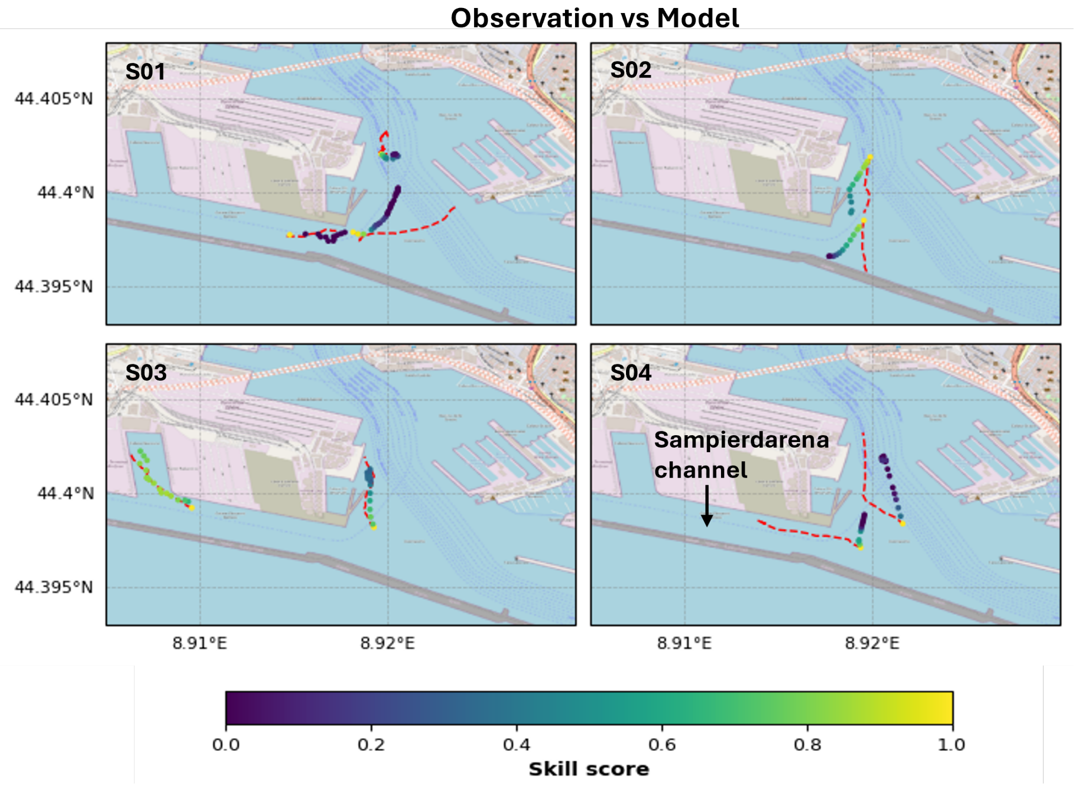

FIGURE 5.3: Observed (red dashed) and simulated (colored markers) drifter trajectories for six scenarios. Simulated points are colored by the NCLS-based skill score SS.

$C_d = 0.02$. Training scores span 0.0–0.8, whereas test scores range from 0.2 to 0.58, indicating a reasonable but not perfect level of generalisation.

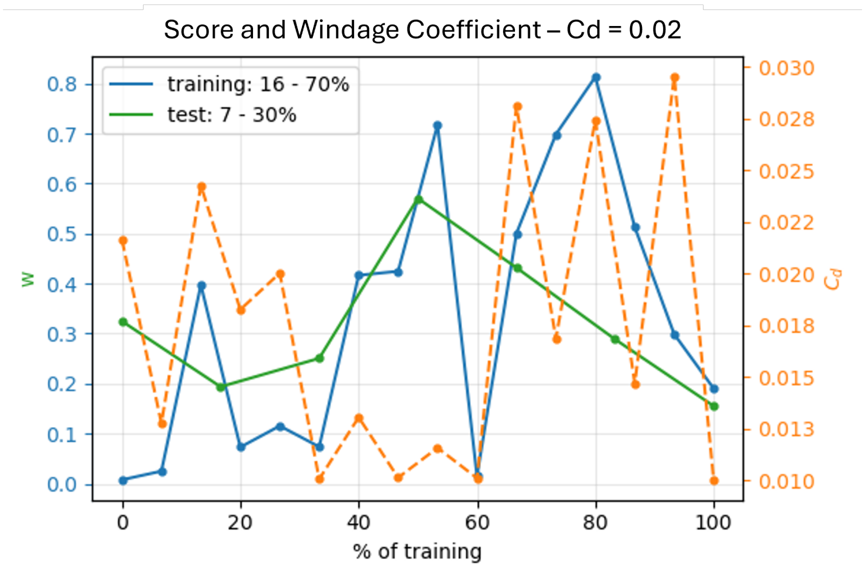

FIGURE 5.4: Training scores (blue) and trial C_d values (orange dashed). Test scores (green) are computed with the single calibrated $C_d = 0.02$.

5.1 Passive Tracer Simulations

Surface Lagrangian simulations of passive tracers are performed with Parcels (Probably A Really Computationally Efficient Lagrangian Simulator, Delandmeter and Van Sebille, 2019), using the surface layer of the hourly three-dimensional velocity fields from the hydrodynamic models.

For each scenario, virtual particles are released evenly throughout the lagoon and the port domains, with an initial spacing of roughly 30 m.

For Narta Lagoon, a second configuration is considered in which particles are released in a plume-shaped area, located at the sewage wastewater discharge of the nearby village of Narta. Two release strategies are tested: (i) an instantaneous release at the initial simulation time, and (ii) a continuous release every 6 hours during the first four days, to mimic a persistent discharge. In the latter case, particles are removed from the simulation after 72 hours to avoid an unrealistic accumulation of particles. To ensure particles stay in the simulation for the same temporal windows, no release occurs in the last three days of the simulation. Table 5.1 resume the main differences between the Lagrangian models implemented.

TABLE 5.1: Main differences between the Lagrangian models of Narta Lagoon and the Port of Genoa.

	Narta Lagoon	Narta Plume	Port of Genoa
Number of particles	26000	6000-72000	22000
Particles spacing [m]]	30	10	30
Integration time step [s]	30	30	60
Output temporal resolution [m]	60	60	5/60
Smagorinsky coefficient	0.1	0.1	0.001
Slip condition	no	yes	yes vs no

5.1.1 Narta Lagoon

Starting from the uniformly distribution configuration, trajectories of particles leaving the lagoon for each scenario are shown in Figure 5.5, along with the exit rates which range from 0.2% to 1.5% and the percentage of particles beached, from 16% to 88% (see also Tab. 5.2).

Scenario		01	02	03	04	05	06
Particles %	TOT	0.3	1.0	1.1	1.5	0.3	0.2
	N	58	86	87	100	73	100
	S	42	14	13	0	27	0

TABLE 5.2: Percentage of particle's exchange between the sea and the lagoon (TOT) and proportion of particles leaving through the two channels (N and S) for the different metocean scenarios.

A no-slip condition is applied along the boundaries, so that when a particle enters a land cell it becomes trapped and cannot re-enter the lagoon. Interestingly, most particles exit the lagoon through the northern channel, despite its being longer

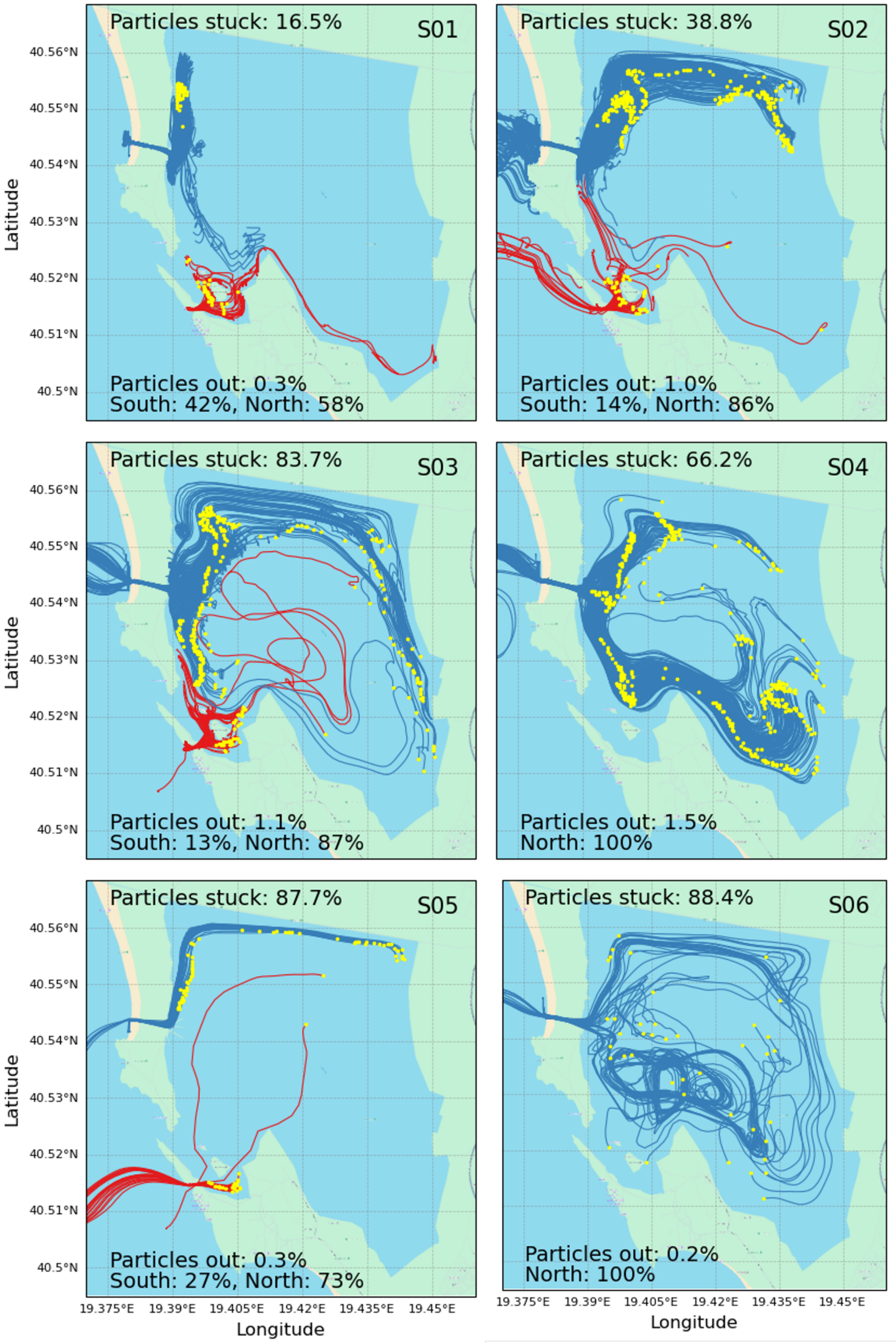

FIGURE 5.5: Trajectories of particles leaving the lagoon through North (blue) and South channels (red). Yellow dots indicate releasing positions.

and narrower than the southern one. This counterintuitive result is primarily attributed to the presence of islands sheltering the southern channel, which act as physical barriers, redirecting and obstructing particles pathways. For those scenarios where particles do exit through the southern inlet (e.g., scenarios 01, 02, 03, and 05), their origins (releasing positions are represented by yellow dots) are predominantly confined to the area between the islands and the coastal barrier separating the lagoon from the open sea. Only in scenario 03 does a small number of particles originate from the eastern side of the islands. This indicates that the islands significantly limit connectivity with the southern channel, reducing the effective exchange through that outlet.

Additionally, in several scenarios (e.g., 02, 03, 04, and 05), the particles that eventually left the lagoon tended to be released near the boundaries, rather than from the central basin. This pattern appears to result from a "conveyor belt" effect, where higher current velocities and peripheral circulation patterns, often in the form of clockwise or counterclockwise eddies (already mentioned in §4.1), transport particles along the margins of the lagoon toward the inlets.

In lower-energy scenarios (e.g., 01, 02), particles that successfully exit the lagoon typically originate close to the inlets, due to reduced overall circulation and weaker mixing. Conversely, in more energetic scenarios (e.g., 06), particles may exit from more interior locations, indicating enhanced dispersion and connectivity due to stronger circulation.

Finally, the proportion of stuck particles tends to increase with scenario energy: in scenario 06, despite high average velocities and easterly wind forcing (favorable for outflow), the exit rate drops to just 0.2%, while the percentage of stuck particles is about 88%. These results emphasize the nonlinear relationship between wind forcing and flushing efficiency, and highlight how local morphology and small-scale circulation features critically shape the lagoon's dispersive behavior.

The second configuration focuses on simulating sewage wastewater discharge into the lagoon. A slip condition is applied so that the resulting trajectories can later be used for the mixing properties analysis, and the lagoon is treated as a closed basin, with the northern channel hypothetically blocked by sediment infilling and the southern one closed by the sluice gates described in Chapter 2.

As shown by the hydrodynamic simulations, even under idealised open-channel conditions the external water level has a negligible influence on the lagoon's internal circulation, except in the immediate vicinity of the inlets. This suggests that closing the inlets would only marginally affect the bulk circulation inside the lagoon. For this reason, no additional hydrodynamic simulation is performed for the closed-lagoon case; instead, the existing velocity fields are used, neglecting the outer cells.

In the first set of simulations, particles are released only at the initial time step. Figure 5.6 shows the resulting trajectories for all scenarios. The grey cloud in the bottom-right corner of the lagoon indicates the release area, while the red dots mark the final particle positions. Intermediate positions are coloured according to simulation time, illustrating the progressive dispersion of the plume. Marked differences emerge across scenarios. In scenario 01, particles remain clustered near the release area, whereas in scenarios 03 and 06 enhanced mixing disperses them throughout much of the lagoon. In scenarios 02, 04 and 05, particles are mainly trapped by boundary-following currents and only under specific conditions, particularly toward the end of the simulations, do they move away from the shoreline.

To investigate the sensitivity of plume dispersion to the release timing, a second set of simulations is performed with a continuous release. In this case, particles are released within the plume area every 6 hours during the first 96 hours of the simulation. To prevent excessive accumulation, each particle is removed 72 hours after its release.

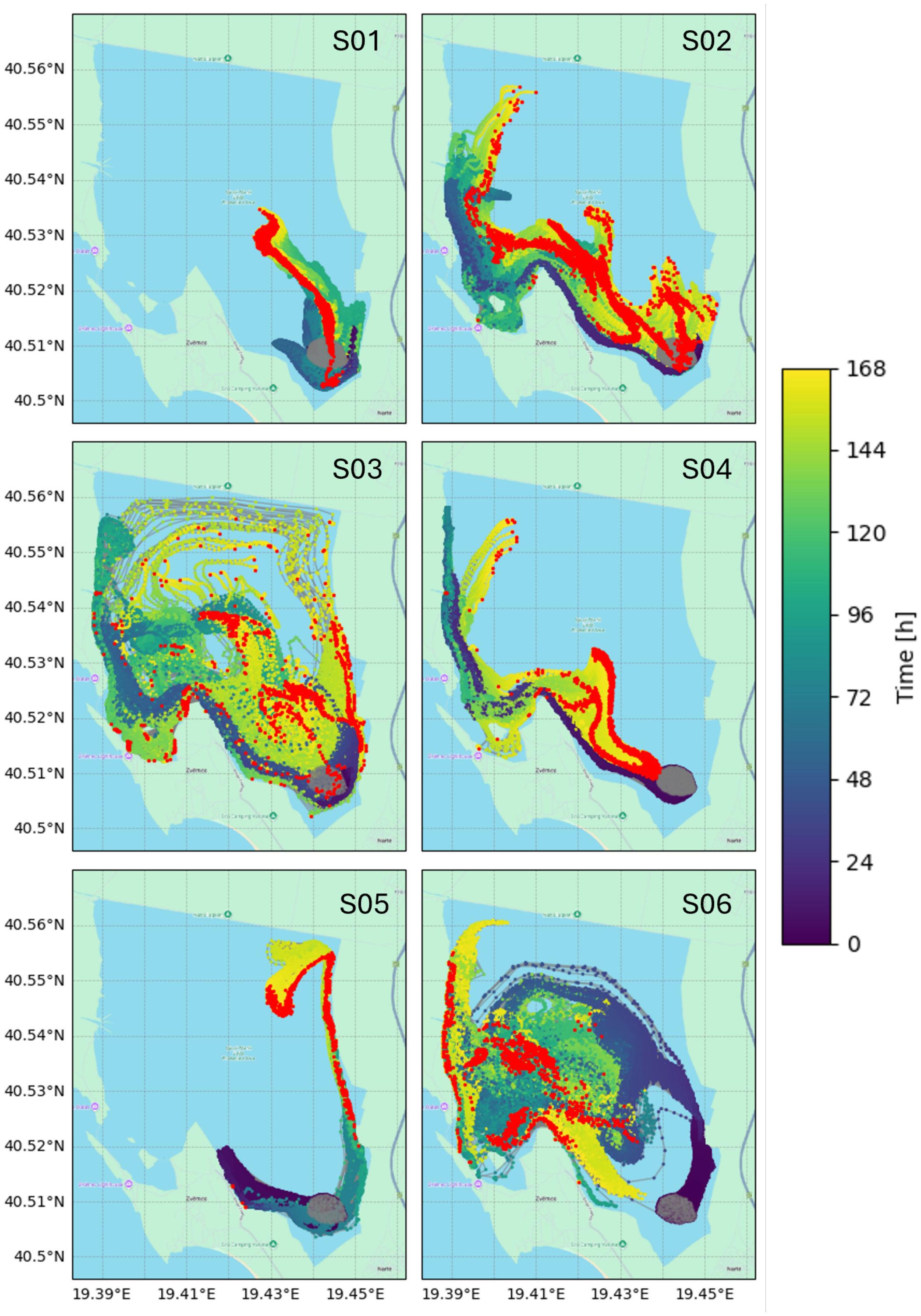

FIGURE 5.6: Trajectories of particles released in plume configuration at the Narta sewage outfall for all scenarios. The gray cloud marks the initial release area, colored trajectories indicate particle positions over time, and red dots denote final positions at the end of the simulation.

Figure 5.7 shows the resulting exposure maps for each scenario.

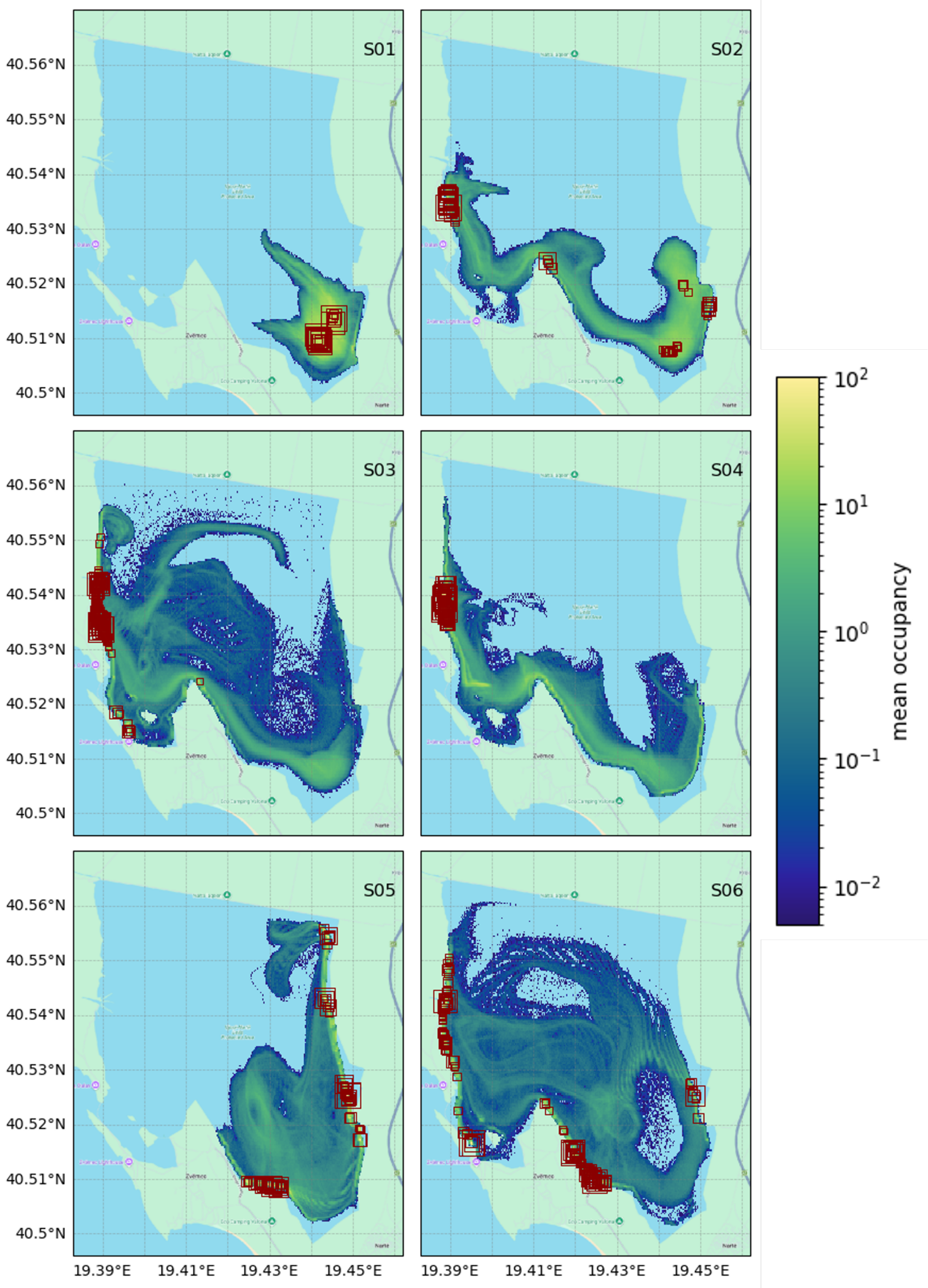

FIGURE 5.7: Particle exposure maps for the continuous plume release configuration in Narta Lagoon. Exposure is defined as the time-averaged particle count per cell over the simulation. Colours are shown on a logarithmic scale, and red boxes highlight the top 0.5% highest-exposure cells.

Exposure is quantified as the time-averaged occupancy, i.e. the mean number of particles present in each grid cell over the simulation window. Let $n_{ij}(t_n)$ denote the number of particles located inside cell (i, j) at the hourly time t_n $(n = 1, \dots, N_t)$. The cumulative particle-time (exposure) in cell (i, j) is

$$E_{ij} = \sum_{n=1}^{N_t} n_{ij}(t_n)\,\Delta t, \tag{5.10}$$

where $\Delta t = 1$ h and N_t is the total number of output times. The time-averaged occupancy is then obtained by normalising by the total duration $T = N_t \Delta t$:

$$\overline{n}_{ij} = \frac{E_{ij}}{T} = \frac{1}{N_t} \sum_{n=1}^{N_t} n_{ij}(t_n). \tag{5.11}$$

The colour scale of Figure 5.7 is logarithmic to enhance the visibility of low-occupancy areas.

By comparing Figures 5.6 and 5.7, it becomes evident that the sensitivity of plume dispersion to the release timing is scenario-dependent. Some scenarios are only weakly affected by whether the discharge is instantaneous or continuous, while others show a much stronger sensitivity.

For example, in scenario 02 the two configurations are broadly comparable: the circulation during the week tends to be relatively uniform, consistently pushing particles along the eastern shore of the lagoon. In contrast, in scenarios 04, 05 and 06, releasing particles at successive times allows them to reach areas that remain unexplored when the release occurs only at the initial time. The opposite also occurs: in scenarios 02, 03 and 04, some northernmost areas are reached only by particles that travel for a long time and arrive near the end of the simulation. In the continuous-release configuration, where particles are removed after 72 hours, these long-lived trajectories are truncated and those distant areas remain largely unaffected.

The red boxes represent cells with the highest occupancy (top 0.5%), highlighting accumulation areas. Except for scenario 01, where they remain close to the release zone, in all other scenarios they are predominantly located along the boundaries. This occurs because, even though beaching is prevented by the slip condition, particles that are driven toward the shore by the currents tend to remain confined there until the circulation pattern changes. In scenarios 02, 03 and 04, most red boxes cluster around the northern channel, indicating that the outflow associated with the open-channel hydrodynamics effectively acts as a sink for passing particles. This behaviour suggests that a dedicated closed-channel model configuration would be needed to more accurately investigate the fully closed-lagoon case.

5.1.2 Port of Genoa

For the Port of Genoa case, particles are uniformly released inside the port. Each particle is tagged according to its release sub-domain, as represented in Figure 5.8, to enable later classification of trajectories. Both slip and no-slip conditions are tested.

The output frequency is set to 5 min during the first 3 h to resolve early-stage mixing processes, and 1 h thereafter. The Lagrangian trajectories are analyzed to quantify: (i) the number of particles leaving the port through each exit; (ii) the overall probability and timing of pollutant arrival in the surrounding coastal areas (Hazard and ETA maps) and (iii) the renewal time.

Figure 5.9 shows the trajectories of particles leaving the port for scenario 01 (top panel) and scenario 20 (bottom panel). The total percentage of particles that exit the port is reported in the legend title, while the number associated with each subdomain indicates the percentage of particles leaving the port, relative to the number

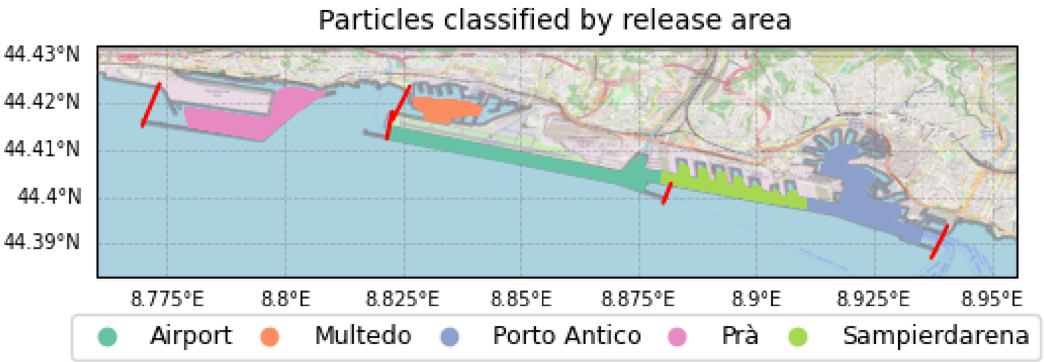

FIGURE 5.8: Particles releasing position grouped per sub-domains.

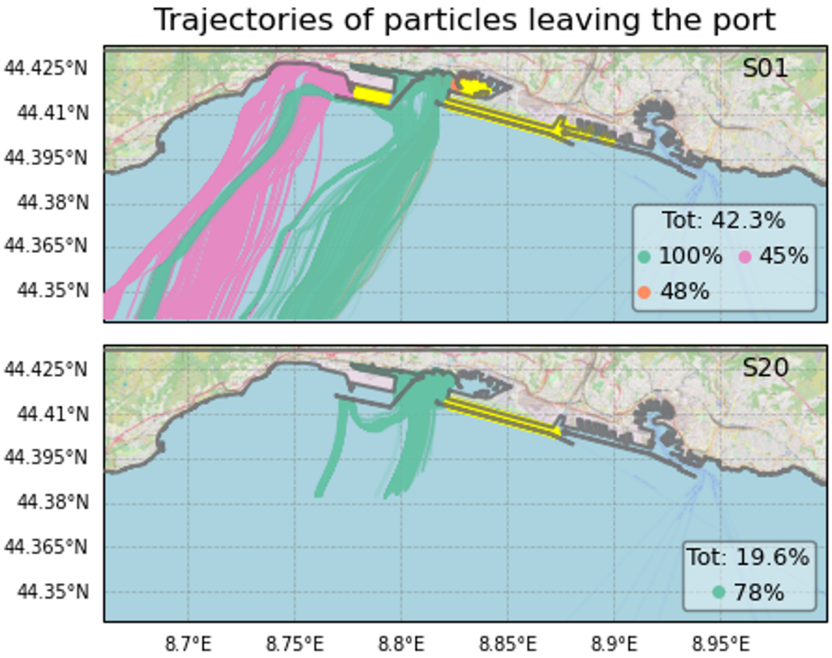

FIGURE 5.9: Trajectories of particles leaving the port for two different scenarios, with slip condition.

of particles released in that specific sub-domain. For example, in scenario 01 all particles released in the Airport channel (light blue sub-domain) leave the port.

To evaluate how efficiently the port exchanges water and floating material with the adjacent sea, the first post-processing analysis quantifies the number of particles exiting the port through each outlet. The exits, highlighted by red lines in Figure 5.8, define the boundaries across which a particle is considered to have left the port: a particle is flagged as out once its trajectory crosses one of these lines.

Figure 5.10 shows the temporal evolution of the number of particles leaving the port under slip conditions, for scenario 01 (top panel) and scenario 20 (bottom panel). The grey dashed line represents the total number of particles that exit the domain.

In both cases, particles tend to leave mainly during the first half of the simulation, while almost no particles exit in the second half. Moreover, the departures are not continuous in time but occur in distinct peaks, concentrated within relatively short time windows. This suggests that particles leave the port only when specific

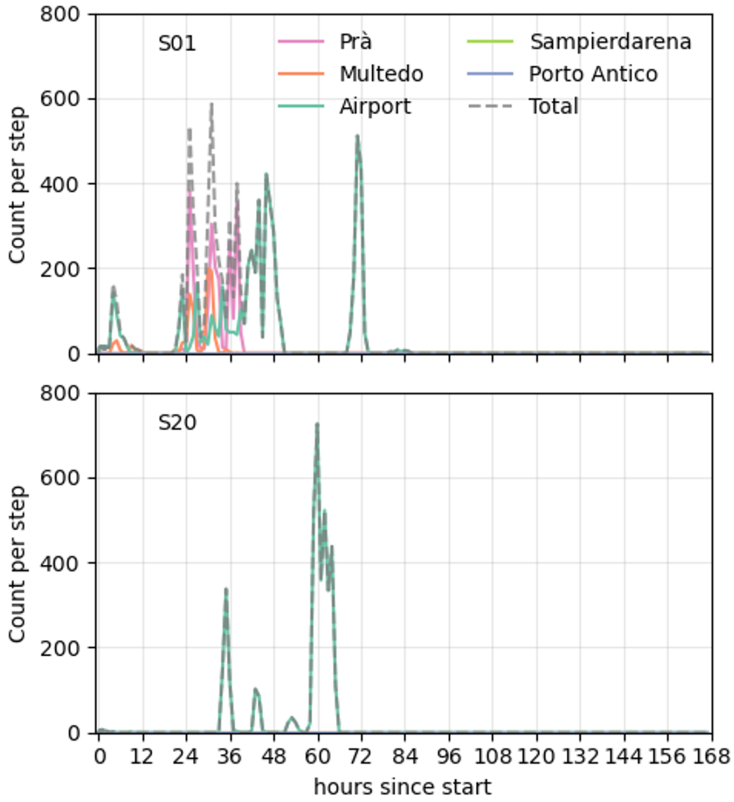

FIGURE 5.10: Temporal evolution of the number of particles leaving the port under slip conditions, for scenario 01 (top panel) and scenario 20 (bottom panel).

circulation patterns develop, temporarily guiding them towards and through the exits.

The comparison between scenarios is shown in Figure 5.11, with the no-slip condition on the top panel and the slip condition on the bottom one. The x-axis represents the scenarios' number (from 01 to 22), while the y-axis reports the percentage of particles leaving the port through each outlet, different color and marker for different sub-domain. The total percentage of particles leaving across all scenarios is indicated in the titles, approximately 8% for the no-slip and 14% for the slip case. The slip condition, which prevents particles from beaching along solid boundaries, results in nearly twice as many particles escaping from the port compared to the no-slip case. Nevertheless, even under slip conditions, the overall percentage of escaping particles remains low, indicating limited exchange between the inner basins and the open sea. This reveals that the complex harbor geometry, with numerous docks, basins, and obstacles, effectively traps most of the released particles, promoting long residence times. Consequently, the choice between slip and no-slip boundary conditions affects the magnitude but not the overall pattern of retention, confirming that the port acts as an efficient trap for surface material. Across both configurations, the dominant exit pathway is consistently the light-blue outlet. This behavior is attributed to the Airport Channel configuration, a longshore channel with two exits (left and right) that facilitates along-channel export. However, the contribution of this outlet is scenario-dependent. In the slip case (bottom panel), the light-blue outlet accounts for around 20% of the released particles in some scenarios (e.g., 01–04), whereas it becomes nearly negligible in others (e.g., 05, 07, 09).

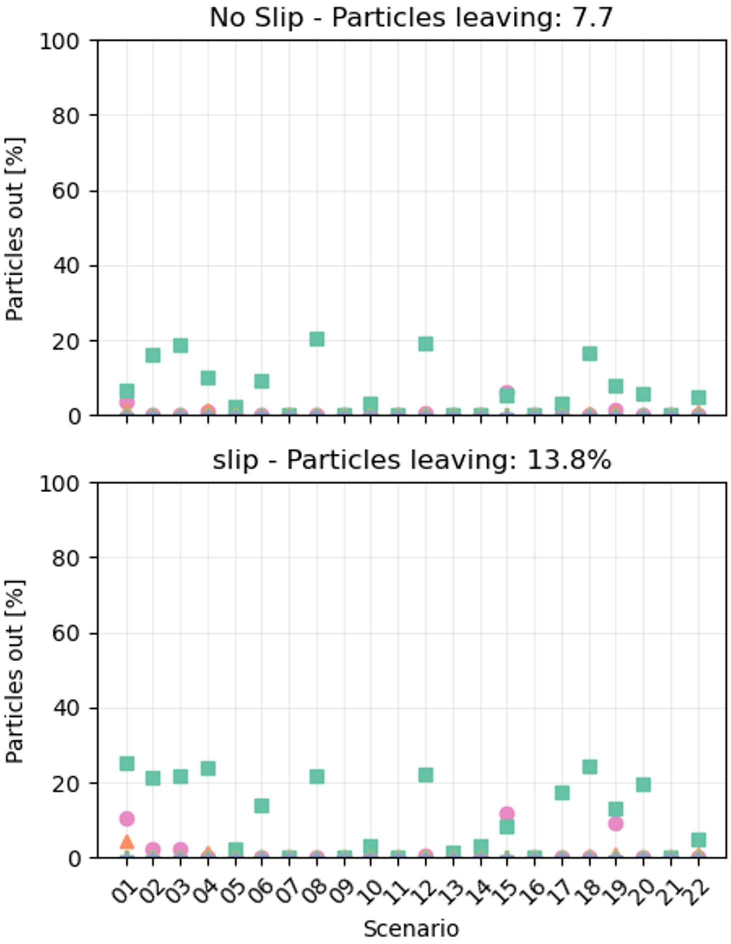

FIGURE 5.11: Comparison of the percentage of particles leaving the port through each exit under slip and no-slip conditions, for all 22 metocean scenarios.

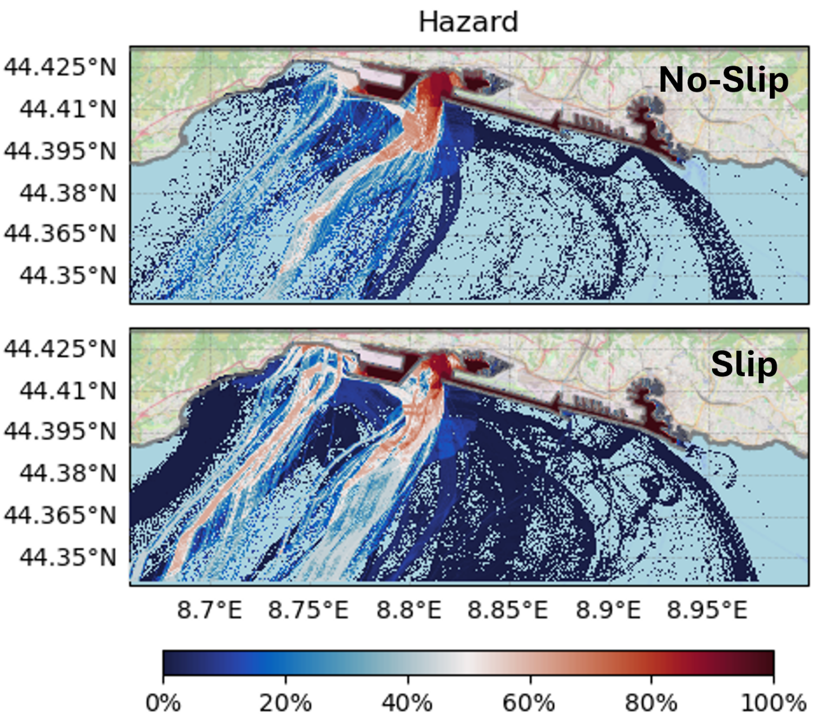

FIGURE 5.12: Hazard map for no-slip condition (top panel) and slip condition (down panel).

A second analysis summarizes all scenarios in terms of two complementary indicators: Hazard (P) and Estimated Time of Arrival (ETA). The Hazard, representing the probability of finding particles in a specific area given the probability of occurrence of each metocean scenario (P^c), is defined as:

$$P(x,y) = \sum_{c=i}^{N_c} P^c H^c(x,y), \tag{5.12}$$

where N_c is the number of metocean scenarios, P^c is the probability of occurrence of scenario c (see Table 3.1) and H^c is a binary variable indicating the presence ($H^c = 1$) or absence ($H^c = 0$) of any particle within cell (x, y).

The ETA represents the minimum time after release when the first particle reaches a given area, thus indicating the earliest possible arrival of pollution:

$$ETA(x,y) = min_{c,t}[t^c(x,y)], \tag{5.13}$$

where $t^c(x, y)$ is the time after release when the first particle from scenario c reaches that cell (x, y).

Together, these two maps help identify coastal sectors most exposed to contamination from the port: the Hazard indicates where pollution is likely to occur, while the ETA shows when it may reach the coast. In this case, the coastal area west of the port (around LON 8.75, LAT 44.415) exhibits a high probability of particle presence after 48–96 hours from release. When combined across all scenarios, the Hazard and ETA fields provide a comprehensive and conservative overview of potential exposure areas.

In addition to the Hazard and ETA maps, Figure 5.14 presents the spatial distribution of water renewal time for scenario 01 (top panel) and scenario 20 (bottom

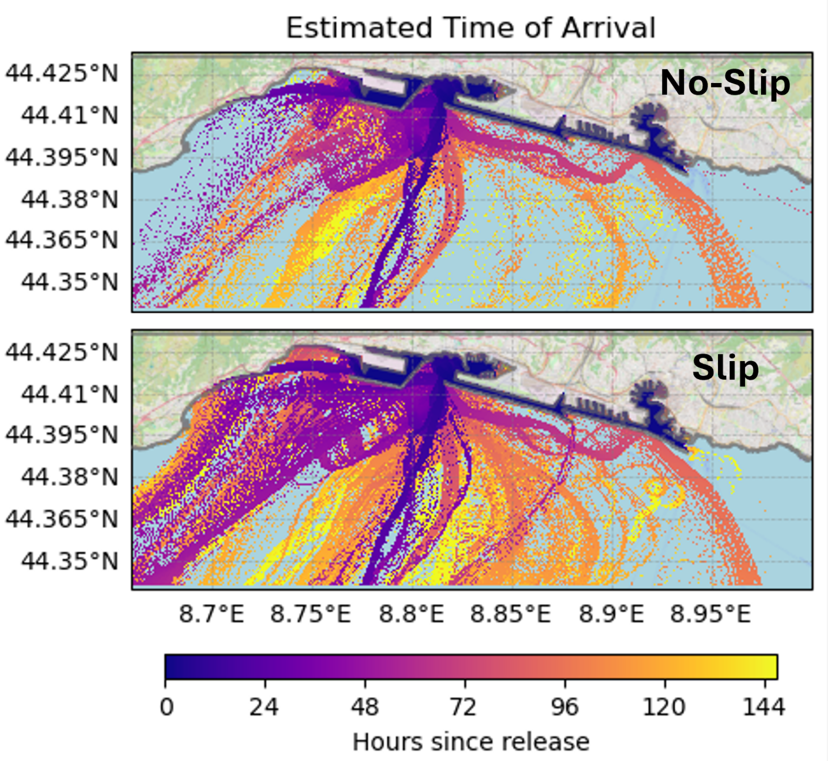

FIGURE 5.13: Minimum Estimated Time of Arrival map for no-slip condition (top panel) and slip condition (down panel).

panel), defined following Takeoka, 1984: “the residence time at a given point in a semi-enclosed coastal domain, i.e., the period required for a water parcel initially located at that point to leave the domain”. High renewal times (darker colors) identify zones of weak flushing and long residence, typically corresponding to the inner basins and docks, where structural confinement and recirculations limit hydrodynamic exchange. A particularly low renewal time is evident within the Airport Channel, a longitudinal subdomain with openings on both its eastern and western sides. This pattern is consistent with the general anti-cyclonic circulation of the Gulf of Genoa, which tends to push water into the channel from the east and out through its western gate, effectively enhancing local flushing.

Together, these three indicators, Hazard, ETA, and Renewal Time, provide a multi-perspective view of risk and transport efficiency within the port of Genoa.

5.2 Oil and HNS Simulations (Port of Genoa)

The simulation of pollutant dispersion is carried out using TESEO, a state-of-the-art 3D Lagrangian particle tracking model developed by the Environmental Hydraulics Institute (IHCantabria, Abascal et al., 2007). TESEO simulates the transport, weathering, and spatial distribution of both oil and HNS released in the marine environment. The transport module models the drift of pollutants by tracking independent Lagrangian particles, each representing a portion of the slick. The movement of these particles results from the combined influence of wind forcing, currents, and turbulent diffusion. The weathering module includes processes such as spreading, evaporation, emulsification, dissolution, volatilization, and adhesion to the coast, but the most relevant for the temporal windows under exam are evaporation and

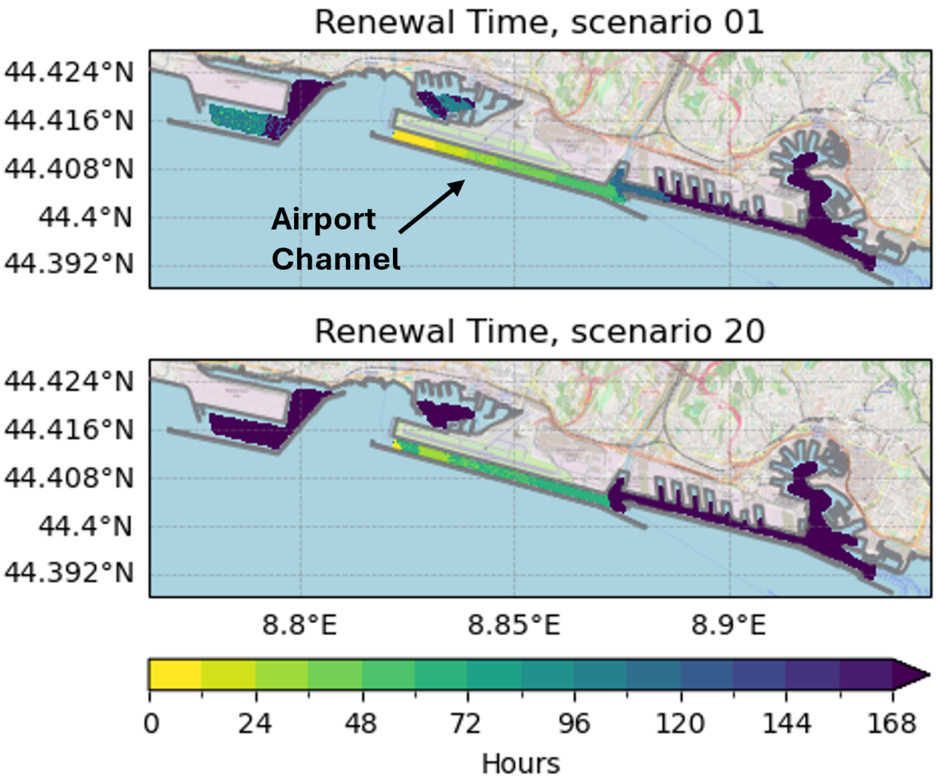

FIGURE 5.14: Spatial distribution of renewal time (in hours) for scenario 01 (top panel) and scenario 20 (bottom panel).

dissolution. TESEO has undergone extensive calibration and validation in previous studies using drifter buoys (Abascal et al., 2017a; Abascal et al., 2017b), demonstrating its robustness for real-world spill forecasting applications.

A total of 25 spill scenarios are simulated, including 12 oil spills and 13 HNS spills, strategically located in areas of the Port of Genoa considered most vulnerable to accidental releases. Figure 5.15 illustrates the selected spill location:

- the top panel shows the oil spill release points, which correspond to areas with high shipping traffic. The oil types are selected based on the fuels commonly used by different vessel categories. These include fuel oil No.1 (kerosene), typically used by cargo ships and large cruise liners, and automotive gasoline, commonly used by recreational boats.
- The bottom panel displays the HNS spill release points, positioned near chemical handling docks within the port. The chemical substances are identified based on documentation provided by the chemical companies operating in the Port itself.

The chemical and physical properties of the spilled substances are sourced from authoritative databases such as the National Center for Biotechnology Information NCBI and the European Chemicals Agency ECHA. Based on this information, substances are classified according to their behavior. All the spills information are listed in table 5.3 and 5.4, where the fifth column classifies the behavior of the substances into the following categories: G: gas; D: dissolver; E: evaporator; F: floater; S: sinker; DE: dissolver/evaporator; ED: evaporator/dissolver; FD: floater/dissolver; FE: floater/evaporator; SD: sinker/dissolver.

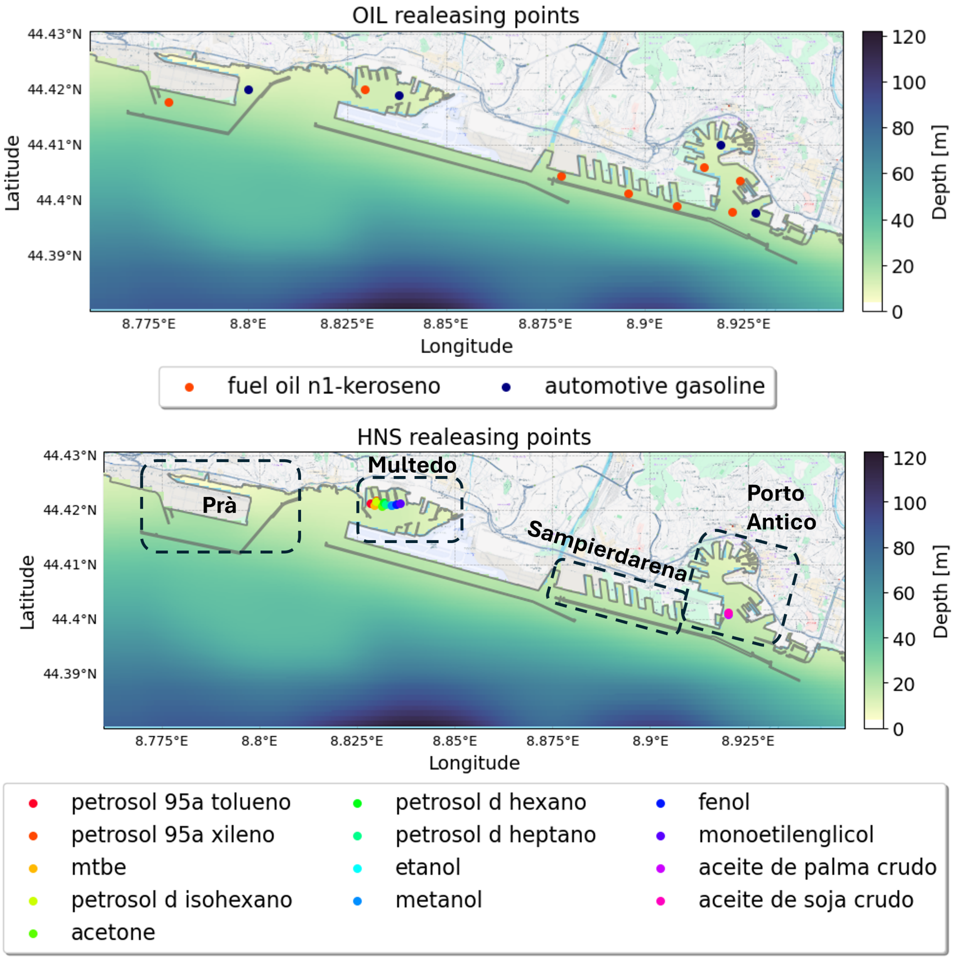

FIGURE 5.15: Releasing positions for oil (top plot) and HNS (down plot) spills.

TABLE 5.3: Oil spills simulated in the Port of Genoa.

Terminal	lat	lon	Substance	Behavior
Prà	44.417	8.780	fuel oil n1-kerosene	FE
Prà	44.420	8.800	automotive gasoline	F
Multedo	44.420	8.829	fuel oil n1-kerosene	FE
Multedo	44.418	8.838	automotive gasoline	F
Sampierdarena	44.404	8.879	fuel oil n1-kerosene	FE
Sampierdarena	44.401	8.896	fuel oil n1-kerosene	FE
Sampierdarena	44.399	8.908	fuel oil n1-kerosene	FE
Porto Antico	44.398	8.922	fuel oil n1-kerosene	FE
Porto Antico	44.000	9.000	automotive gasoline	F
Porto Antico	44.000	8.923	fuel oil n1-kerosene	FE
Porto Antico	44.406	8.915	fuel oil n1-kerosene	FE
Porto Antico	44.410	8.919	automotive gasoline	F

TABLE 5.4: HNS spills simulated in the Port of Genoa.

Terminal	lat	lon	Substance	Behavior
Multedo	44.421	8.828	toluene	FE
Multedo	44.421	8.829	xylene	E
Multedo	44.420	8.829	methyl ethyl ketone	SD
Multedo	44.421	8.829	methoxypropyl acetate	E
Multedo	44.420	8.831	acetone	SD
Multedo	44.421	8.831	hexane	E
Multedo	44.421	8.832	heptane	E
Multedo	44.420	8.832	ethanol	D
Multedo	44.420	8.833	methanol	D
Multedo	44.421	8.834	dinitrophenol	SD
Multedo	44.420	8.836	ethylene glicol	SD
Bettolo	44.400	8.919	palm oil	F
Bettolo	44.400	8.919	soy oil	F

Each simulation begins with the instantaneous release of 5 m^3 of the selected substance. This volume is chosen to represent small-scale spills, which are typically defined as having a volume below 7 tons. Internally, the model converts this volume into a corresponding number of particles based on the density of the released substance. Simulations are run for 72 hours, a period over which all substances either evaporate or adhere to port infrastructure. Seasonal temperature effects are not explored; instead, constant average conditions are assumed, with air and water temperatures set to 15.5°C and 17°C, respectively.

5.2.1 Post-processing Analysis

Figure 5.16 shows four representative simulations from the weathering module, highlighting the behavior and fate of different substances upon release into the marine environment. The top panel presents results for oil products, specifically kerosene (a heavy oil) and automotive gasoline (a light fuel). Both substances undergo evaporation shortly after release, but to varying extents: less than 20% of kerosene evaporates within the first hour, while up to 80% of automotive gasoline evaporates within the first seven hours. In both cases, the remaining fraction becomes trapped along port structures, preventing further dispersion. This behavior aligns with expectations, as automotive gasoline has a higher volatility, leading to faster evaporation, whereas kerosene, being less volatile, persists longer in the environment. The bottom panels illustrate two examples of HNS: Toluene, a highly volatile hydrocarbon with low solubility, and Ethanol, a fully water-miscible compound. After 24 hours, approximately 60% of Toluene has evaporated, while a small fraction undergoes volatilization from the water surface, and only a negligible amount dissolves into the water column. The remaining portion is trapped along port structures. In contrast, Ethanol dissolves entirely upon entering the water and subsequently begins to volatilize over time.

The spatial and temporal evolution of the pollutant slick is further assessed using the two Eulerian indicators defined for passive tracers analysis: Hazard and ETA.

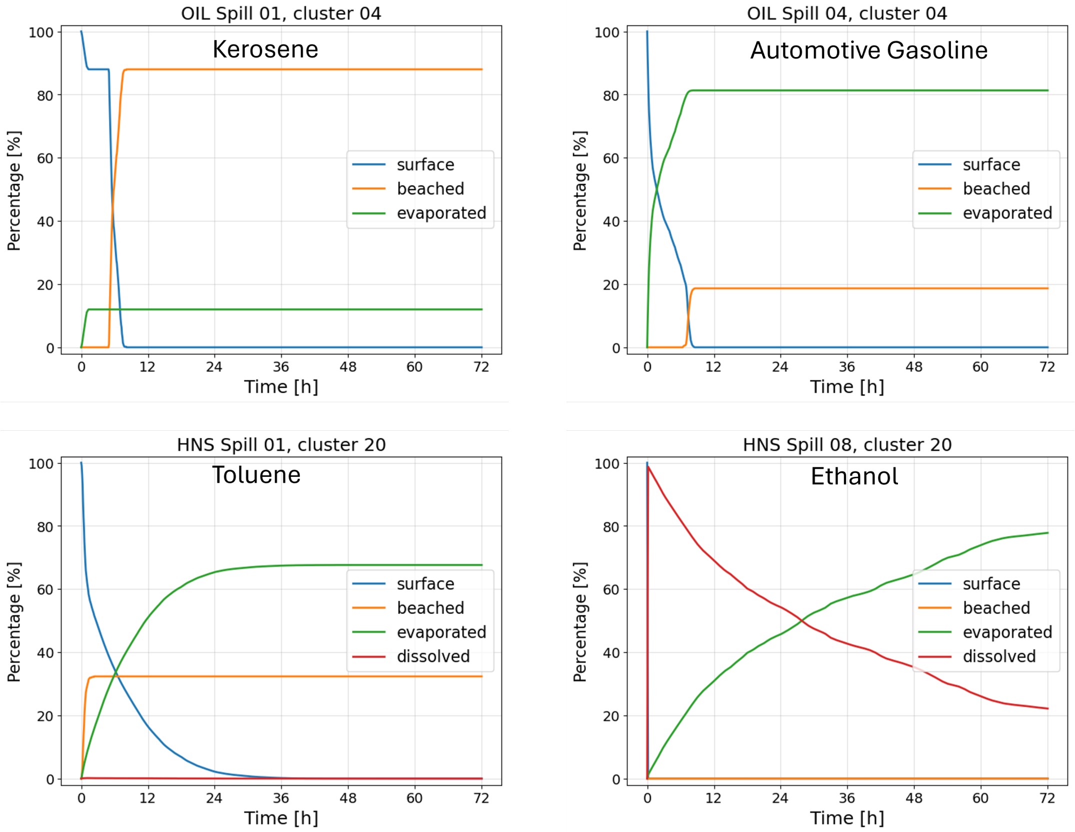

FIGURE 5.16: Weathering module results. From left to right, top panel (oil): Kerosene, Automotive Gasoline. Down panel (HNS): Toluene, Ethanol

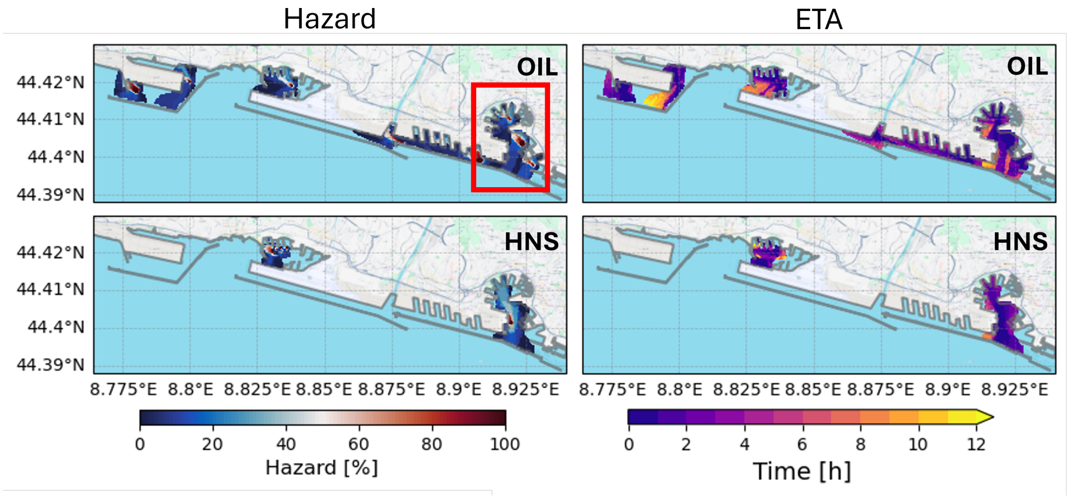

FIGURE 5.17: Left column: Hazard for oil (top panel) and HNS (down panel). Right column: minimum estimation time of arrival for oil (top panel) and HNS (down panel).

Figure 5.18 illustrates the ETA (right column) and Hazard (left column) maps for selected scenarios. For HNS spills, simulation results across 23 metocean scenarios confirm that contaminants remain confined within the port. This is primarily due to rapid weathering processes, such as evaporation or dissolution, and the tendency of non-volatile substances to adhere to port structures. The ETA plots, with a common

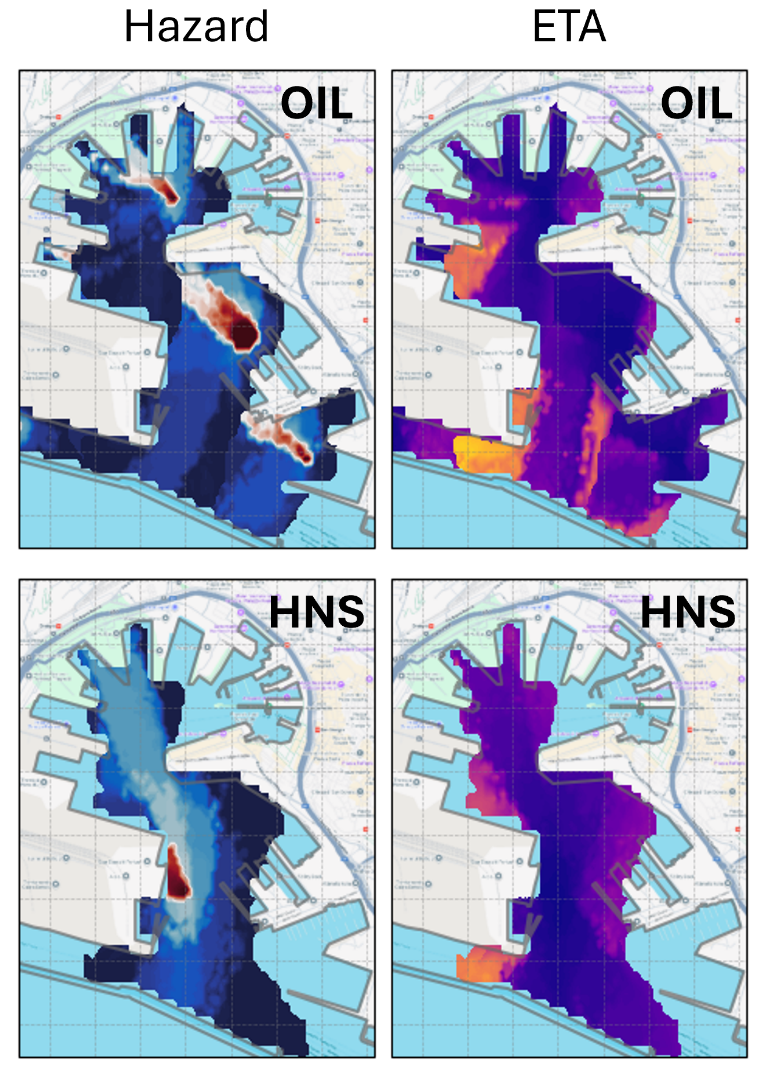

FIGURE 5.18: Zoom in Porto Antico basin. Left panel: Hazard for oil (left) and HNS (right). Right panel: minimum estimation time of arrival for oil (left) and HNS (right).

scale of 0 to 12 hours, show that the arrival time of pollutants is generally short. This highlights the critical importance of early detection and immediate response for limiting environmental impact.

5.2.2 Web User Interface

Finally, to support decision-makers in promptly taking action in case of a spill, a web-based user interface (WUI) has been developed and made freely available (PROMPT). Through this interface, the user can configure and launch simulations by specifying the main input variables, as shown in Figure 5.19. The model can be run for any of the substances listed in Tables 5.3 and 5.4; the user defines the released volume, the release position, and the start time of the spill. Environmental conditions can also be adjusted, including water and air temperature and water density, to represent different seasonal or scenario-specific configurations. The interface provides a list of all precomputed scenarios, ordered by decreasing similarity to the daily metocean forecast, so that the first cluster in the list corresponds to the

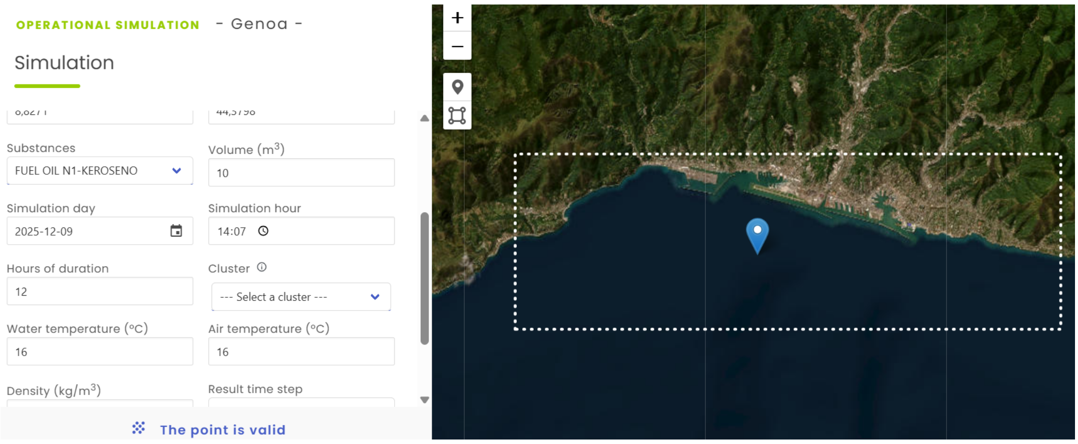

OPERATIONAL SIMULATION - Genoa -

Simulation

Substances
FUEL OIL N1-KEROSENO

Volume (m^3)
10

Simulation day
2025-12-09

Simulation hour
14:07

Hours of duration
12

Cluster
--- Select a cluster ---

Water temperature (°C)
16

Air temperature (°C)
16

Density (kg/m^3)

Result time step

The point is valid

FIGURE 5.19: WUI to configure and launch oil and HNS simulations.

closest match. Similarity between the daily forecast and each scenario is quantified by minimising the normalised Euclidean distance between them, following Daliri et al., 2025. After selecting the scenario, specifying the output time step and pressing "run", since the hydrodynamic fields are already precomputed, the system rapidly returns the results.

Model outputs are displayed in terms of the temporal evolution of the mass balance and the surface slick footprint, as illustrated in Figure 5.20. In this way, the tool provides, within a matter of minutes, a first-order picture of the expected dispersal of a pollutant. This information supports decision-makers in identifying which coastal sectors are likely to be affected, where containment booms or other response measures should be deployed, and how quickly these actions need to be implemented.

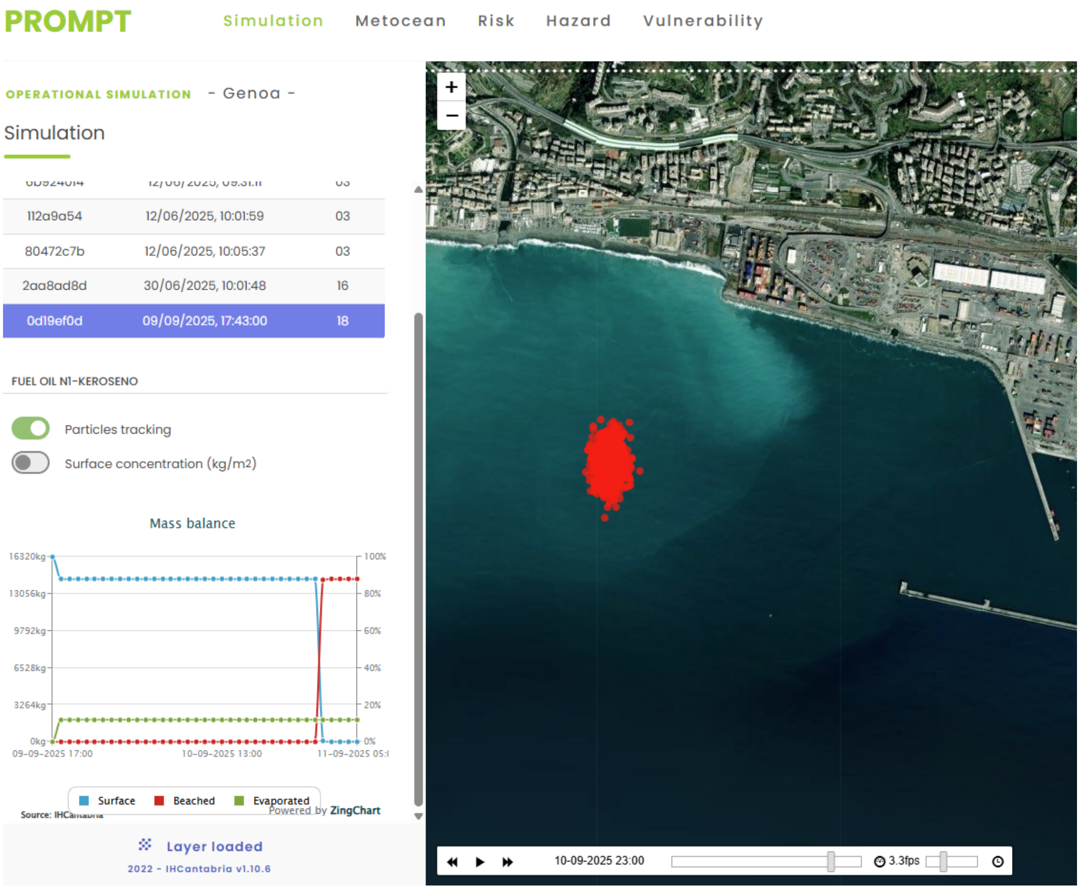

112a9a54	12/06/2025, 10:01:59	03
80472c7b	12/06/2025, 10:05:37	03
2aa8ad8d	30/06/2025, 10:01:48	16
0d19ef0d	09/09/2025, 17:43:00	18

FUEL OIL N1-KEROSENO

● Particles tracking

○ Surface concentration (kg/m2)

FIGURE 5.20: WUI output example. The graph on the left shows the temporal evolution of the mass balance, while the map represents the surface slick footprint.

Chapter 6

Mixing Properties

The previous chapter presented several Eulerian-type metrics, very suitable to investigate the ability of semi-enclosed basins to exchange water with the outer sea, or the tendency of particles to accumulate in specific areas, but that do not fully describe the underlying processes driving particle motion. To better interpret these patterns and quantify the mechanisms controlling spreading and exchange, the present chapter examines the mixing properties of the simulated Lagrangian trajectories. The mixing properties are statistical descriptors that help identifying spatial and temporal scale of the transport mechanisms (LaCasce, 2008). They are generally divided into single-particle statistics, which describe the behavior of a cloud of particles by studying the one of each individual particles, and multiple-particle statistics, which characterize the relative motion of particle pairs released at a fixed initial separation. Given that beached particles damps variability and flattens scalings, we therefore base the analysis on the slip case only, or to the no-slip case, but previously removing particles that eventually stuck.

Furthermore, from now on, only few scenarios will be taken as example, to focus the attention on different behaviors. For Narta lagoon, only simulations of the plume, both instantaneously and continuously released, are considered and results are presented for scenario 01 and 03. For Genoa case, only the first scenario, the one with the highest frequency of occurrence, will be taken as example. Before investigating the results related to each domain, a brief introduction will explain the mixing properties used.

6.0.1 Single-Particle Statistics

Concerning single-particle statistics, the first descriptor is the velocity autocorrelation function, defined as the correlation between the velocity at time t and at a later time $t + \tau$ (LaCasce, 2008):

$$R(\tau) = \frac{\langle \mathbf{u}(t) \cdot \mathbf{u}(t+\tau) \rangle}{\langle \|\mathbf{u}(t)\|^2 \rangle}, \tag{6.1}$$

where $\langle \cdot \rangle$ denotes an ensemble average over particles and $\mathbf{u}(t)$ is the velocity. As long as R is close to 1, the velocity remains strongly correlated over the time lag τ, and particle motion is persistent.

The second descriptor is the absolute dispersion, which quantifies the particle-based mean-squared displacement from the release position (LaCasce, 2008). Let $\mathbf{x}_i(t)$ be the position vector of particle i at time t and N the number of particles in the considered ensemble. The absolute dispersion is defined as

$$A^2(t) = \frac{1}{N} \sum_{i=1}^{N} \|\mathbf{x}_i(t) - \mathbf{x}_i(0)\|^2, \tag{6.2}$$

which combines both the drift of the cloud and its spreading. At early time steps A^2 grows proportionally to t^2: particle motion is ballistic, indicating that velocities remain correlated over the considered time scale. At later time steps A^2 grows linearly with t, revealing a diffusive regime where velocities lose correlation.

The first two descriptors are connected by the Lagrangian time (T_L), defined as the time integral of the autocorrelation function. T_L provides an estimate of the time scale over which A^2 deviates from ballistic growth.

The drift of the cloud as a whole is characterized through the displacement of its center of mass. The ensemble centroid is

$$\overline{\mathbf{x}}(t) = \frac{1}{N}\sum_{i=1}^{N}\mathbf{x}_i(t), \tag{6.3}$$

which is dominated by coherent advection. The squared displacement of the center of mass is

$$A_c^2(t) = \left\|\overline{\mathbf{x}}(t) - \overline{\mathbf{x}}(0)\right\|^2 . \tag{6.4}$$

To isolate the spreading of the particle cloud around its drifting centroid, the dispersion relative to the center of mass can be computed

$$R_c^2(t) = \frac{1}{N}\sum_{i=1}^{N}\left\|x_i'(t)\right\|^2 . \tag{6.5}$$

where $\mathbf{x}_i'(t) = \mathbf{x}_i(t) - \overline{\mathbf{x}}(t)$ defines the centered positions at time t. R_c describes the instantaneous width of the particle cloud at time t.

Finally, to quantify whether the particle cloud spreads preferentially along one horizontal direction, an anisotropy metric, bounded between -1 and 1, is computed from the second central moments of the centered positions

$$AN(t) = \frac{\sigma_x^2(t) - \sigma_y^2(t)}{\sigma_x^2(t) + \sigma_y^2(t)}. \tag{6.6}$$

Here

$$\sigma_x^2(t) = \frac{1}{N}\sum_{i=1}^{N} x_i'(t)^2, \qquad \sigma_y^2(t) = \frac{1}{N}\sum_{i=1}^{N} y_i'(t)^2, \tag{6.7}$$

are the variances of the centered positions along the x– and y–axes, respectively. Values $AN > 0$ indicate a preferential stretching along the x–direction, $AN < 0$ along the y–direction, and $AN = 0$ corresponds to an isotropic spread in these coordinates.

6.0.2 Narta Lagoon

For Narta Lagoon, only two scenarios are analysed, namely scenario 01 (S01) and scenario 03 (S03). Starting from the single release at $t = 0$ h,

Figure 6.1 shows the Lagrangian velocity autocorrelation for the u (blue) and v (orange) components; lighter lines correspond to individual trajectories, while darker lines indicate the ensemble mean. A marked difference emerges between the two scenarios. In S01, the autocorrelation remains persistent and exhibits a clear oscillatory pattern, particularly for the u component, indicating the presence of coherent and/or periodically forced motions. In contrast, in S03 the autocorrelation decays rapidly toward zero, suggesting a much shorter Lagrangian memory time

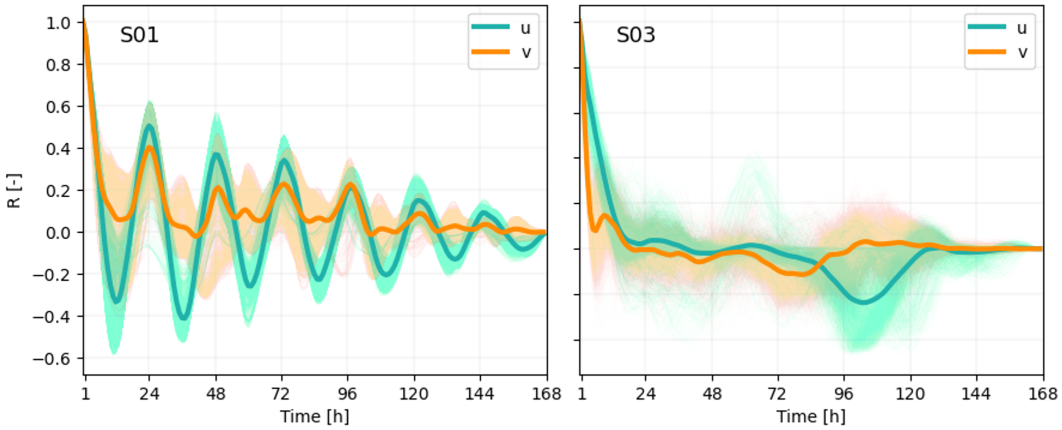

FIGURE 6.1: Lagrangian velocity autocorrelation for Narta Lagoon scenarios S01 (left) and S03 (right). Blue and orange denote the u and v components, respectively. Thin lines correspond to individual trajectories, while thick lines show the ensemble mean.

scale and a more rapidly decorrelating flow. These behaviors are consistent with the wind forcing shown in Figure 6.2, where periodic components are evident for S01 (top panel), while they are absent in S03 (bottom panel).

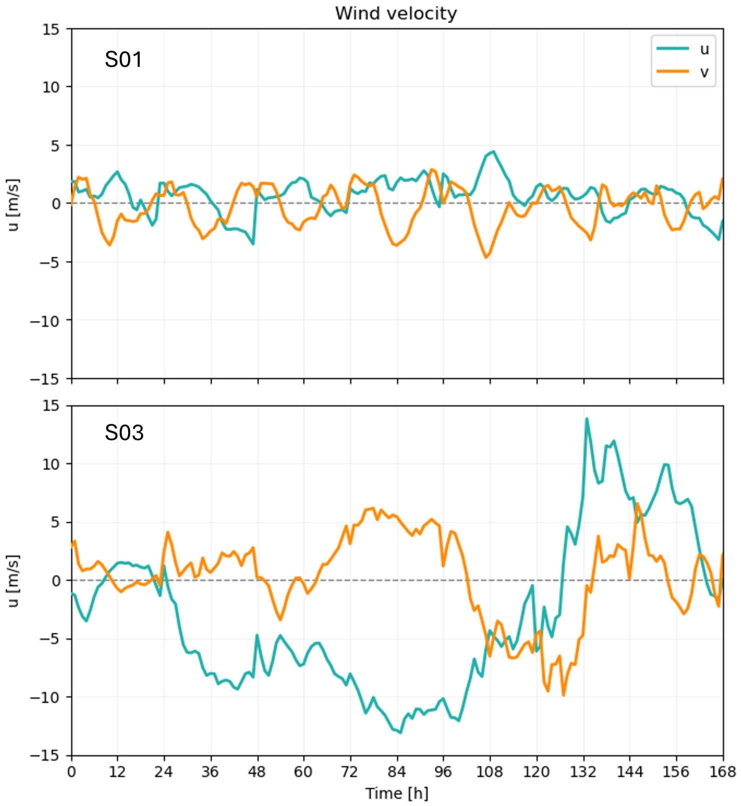

FIGURE 6.2: Wind velocity components for scenario 01 (top panel) and scenario 03 (down panel). Blue line represents the u component, while orange line represents the v component.

In terms of particle dispersion, the previous analysis suggests that in S01, particles move as a coherent cloud, reversing direction approximately every 12 hours;

while in S03, particles spread more individually, without the same periodic structure.

Figure 6.3 displays the spatial distribution of the absolute dispersion A^2 of the released plume at $t = 168$ h. The A^2 is normalized between 0 and 1, so the focus is not on how far particles go, but on behavioral differences within the plume. Despite the relatively small release region, S01 exhibits a distinct spatial structure, with areas characterised by low A^2 (particles remaining close to their release locations) and areas with high A^2 (particles experiencing larger net displacements). Conversely, S03 shows a more spatially scattered pattern, with less clear separation between low- and high-dispersion regions, consistent with the faster decorrelation observed in the velocity autocorrelation.

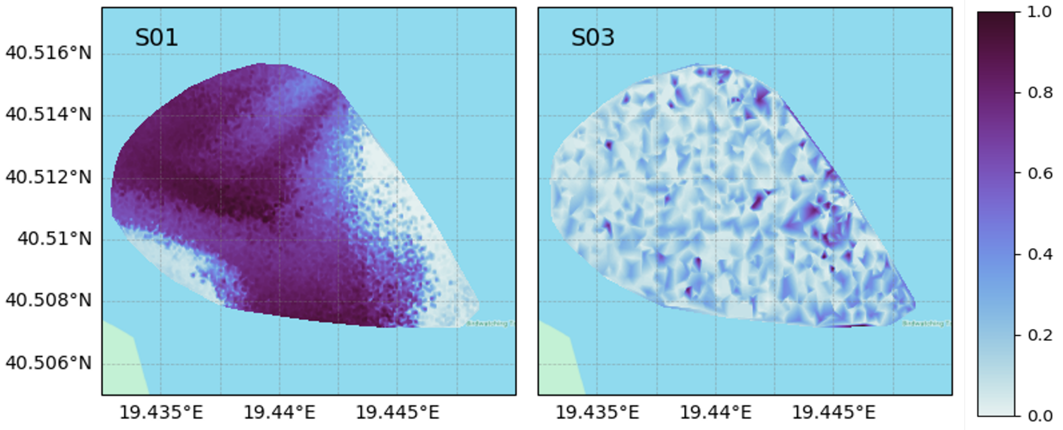

FIGURE 6.3: Spatial distribution of absolute dispersion A^2 at $t = 168$ h for Narta Lagoon scenarios S01 (left) and S03 (right).

Mixing descriptors are also applied to the continuous-release experiment. Figure 6.4 compares S01 (left column) and S03 (right column), where each colour denotes a different release cohort. The analysis for different scenarios yields different y-axis values, as the focus is not on the magnitude differences between the descriptors across scenarios, but rather on the behavior of different cohorts within the same scenario. The first row shows the absolute dispersion $A^2(t)$. In S01, cohorts exhibit broadly similar behaviour, indicating limited sensitivity to release time. In S03, by contrast, cohorts released earlier (light blue colours) differ substantially from those released later (violet colours), highlighting a pronounced dependence on release timing. The $A^2(t)$ curves for the early-released cohorts exhibit a weak initial slope, suggesting that the flow first tends to keep particles close to their release positions before spreading them farther away.

To disentangle whether these differences originate from coherent transport or from plume spreading, the second and third rows report the squared displacement of the center of mass, $A_c^2(t)$, and the dispersion relative to the center of mass, $R_c^2(t)$, respectively. Consistent with $A^2(t)$, S01 shows only minor inter-cohort variability in both drift and spreading. In S03, the cohort-to-cohort differences are primarily expressed in the drift term $A_c^2(t)$, whereas the spreading term $R_c^2(t)$ remains comparatively similar across cohorts. This indicates that the sensitivity to release time in S03 is mainly controlled by changes in advective pathways rather than by changes in the intensity of spreading, which results in particles of the same cohort being transported coherently.

The last row shows the anisotropy metric. In both scenarios, the particle cloud tends to be elongated predominantly along the x direction during the first part of the simulation and shifts toward preferential elongation along the y direction later in time, suggesting a change in the dominant deformation axis of the plume. For scenario 03, the anisotropy tends toward zero in the final part of the simulation, indicating that particles become isotropically mixed within the lagoon.

6.0.3 Port of Genoa

For the second domain, trajectories are examined either as a single ensemble or grouped by the previously defined sub-domains, separating particles that remain inside the port (IN) from those that eventually leave it (OUT). Sub-domains where all particles remain trapped are excluded. The first descriptor is the velocity autocorrelation function. The gray curves in the left panel of Figure 6.5 show the autocorrelation of each individual trajectory. They reveal highly variable behaviors, with both positive and negative trends, reflecting the chaotic and independent nature of single-particle motion within the port. The ensemble-mean signal (blue line) smooths these differences: the correlation quickly decays to zero, resulting in a decorrelation time $T_L = 1.65$ h. After decorrelation, the signal exhibits a weak negative branch (minimum around –0.2) before slowly returning toward zero by the end of the simulation. This persistent mild anti-correlation indicates frequent velocity reversals, consistent with particles turning or retracing their paths within the complex geometry of docks and basins. The lack of oscillations around zero also suggests that tidal forcing is not the dominant driver of motion.

The sub-domain averages (bottom panel in 6.5) show broadly similar behaviors, suggesting that the decorrelation process is spatially homogeneous across the port. Only the three sub-domains from which a fraction of particles escapes are shown (see Figure 5.9); for the light-blue basin, where all particles exit, only the dashed line (OUT case) is plotted. Dashed lines refer to particles that eventually leave the port, but the averaging is performed from the release time rather than from the moment of exit. Consequently, the early part of each OUT curve includes both particles still confined inside and others already drifting outside, slightly damping potential differences. Even after all particles have exited (approximately at 72 h, see Figure 5.10), dashed and solid lines remain remarkably similar, indicating that the temporal scales of velocity correlation are comparable inside and outside the harbor.

The left panel of Figure 6.6 shows A^2 for each particle (gray lines) and the ensemble mean (blue line). The broad scatter of the gray lines again confirms the diversity of individual behaviors, while the ensemble mean clearly displays an initial ballistic regime ($\propto t^2$), which extends even beyond the decorrelation time T_L. This apparent persistence occurs because, although particles lose correlation with their initial velocity after T_L, their subsequent motion can still remain directionally consistent over short intervals if they are advected by coherent, slowly varying flow structures. In other words, the autocorrelation captures the memory of velocity fluctuations, while the absolute dispersion measures the accumulated displacement, which can continue growing quadratically for some time even after decorrelation. After approximately four hours, the curve alternates between nearly flat segments and sharp increases. This intermittency arises from ensemble heterogeneity: some particles remain trapped in port's basins, while others escape through the harbor mouths and are rapidly advected along preferential pathways. The latter events produce super-diffusive bursts in the ensemble average, leading to abrupt increases of A^2.

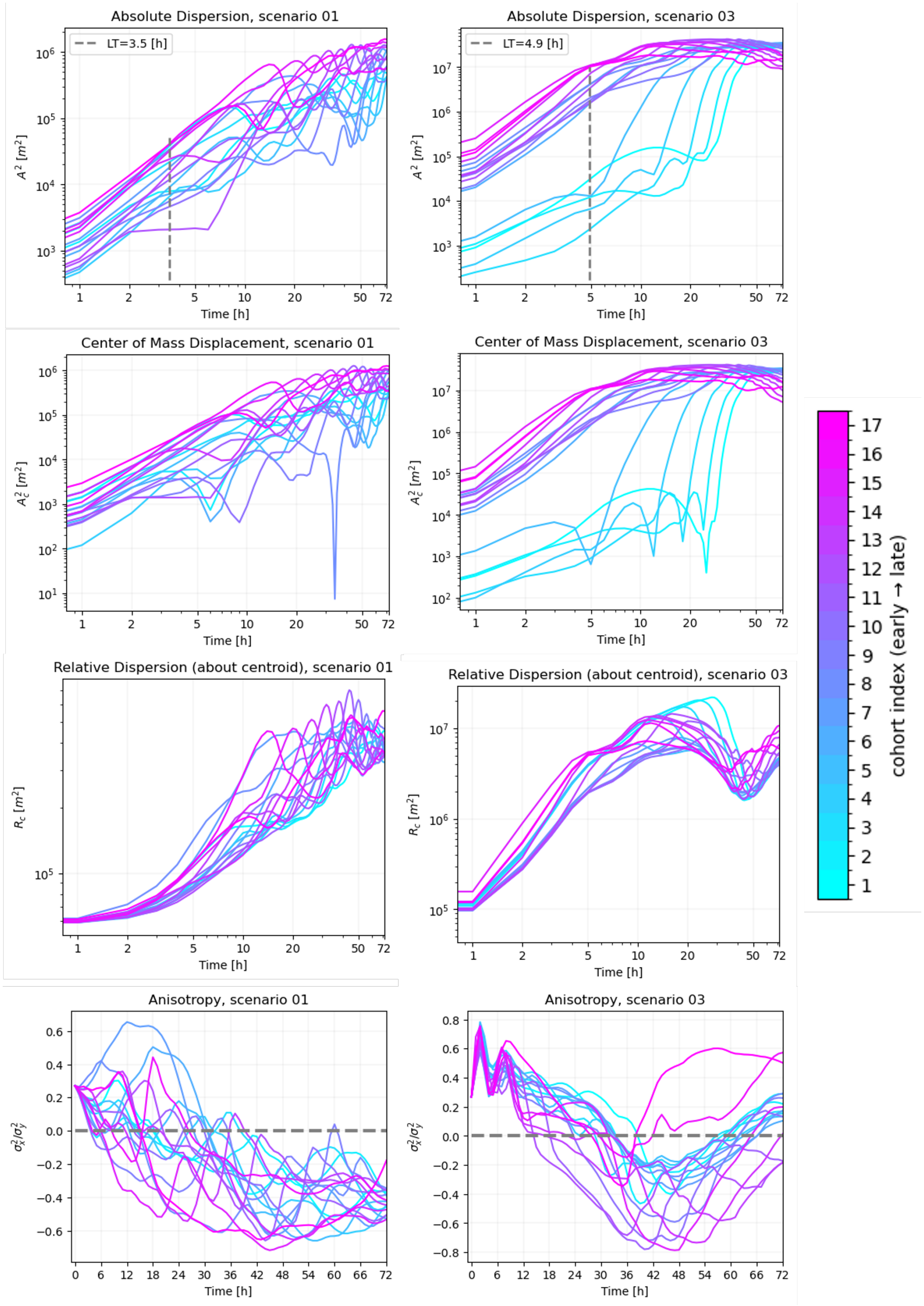

FIGURE 6.4: Mixing descriptors for the continuous-release experiment in Narta Lagoon, comparing scenarios S01 (left column) and S03 (right column). Colours denote different release cohorts (earlier releases in lighter tones, later releases in darker tones). From top to bottom: absolute dispersion $A^2(t)$; squared displacement of the center of mass $A_c^2(t)$ (drift); dispersion relative to the center of mass $R_c^2(t)$ (spreading); and anisotropy metric (preferential deformation axis).

As done for the autocorrelation, the bottom panel of Figure 6.6 compares ensemble mean-square displacements for the different sub-domains, separating particles

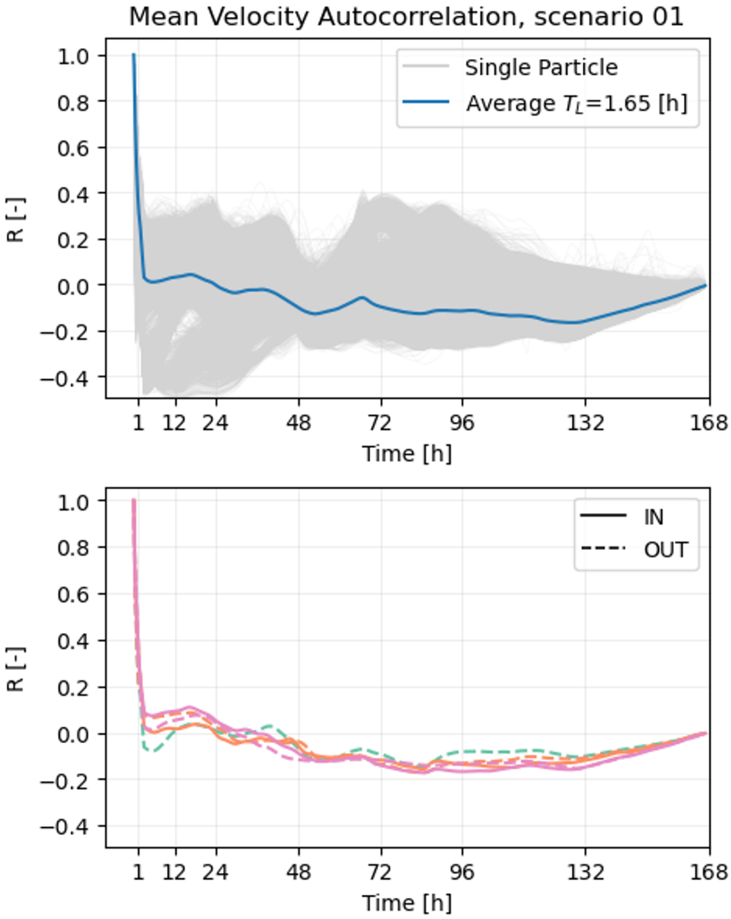

FIGURE 6.5: Velocity autocorrelation. Top panel: gray lines represent each particle, blue line represents the average. On the bottom panel, only sub-domain form which particles leave are reported (different color for different sub-domain). Solid lines represent particles staying inside the port, dashed lines represent particles leaving.

that remain inside the port (solid lines) from those that exit (dashed lines). Both groups share a similar initial ballistic regime, consistent with comparable decorrelation times. Subsequently, the signals diverge: solid lines exhibit alternating plateaus and weakly negative slopes, indicative of sub-diffusive behavior caused by confinement-limited transport and trapping within basins. In contrast, the dashed curves alternate between quasi-stationary phases and sharp increases, mirroring the behavior of the ensemble average. These bursts correspond to subsets of particles escaping through specific outlets and being rapidly advected offshore, yielding transient super-diffusive behavior.

6.1 Multiple-Particle Statistics

Rather than focusing on individual trajectories, multiple-particle statistics describe the evolution of particle pairs initially released with a given separation.

Mixing is characterized through the relative diffusivity, obtained by grouping particle pairs according to their initial separation r_0 and evaluating:

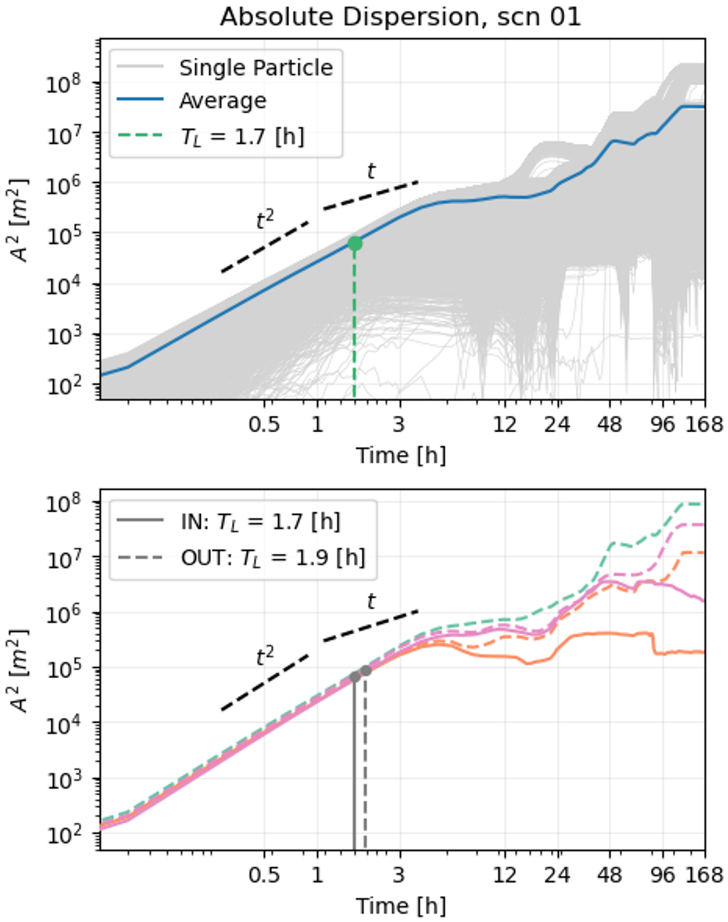

FIGURE 6.6: Absolute Dispersion. Top panel: gray lines represent each particle, blue line represents the average. On the bottom panel only sub-domain form which particles leave are reported (different color for different sub-domain). Solid lines represent particles staying inside the port, dashed lines represent particles leaving.

$$K(r) = \frac{1}{2}\frac{d}{dt}\langle r^2 \rangle, \tag{6.8}$$

as a function of the instantaneous separation r. The relative diffusivity quantifies the scale-dependent efficiency of the flow in separating pairs of particles initially released close to each other. Its scaling with r distinguishes between different dispersion regimes. In the inertial-range (Richardson–Obukhov) regime, $K \sim r^{4/3}$, indicating separation driven by turbulent eddies across a hierarchy of scales. In the smooth-strain (Batchelor) regime, $\sim r^2$, corresponding to locally smooth velocity gradients and exponential growth of pair separation.

Complementary to $K(r)$ the Finite Size Lyapunov Exponent ($FSLE$) measures the average rate of separation of two particles initially separated by a distance r_0 (Artale et al., 1997):

$$\lambda(r_0) = \frac{ln(c)}{\langle \tau(r_0, c) \rangle}, \tag{6.9}$$

where τ is the first-passage time for a pair to grow from r_0 to cr_0 and c is a scaling factor. While the relative diffusivity $K(r)$ is derived from the time evolution of the mean-square separation at fixed times, thereby mixing the behavior of particle pairs with potentially very different separation histories, the *FSLE* adopts a scale-based viewpoint. In the *FSLE* framework, the separation distance is treated as the independent variable, and one measures the average time required for particle pairs to grow between prescribed separation scales. This first-passage-time approach conditions statistics on spatial scale rather than on time, making the *FSLE* particularly well suited for inhomogeneous and finite domains, where different regions of the flow may contribute very differently to pair dispersion at the same physical time.

Together, $K(r)$ and the *FSLE* provide complementary descriptions of scale-dependent mixing, the former emphasizing time-based dispersion rates and the latter emphasizing the flow's ability to separate particles across spatial scales

6.1.1 Port of Genoa

Since the single-particle analysis revealed no major differences among sub-domains, here we restrict the comparison to particles that remain inside the port for the whole simulation (solid lines, or IN) and those that eventually leave it (dashed lines, or OUT).

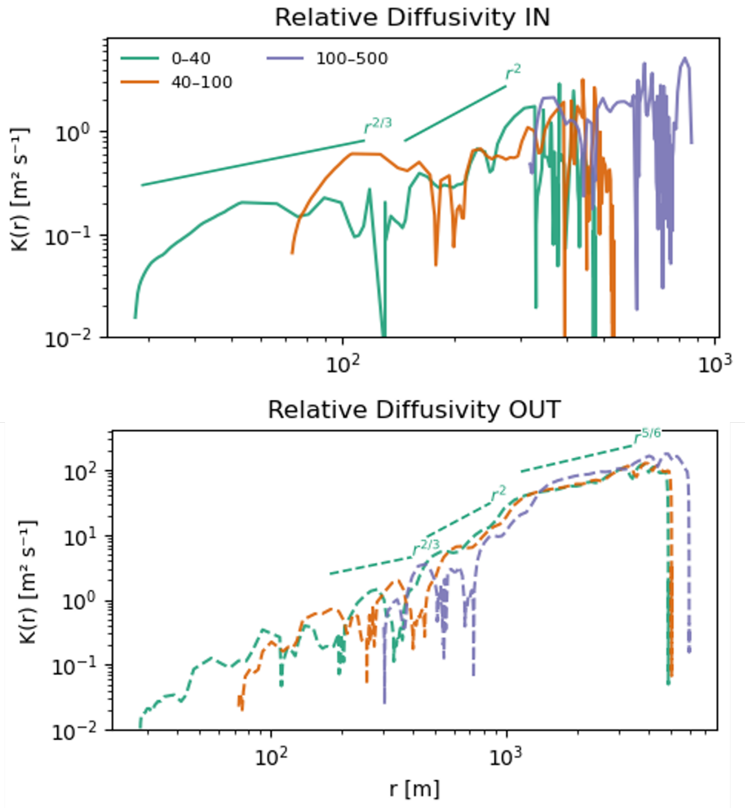

FIGURE 6.7: Relative diffusivity $K(r)$ for pairs remaining inside (top panel, solid lines) and leaving the port (bottom panel, dashed lines). Reference slopes $r^{4/3}$ and r^2 indicate Richardson–Obukhov and Batchelor regimes, respectively

In Figure 6.7, three representative initial classes are shown for IN (top panel) and OUT (bottom panel): 0–40 m (light blue) and 40–100 m (orange), 100-500 m (blue). Black dashed segments indicate the canonical slopes $K \sim r^{4/3}$ and $K \sim r^2$.

At small separations, both IN and OUT curves show similar behavior, consistent with pair separations initially governed by local shear and turbulent-like fluctuations rather than large-scale advection. The weak initial slope ($\propto r^{2/3} \sim r^{4/3}$) indeed reflects a cascade-like regime in which unsteady shear and chaotic stretching promote relative dispersion.

As r increases, the curves approach a steeper slope $\propto r^2$, consistent with the smooth-strain regime, where particle pairs are stretched by large-scale velocity gradients that are nearly uniform in space and slowly varying in time, leading to approximately exponential growth of their separation. However, the transition occurs at different separations for IN and OUT trajectories because confinement limits pair expansion inside the basins, while outside pairs continue to grow until they align with the mean outflow. At larger separations, OUT lines exhibit a gentler growth (approximately $r^{5/6}$), indicating that pairs leaving the port tend to co-move within coherent outflow jets or filaments. These results highlight the spatially heterogeneous dynamics of particle dispersion inside and outside the port.

Finally, the curves flatten and approach zero at limiting separations, roughly between 0.5-1 km for IN and 4-6 km for OUT pairs. This plateau marks the finite-size effect: once the average pair separation reaches the characteristic length of the domain, further separation ceases to increase. The fact that $K(r)$ for OUT particles saturates well below the full model scale ($\approx$ 30 km) indicates that outside the port, particles are advected coherently within narrow outflow filaments, confirming the absence of fully developed mixing at the open scale.

Additionally, the Finite-Size Lyapunov Exponent (FSLE) is computed by treating all released particles as a single ensemble, without distinguishing between those that remain inside the port and those that leave it.

Linear interpolation in r^2 is used to estimate sub–time-step crossings and the median over crossers in each r_0 bin to reduce sensitivity to outliers. Different values of c are tested ($c \in [1.2, 1.5, 1.8, 2]$) across different separation classes r_0. Increasing c means smooth out small-scale effects, so, a single, robust c, is chosen as the smallest one that allows for the highest number of bins crossing the threshold: r_0 bins whose crossing fraction (crossers/total pairs) is $\geq$ 50% (bins below the threshold are flagged with red markers in Figure 6.8).

According to this criterion, the best value is $c = 1.2$, consistent with previous studies (Stocchino et al., 2011). The light blue line is the only one showing an oscillation for separation closer to 1 km, the cause of which will be explained here after. $c = 1.2$ is therefore used to compute the FSLE for each scenario. The bottom panel of Figure 6.8 shows the FSLE results for scenario 01, again with red marks for bins where crossing fraction is $\leq$ 50%.

At the smallest resolved separations, the FSLE curve exhibits an approximate plateau, indicating a scale-independent separation rate. This is consistent with a smooth-strain regime, where particle pairs are stretched by quasi-steady velocity gradients and their separation grows approximately exponentially in time. In this range (distances of order 30–300 m), most pairs are still inside the port and are influenced by a combination of mean shear associated with the harbour geometry and unresolved, turbulent-like fluctuations.

Following this, the signal shows some oscillations (between separations of 400 and 800 meters), which likely arise from periodic interactions with localized flow features, such as eddies, recirculations, or transient jets. These fluctuations represent the complex, intermittent nature of relative separation in regions where pairs experience varying degrees of shear and turbulence.

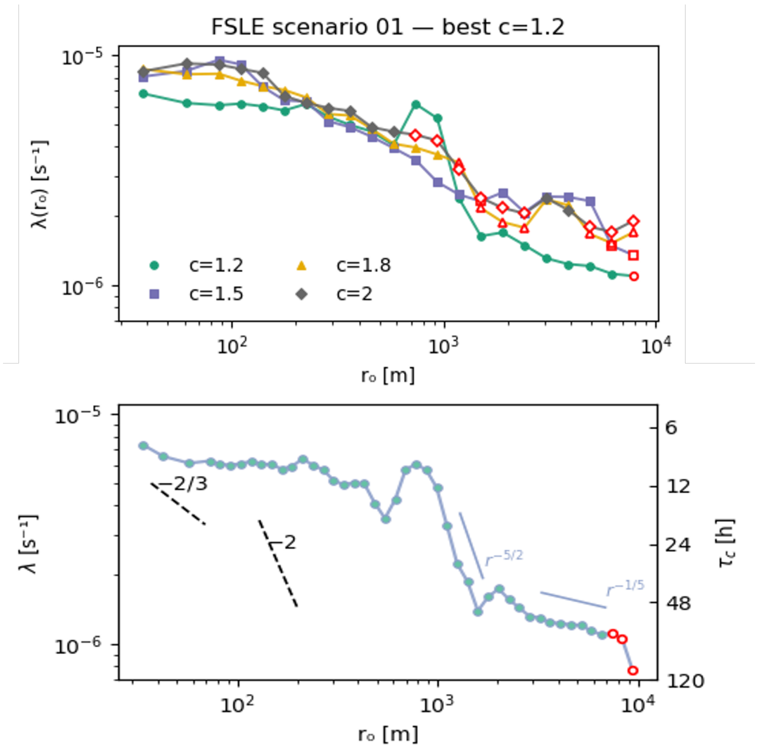

FIGURE 6.8: Top panel: FSLE for scenario 01 in function of different scaling factors c. Down panel: FSLE for scenario 01 for the chosen scaling factor $c = 1.2$.

After the oscillations, the curve shifts to a smoother decay, with the FSLE slope becoming almost vertical and following a power law of the form $\lambda(r) \propto r^{-5/2}$. This behavior is typical of the diffusive regime, where the separation of pairs is dominated by smooth, large-scale velocity gradients rather than local turbulence. At these separations a lot of particles have left the port and are experiencing a larger-scale advection.

Beyond separations of approximately 1 km, the FSLE curve changes slope to $r^{-1/5}$, reflecting the transition to weak diffusion, possibly due to larger-scale coherent motion in the flow. Finally, the FSLE signal reaches saturation at around $r = 10$ km, indicating that particle pairs have reached the limit of their possible separation due to the finite domain of the system, marking the end of the diffusive process.

Chapter 7

Discussion

In this work, a unified Eulerian and Lagrangian modeling framework was developed and applied to two contrasting semi-enclosed coastal systems: Narta Lagoon and the Port of Genoa. Although these environments differ markedly in their morphology, forcing regimes and management priorities, they share a common feature: a limited exchange of water with the open sea, which controls both their ecological functioning and their vulnerability to contamination. By combining long-term metocean statistics, high-resolution hydrodynamic simulations and Lagrangian particle tracking, the thesis investigates how circulation patterns and water exchange modulate transport, retention and dispersion processes in these semi-enclosed basins.

The adopted approach is based on a library of representative scenarios, extracted from a 40-year hindcast through clustering techniques, and used to force dedicated Delft3D setups for each case study. In both domains, the resulting velocity fields are employed to simulate the dispersion of passive tracers, while in the Port of Genoa additional experiments are carried out for oil and hazardous and noxious substances (HNS), including a calibration of the wind drag coefficient against drifter trajectories. In both domains a quantitative analysis of mixing properties reveals difference in inner and outer transport dynamics, or in releasing particles at different times. The scenario-based strategy was designed to capture the essential variability of metocean conditions while remaining computationally affordable and suitable for rapid response applications.

The practical applicability of this framework lies in its transferability. Unlike localized forecasting systems which often suffer from computational "myopia," our scenario-based library identifies bottleneck zones and high-risk retention areas under varying meteorological conditions. In the context of hindcast analysis, while existing studies (e.g. Zannella et al., 2007) focus on specific hydrodynamic phenomena, our approach provides a statistical "atlas" of transport outcomes. This allows harbor authorities to move from reactive management—where decisions are made during an emergency—to proactive management, where operational protocols are designed around pre-computed, high-probability environmental scenarios. The identification of accumulation zones in the Port of Genoa, for instance, provides actionable data for the positioning of static containment booms or infrastructure expansion.

The following discussion synthesises the main findings obtained for Narta Lagoon and the Gulf of Genoa, highlighting the common mechanisms and key differences that emerge across the two systems. It examines how basin geometry, inlet configuration and external forcing jointly control water exchange and residence times, how these controls translate into patterns of exposure and vulnerability, and to what extent the proposed framework can support management and emergency response in semi-enclosed coastal environments. Finally, the implications and limitations of the methodology are discussed, together with perspectives for its extension to other sites and to more complex source terms and processes.

7.1 Narta Lagoon

Understanding the water exchange between the Narta Lagoon and the Adriatic Sea is fundamental to evaluate the lagoon's hydrodynamics and, by extension, the health of its ecosystem. Water exchange is a key driver of water quality, facilitating the removal of excess nutrients, pollutants, and suspended matter. These processes are critical for maintaining the ecological balance that supports the lagoon's diverse bird, fish, and aquatic communities.

Even though manually operated sluice gates act as a barrier to regular exchange, in this study, numerical simulations are based on an open-channels configuration and used to assess the lagoon's renewal capacity. The analysis of water level correlations between the inner lagoon and the open sea showed that tidal signals are barely transmitted into the lagoon (Section 4.1.2), suggesting that tidal forcing plays a minor role in the lagoon's internal circulation. Unlike systems where tidal prisms promote efficient flushing (e.g., the Venice Lagoon (Sarretta et al., 2010)), coherently with other semi-enclosed bays (Cáceres-Euse, Morales-Márquez, and Molcard, 2014; Boutron et al., 2015), Narta's exchange is dictated by wind forcing. Our results indicate that under moderate-to-high wind conditions, the lagoon acts as a retentive basin, with eddy structures that are short-lived (∼24h) but spatially extensive. This retentive behaviour aligns with findings in other Mediterranean lagoons with restricted inlets, such as Mar Menor (García-Pintado et al., 2007), where limited water renewal exacerbates the impact of nutrient inputs. Conversely, systems like Étang de Thau benefit from configurations that facilitate higher exchange, demonstrating that inlet geometry—rather than just total lagoon area—is the primary control on resilience to eutrophication. Both the low discharge rates and the restricted particle export observed across multiple scenarios (§4.1) point to a highly retentive system. This raises significant concerns about the vulnerability of the lagoon to water quality degradation, particularly in the event of contaminant or nutrient inputs.

Simulations of a discharge in correspondence with the sewage outfall further show that the behaviour of the plume is strongly scenario-dependent, even when focusing on a relatively small release area. The spatial distribution of absolute dispersion exhibits contrasting patterns in the two scenarios analysed. In scenario 01, there is a clear separation between plume-core pathways, where particles are efficiently advected away from the source, and subregions that behave almost as stagnation zones. In scenario 03, by contrast, the dispersion pattern is more scattered and less clearly organized. The separation between advection and spreading, indicates that whenever sensitivity to release timing is observed, it is primarily controlled by the advective component of the flow.

These hydrodynamic features have clear ecological implications, which align with observations in other Mediterranean lagoon systems. The limited water exchange observed in the Narta Lagoon implies long residence times for nutrients and contaminants, which can promote eutrophic conditions. In such systems, elevated nutrient concentrations, particularly nitrogen and phosphorus, can trigger excessive primary production, often resulting in harmful algal blooms. These blooms deplete oxygen in the water column during decomposition phases, leading to hypoxic or anoxic conditions detrimental to fish and benthic fauna (e.g., Kane et al., 2015; Jones et al., 2024). Moreover, limited flushing reduces the system's capacity to recover from pollution events, increasing its ecological sensitivity to seasonal runoff or sewage inputs. These processes may result in habitat degradation, biodiversity loss, and the disruption of migratory bird routes and spawning grounds.

The patterns observed in Narta are consistent with findings in other Mediterranean lagoons exhibiting low tidal ranges and restricted inlets. For instance, the Mar Menor in Spain has experienced severe eutrophication due to nutrient accumulation from agricultural runoff and limited water renewal, leading to substantial ecological degradation (García-Pintado et al., 2007). Similarly, the Venice Lagoon in Italy, despite its larger size and multiple inlets, faces challenges with water quality and habitat loss, exacerbated by anthropogenic pressures (Sarretta et al., 2010). In contrast, lagoons like the Étang de Thau in France and the Orbetello Lagoon in Italy, which benefit from more effective water exchange mechanisms, have demonstrated greater resilience to nutrient loading and better maintenance of ecological balance (Zannella et al., 2007; Derolez et al., 2020). These comparisons emphasize the importance of hydrodynamic connectivity in sustaining lagoon health and resilience.

The findings of this study emphasize the fragile equilibrium that characterizes the Narta Lagoon. Without sufficient flushing and with irregular channel management, the lagoon is especially sensitive to external pressures. This underscores the urgent need for improved monitoring, consistent management practices, and protective policies aimed at preserving the ecological function and services of the lagoon.

While this study provides new insights into the hydrodynamic functioning of the Narta Lagoon, some limitations must be acknowledged. The present modeling effort has not yet undergone validation against in situ velocity or flow measurements, which would be essential to fully assess the accuracy of the simulated circulation fields and particle trajectories. Another limitation is the absence of salinity-driven density gradients in the model. This barotropic approximation neglects baroclinic effects, which can play a significant role in vertical stratification and water exchange, especially under high evaporation conditions (Kankara and Panda, 2020; Huang et al., 2020). Additionally, the inlet configurations in the simulations assume idealized open channels, whereas in reality, the sluice gates and sedimentation processes cause partial or intermittent closure, which likely reduces the actual water exchange.

In the plume-like discharge simulations the lagoon is considered as closed, simply cutting-off the offshore and inlet cells. This approach provides a first-order approximation of a closed-lagoon configuration and demonstrates that inlets act as sink for particles passing nearby. A fully consistent treatment would require re-running the hydrodynamic model with modified boundary conditions, but this is expected to produce only minor changes to the interior circulation given the already very weak hydraulic connectivity.

Despite these limitations, the modeling framework presented here offers a robust baseline for understanding key hydrodynamic processes and sets the stage for more detailed and validated future studies.

7.2 Port of Genoa

This Port of Genoa study proposes a comprehensive methodology to quantify the exchange of particles between a port and the open sea both in terms of passive tracers and oil and HNS substances, in order to both characterize the flow dynamics driving the exchange and support rapid response in case of spills.

A new clustering method is developed to condense a long hindcast into a small number of wave-driven scenarios. By construction, scenarios are centered on storm peaks, capturing build-up and decay. Although regional currents are relatively steady in the domain, they still show seasonal variability; incorporating large-scale circulation into the clustering could further improve representativeness. To date, validation relies mainly on water levels at a single location inside the port; broader validation against in-situ current measurements (when available) would strengthen confidence in simulated circulation and transport pathways.

A critical component of this framework is the explicit inclusion of windage in the advection equation. As previously noted, floating matter does not move solely with the Eulerian surface current; it is subject to direct aerodynamic drag. The effect of wind in surface transport is taken into account only for the oil and HNS simulations. Windage coefficient is calibrated with drifter data, yielding a best estimate $C_d = 0.02$. The calibration underscores the importance of accurate wind fields in a geometrically complex port. In these terms, a key limitation is the wind forcing, which is taken in a point inside the port: as the trajectory comparisons in Figure 5.3 show, some scenarios are not well reproduced, leading to lower scores (Figure 5.4). Moreover, drifter experiments are performed in calm conditions; therefore, the calibrated C_d should be considered valid primarily for low sea states. Additional, deployments under moderate–strong winds and during storm conditions are needed to test stability of C_d across regimes.

7.2.1 Passive Tracers

Surface Lagrangian dispersion simulations are carried out for 23 representative metocean scenarios, capturing the hydrodynamic variability in the port of Genoa. For each scenario, approximately 22,000 virtual particles are uniformly released within the port, and their trajectories are computed by solving the advection–diffusion equation, both with and without a slip boundary condition.

The analysis of particles leaving the port through its main gates reveal that the complex geometry of the harbor strongly limits exchange with the outer sea. Only about 8% of particles exit under the no-slip condition, and 14% under the slip condition, confirming that the presence of docks, breakwaters, and inner basins effectively traps most of the released material. Re-entrainment (particles exiting and subsequently re-entering the port) is not explicitly quantified, but visual inspection of particle animations suggests that its contribution is negligible; nonetheless, future analyses could incorporate this aspect for completeness.

The Hazard and minimum Estimated Time of Arrival (ETA) maps integrate all 23 scenarios into two synthetic indicators that identify the coastal areas most exposed to pollution originating from the port. Both metrics consistently highlight the sector west of the harbor (around 8.75°E, 44.415°N) as the region most prone to contamination after 48–96 hours from release. This finding aligns with the persistent anti-cyclonic circulation of the Ligurian Sea, which tends to advect surface material westward. Combined with a coastal vulnerability framework, the Hazard and ETA maps form a valuable basis for future integrated risk assessments of port-related pollution.

The Renewal Time analysis measures the time is takes to particles inside the port to leave it, quantifying the ability of the port to renew its water. For the scenario 01 taken as example, the map shows low values for the Airport Channel, while the rest of the port takes days and most of it more of the week analysed to renew its water.

To further interpret the underlying transport dynamics, both single- and multiple-particle statistics are applied, considering particles either as a single ensemble or grouped by release sub-domain. Only scenario 01, the most frequent one, is taken as example. The absence of significant differences across sub-domains indicates that, within the port, mixing is spatially homogeneous. However, clear differences emerge when comparing particles that remain inside the port (IN) with those that escape (OUT).

The velocity autocorrelation exhibit a mild but persistent anti-correlation, indicative of frequent velocity reversals. This behavior reflects the confined and irregular geometry of the basins, where particles repeatedly turn or retrace their paths.

The absolute dispersion analysis highlights distinct regimes for particles IN and OUT. Inside the port, dispersion rapidly reaches a plateau, displaying sub-diffusive behavior typical of confinement-limited transport and trapping in basins. In contrast, particles that exit the port exhibit intermittent bursts of super-diffusive growth, associated with rapid advection along preferential outflow pathways. Even though, in the analyzed scenario, most particles remain inside the port, the mean absolute dispersion (A^2, blue line in the top panel of Figure 6.6) primarily reflects the behavior of the fraction of particles that leave the port. Since A^2 is distance-based, escaping particles contribute disproportionately and therefore dominate the overall slope of the curve, even if they represent only a minority of the releases. This highlights that A^2 can be misleading if interpreted without proper context (e.g., without separating retained vs. escaping particles).

The relative diffusivity confirm the spatially heterogeneous nature of dispersion both inside and outside the port. The $K(r)$ curves for OUT particles saturate well below the full model scale ($\approx$ 30 km), suggesting that beyond the port, particles are advected coherently within narrow outflow filaments, without developing large-scale isotropic mixing. This indicates that the outer circulation maintains a partially coherent, filamented structure rather than a fully turbulent field.

Finally, the Finite-Size Lyapunov Exponent (FSLE) analysis reveal that velocity gradients and small-scale unsteadiness dominate pair separation at short distances, while larger separations reflect smoother strain and flow heterogeneity. The observed oscillations at intermediate separations (400–800 m) point to a transition zone where pairs are simultaneously influenced by inner-port recirculations, harbor outflows, and nearshore circulation, further confirming the coexistence of multiple dynamic regimes.

Overall, this multi-scale Lagrangian approach provides a detailed picture of transport and retention dynamics within a semi-enclosed port environment. Future work should extend these analyses by: (i) releasing particles at multiple times within each weekly scenario to better represent the temporal variability of the hydrodynamics, (ii) including vertical dispersion to assess the influence of stratification, (iii) including wind drag and wave Stokes drift contributions.

7.2.2 Oil and HNS

Simulations of spills at high-risk locations within the Port of Genoa show that weathering processes strongly control dispersion. Many simulated oils and HNS either evaporate or adhere to port structures, often remaining within the harbour and potentially impacting local ecosystems. These results are specific to the tested spill configurations, but the main operational outcome remains: the scenario-based framework provides 23 high-resolution surface velocity fields that can be used to rapidly run spill simulations under a wide range of metocean conditions.

The contribution of wind to surface oil and HNS dispersion is included in the advection term, but the simulations used to calibrate C_d are based on neutrally buoyant virtual particles constrained to follow the surface currents, rather than on observed oil slicks or HNS plumes. This makes the calibrated wind drag most appropriate for passive, surface-following tracers. In the absence of substance-specific data for oil and HNS, however, the same value of C_d is adopted here as a first-order estimate of the wind contribution to their transport, with the explicit caveat that these substances do not behave identically to drifters.

From a contingency planning perspective, the results emphasise that many spills released at accident-prone locations tend to remain confined within the inner basins for time scales of days, even under relatively energetic conditions. In such cases, natural flushing plays a secondary role compared to local retention and weathering, implying that in-port containment and recovery should be prioritised over relying on export to the open sea. The Hazard and minimum Estimated Time of Arrival maps derived from the ensemble of scenarios highlight a limited number of preferential export pathways and coastal sectors at risk, providing a useful basis for pre-positioning response resources and designing contingency plans.

At the same time, several limitations must be acknowledged. The simulations are essentially two-dimensional and focus on surface transport, neglecting vertical stratification and depth-dependent processes such as sinking or resuspension. Moreover, the use of a single, drifter-based wind drag coefficient for all substances and sea states necessarily simplifies the problem. Future work should therefore aim to incorporate three-dimensional transport, product-specific weathering and, where possible, targeted field experiments with controlled releases to better constrain substance-dependent parameters. In addition, the sensitivity of spill behaviour to seasonal temperature should be investigated by varying air and water temperatures within realistic annual ranges.

Chapter 8

Conclusions

This thesis developed and applied an integrated, scenario-based hydrodynamic and Lagrangian modeling framework to two contrasting semi-enclosed coastal systems: Narta Lagoon and the Port of Genoa. Despite their differences in morphology, forcing regimes and management priorities, both systems are characterized by a limited exchange of water with the open sea, which strongly controls their ecological functioning and their vulnerability to pollutant accumulation. By combining a 40-year metocean hindcast, high-resolution Delft3D simulations and Lagrangian particle tracking, the work quantifies how circulation patterns, water exchange and retention shape transport processes in these environments.

For Narta Lagoon, the results reveal an extremely weak connectivity with the Adriatic Sea. Tidal signals are only marginally transmitted into the lagoon, and water renewal is largely driven by wind stress. Numerical experiments show very low flushing rates, with most particles remaining trapped inside the lagoon, particularly under energetic wind conditions. Simulations of a discharge in the south-eastern part of the lagoon show accumulation areas along the boundaries and the sensitivity of dispersal behaviors to the releasing times.

These findings point to a system highly prone to pollutant retention and water quality degradation, especially under current anthropogenic pressures such as irregular inlet management and untreated urban discharges. The lagoon's ecological balance, and the sustainability of local activities that depend on it, are therefore tightly linked to its limited capacity to exchange water with the open sea.

In the Port of Genoa, the analysis of mixing properties reveals heterogeneous transport regimes both inside and outside the port, while the Lagrangian framework is extended to simulate the dispersion of routine operational spills of oil and hazardous and noxious substances (HNS). The analysis shows that releases at accident-prone locations frequently remain within the harbor, where the interaction between complex port geometry and circulation promotes retention. Two mechanisms dominate the fate of oil-like pollutants in the tested configurations: evaporation, which removes a substantial fraction of material, and enhanced trapping due to port structures. Although these findings depend on the specific products and parameterisations used, they underline the need to prioritise in-port containment and shoreline protection in preparedness strategies. The framework delivers pre-computed hazard and ETA maps that can be used to design and refine port contingency plans. A calibration of the wind drag coefficient against drifter trajectories, performed through Bayesian optimisation, yields a best estimate of $C_d = 0.02$ under mild sea-state conditions inside the port, underscoring the importance of accurate wind forcing in sheltered, geometrically complex basins.

Beyond the specifics of each case study, the thesis demonstrates that a library of representative metocean scenarios, derived through clustering of long-term hindcast, can effectively support many management-oriented questions in semi-enclosed basins. This approach captures the essential variability of forcing while remaining computationally affordable and suitable for rapid-response applications. The same workflow, from forcing selection to hydrodynamic–Lagrangian simulations and statistical post-processing, is directly transferable to other lagoons, ports, or estuarine embayments where water renewal and pollutant retention are critical concerns.

The results have clear management implications. For Narta Lagoon, the findings support actions aimed at improving water exchange, such as more regular and ecologically informed inlet operation and, where feasible, optimisation or restoration of channel morphology. These measures should be complemented by stricter control of pollutant inputs and the establishment of a long-term monitoring network for water level and key water quality indicators. For the Port of Genoa, the strong in-port retention of spills emphasises the need to prioritise rapid containment and cleanup strategies within the harbor, and to integrate hydrodynamic dispersion maps into contingency planning and zoning of high-risk areas.

From a research perspective, several extensions emerge naturally from this work. For Narta Lagoon, future developments should include baroclinic simulations that explicitly account for salinity gradients and seasonal stratification, bio-geochemical modules to represent nutrient and oxygen dynamics and in-situ measurements to validate the models. For the Port of Genoa, further work should incorporate higher-resolution wind fields, expanded validation of currents using instruments such as ADCPs or HF radar, and fully three-dimensional dispersion analyses to capture vertical processes and sedimentation of pollutants. In both systems, extending simulations to explore seasonal and inter-annual variability, as well as climate-driven changes in forcing, would strengthen the framework as a tool for adaptive management.

Overall, this thesis shows that combining scenario-based hydrodynamic modeling with Lagrangian dispersion and targeted statistical diagnostics provides a powerful and flexible approach to assess transport, retention and exposure in semi-enclosed coastal basins. The methodology bridges the gap between process-based numerical modeling and management needs, offering a practical pathway to support evidence-based management and emergency response in vulnerable coastal environments.

Bibliography

Abascal, A.J. et al. (2007). “TESEO, an Operational System for Simulating Oil Spills Trajectories and Fate Processes”. In: *Proceedings of Seventeenth International Offshore Ocean and Polar Engineering Conference*.

Abascal, A.J. et al. (2010). “Analysis of the reliability of a statistical oil spill response model”. In: *Marine Pollution Bulletin* 60.11. DOI: `https://doi.org/10.1016/j.marpolbul.2010.07.008`.

Abascal, A.J. et al. (2017a). “A high-resolution operational forecast system for oil spill response in Belfast Lough”. In: *Marine Pollution Bulletin* 114. DOI: `https://doi.org/10.1016/j.marpolbul.2016.09.042`.

Abascal, A.J. et al. (2017b). “Operational oil spill trajectory modelling using HF radar currents: a northwest European continental shelf case study”. In: *Marine Pollution Bulletin* 119. DOI: `https://doi.org/10.1016/j.marpolbul.2017.04.010`.

Abreu, D.T.M.P. de et al. (2019). “Accidents in Seaports: An Analysis from the Perspective of System Dynamics”. In: *European Safety and Reliability Association*. DOI: `10.3850/978-981-11-2724-3_0577-cd`.

Ainsworth C.H. Chassignet, E.P. et al. (2021). “Ten years of modeling the Deepwater Horizon oil spill”. In: *Environmental Modelling Software* 142. DOI: `https://doi.org/10.1016/j.envsoft.2021.105070`.

Alba, Javier García et al. (Feb. 2014). “Hydrodynamic modelling of a regulated Mediterranean coastal lagoon, the Albufera of Valencia (Spain)”. In: *Journal of Hydroinformatics* 16.5, pp. 1062–1076. ISSN: 1464-7141. DOI: `10.2166/hydro.2014.071`.

Allen, J.I., P.J. Somerfield, and F.J. Gilbert (2007). “Quantifying uncertainty in high-resolution coupled hydrodynamic-ecosystem models”. In: *Journal of Marine Systems* 64.1. Contributions from Advances in Marine Ecosystem Modelling Research, 27-29 June, 2005, Plymouth, UK, pp. 3–14. ISSN: 0924-7963. DOI: `https://doi.org/10.1016/j.jmarsys.2006.02.010`.

Artale, V. et al. (1997). “Dispersion of passive tracers in close basins: beyond the diffusion coefficient”. In: *Physics of fluids* 9.11, pp. 3162–3171.

Beqaj, B. (2023). “Evaluation of Water Quality Parameters for Narta Lagoon”. In: *European Journal of Engineering and Technology Research* 8.1, pp. 41–45. DOI: `10.24018/ejeng.2023.8.1.2945`.

Boutron, O. et al. (2015). “An Unstructured Numerical Model to Study Wind-Driven Circulation Patterns in a Managed Coastal Mediterranean Wetland: The Vaccarès Lagoon System”. In: *Water* 7.11. DOI: `https://doi.org/10.3390/w7115986`.

Camus, Paula et al. (2011). “Analysis of clustering and selection algorithms for the study of multivariate wave climate”. In: *Coastal Engineering* 58.6, pp. 453–462.

Casella, Elisa, Giovanni Scicchitano, and Alessio Rovere (2024). “Accuracy and Precision of Shallow-Water Photogrammetry from the Sea Surface”. In: *Remote Sensing* 16.22. ISSN: 2072-4292. DOI: `10.3390/rs16224321`.

Cassola, F., F. Ferrari, and F. Mazzino (2015). “Numerical simulations of Mediterranean heavy precipitation events with the WRF model: analysis of the sensitivity to resolution and microphysics parameterization schemes”. In: *Atmospheric Research* 164-165, pp. 210–225.

Castellari, S., N. Pinardi, and K. Leaman (2000). “Simulation of water mass formation processes in the Mediterranean Sea: Influence of the time frequency of the atmospheric forcing”. In: *Journal of Geophysical Research: Oceans* 105.C10, 24157 – 24181. DOI: https://doi.org/10.1029/2000jc900055.

Cavaleri, Luigi et al. (2022). “The 29 October 2018 storm in Northern Italy: Its multiple actions in the Ligurian Sea”. In: *Progress in Oceanography* 201, p. 102715. ISSN: 0079-6611. DOI: https://doi.org/10.1016/j.pocean.2021.102715.

Chang, Yu-Lin and Lie-Yauw Oey (2014). “Analysis of STCC eddies using the Okubo–Weiss parameter on model and satellite data”. In: *Ocean Dynamics* 64. DOI: 10.1007/s10236-013-0680-7.

Chen, J. et al. (2019). “Oil spills from global tankers: status review and future governance”. In: *Journal of Cleaner Production* 227. DOI: 10.1016/j.jclepro.2019.04.020.

Corrales-Gonzalez, M., G. Lavidas, and G. Besio (2023). “Feasibility of Wave Energy Harvesting in the Ligurian Sea, Italy”. In: *Sustainability*. DOI: https://doi.org/10.3390/su15119113.

Cucco, A. et al. (2012). “A high-resolution real-time forecasting system for predicting the fate of oil spills in the Strait of Bonifacio (western Mediterranean Sea)”. In: *Marine Pollution Bulletin* 64. DOI: https://doi.org/10.1016/j.marpolbul.2012.03.019.

Cullaj, Alqiviadh et al. (2005). “The quality of Albanian natural waters and the human impact”. In: *Environment International* 31.1, pp. 133–146. ISSN: 0160-4120. DOI: https://doi.org/10.1016/j.envint.2004.06.008. URL: https://www.sciencedirect.com/science/article/pii/S0160412004001114.

Cáceres-Euse, A., V. Morales-Márquez, and A. Molcard (2014). “On the Observed Wind-Driven Circulation Response in Small Semienclosed Bays”. In: *American Metheorological Society*. DOI: https://doi.org/10.1175/JPO-D-22-0224.1.

Daliri, M. et al. (2025). “From hindcast to forecast: A statistical framework for real-time coastal circulation bulletins in the Gulf of Genoa”. In: *Applied Ocean Research* 154. DOI: https://doi.org/10.1016/j.apor.2024.104337.

D’Alpaos, Chiara and Andrea D’Alpaos (2021). “The Valuation of Ecosystem Services in the Venice Lagoon: A Multicriteria Approach”. In: *Sustainability* 13.22. DOI: 10.3390/su13179485.

Darbra, R.M. and J. Casal (2004). “Historical analysis of accidents in seaports”. In: *Safety Science* 42. DOI: https://doi.org/10.1016/S0925-7535(03)00002-X.

Delandmeter, P and E. Van Sebille (2019). “The Parcels v2.0 Lagrangian framework: new field interpolation schemes”. In: *European Geosciences Union* 12.8. DOI: https://doi.org/10.5194/gmd-12-3571-2019.

Delft-Hydraulics (2007). *Delft3D-FLOW User Manual Version 3.14*. Deltares.

Derolez, V. et al. (2020). “Fifty years of ecological changes: Regime shifts and drivers in a coastal Mediterranean lagoon during oligotrophication”. In: *Science of The Total Environment* 732, pp. 934–949. DOI: https://doi.org/10.1016/j.csr.2009.07.002.

Egbert, Gary D. and Svetlana Y. Erofeeva (2002). “Efficient Inverse Modeling of Barotropic Ocean Tides”. In: *Journal of Atmospheric and Oceanic Technology* 19.2, pp. 183 –204. DOI: 10.1175/1520-0426(2002)019<0183:EIMOBO>2.0.CO;2.

El Mahrad, Badr, Alice Newton, and Nicholas Murray (2022). “Coastal lagoons: important ecosystems”. In: *Front. Young Minds* 10, p. 637578.

Elmazi, Liljana and Evelina Bazini (2011). “Biodiversity and actual status of Narta and Dukati lagoons in Albania”. In: *Environmental Earth Sciences*, 51 – 60. DOI: 10.1007/978-3-540-95991-5-5.

EMSA (2025). "TAnnual Overview of Marine Casualties and Incidents 2025". In: *EMSA Report*. DOI: https://www.emsa.europa.eu/publications/item/5562-annual-overview-of-marine-casualties-and-incidents-2025.html.

Escudier, R. et al. (2021). "High Resolution Reanalysis for the Mediterranean Sea". In: *Frontiers in Earth Science* 9. DOI: 10.3389/feart.2021.702285.

Ferrari, F. et al. (2024). "The role of atmospheric aerosols on severe convective precipitation in a Mediterranean coastal region". In: *Atmospheric Research* 305. DOI: https://doi.org/10.1016/j.atmosres.2024.107421.

Ferrari, Francesco et al. (2020). "Impact of Model Resolution and Initial/Boundary Conditions in Forecasting Flood-Causing Precipitations". In: *Atmosphere* 11.6. DOI: 10.3390/atmos11060592.

Fiandrino, Annie et al. (2017). "Spatial patterns in coastal lagoons related to the hydrodynamics of seawater intrusion". In: *Marine Pollution Bulletin* 119.1, pp. 132–144. ISSN: 0025-326X. DOI: https://doi.org/10.1016/j.marpolbul.2017.03.006.

Fraschetti, Simonetta et al. (Dec. 2011). "Effects of Unplanned Development on Marine Biodiversity: A Lesson from Albania (Central Mediterranean Sea)". In: *Journal of Coastal Research* 2011.58. _eprint: https://meridian.allenpress.com/jcr/article-pdf/doi/10.2112/SI_58_10/2628435/si_58_10.pdf, pp. 106–115. ISSN: 0749-0208. DOI: 10.2112/SI_58_10. URL: https://doi.org/10.2112/SI_58_10.

French-McCay, D.P. et al. (2021). "Validation of Oil Trajectory and Fate Modeling of the Deepwater Horizon Oil Spill". In: *Frontiers* 8. DOI: https://doi.org/10.3389/fmars.2021.618463.

García-Pintado, J. et al. (2007). "Anthropogenic nutrient sources and loads from a Mediterranean catchment into a coastal lagoon: Mar Menor, Spain". In: *Science of The Total Environment* 373, pp. 220–239. DOI: https://doi.org/10.1016/j.scitotenv.2006.10.046.

Gaspar, P and M. Lalire (2017). "A model for simulating the active dispersal of juvenile sea turtles with a case study on western Pacific leatherback turtles". In: *PlosOne*. DOI: https://doi.org/10.1371/journal.pone.0181595.

GEBCO, Compilation Group (2024). "GEBCO 2024 Grid". In: DOI: 10.5285/1c44ce99-0a0d-5f4f-e063-7086abc0ea0f.

Guarnieri, A. et al. (2013). "Impact of tides in a baroclinic circulation model of the Adriatic Sea". In: *Journal of Geophysical Research: Oceans* 118.1, pp. 166–183. DOI: https://doi.org/10.1029/2012JC007921.

Hardesty, D.B. et al. (2017). "Using Numerical Model Simulations to Improve the Understanding of Micro-plastic Distribution and Pathways in the Marine Environment". In: *Frontiers* 4. DOI: https://doi.org/10.3389/fmars.2017.00030.

He, C. et al. (2024). "Environmental risk assessment of coastal dredging based on clustering of meteocean forcing". In: *Coastal Engineering* 192. DOI: https://doi.org/10.1016/j.coastaleng.2024.104555.

Huang, P. et al. (2020). "Climate change overtakes coastal engineering as the dominant driver of hydrological change in a large shallow lagoon". In: *Hydrology and Earth System Sciences* 24, 5673–5697. DOI: https://doi.org/10.5194/hess-24-5673-2020.

Huck, T. et al. (2022). "Three-Dimensional Dispersion of Neutral "Plastic" Particles in a Global Ocean Model". In: *Frontiers* 2. DOI: https://doi.org/10.3389/frans.2022.868515.

Iacono, Roberto and Ernesto Napolitano (2020). "Aspects of the summer circulation in the eastern Ligurian Sea". In: *Deep Sea Research Part I: Oceanographic Research Papers* 166. DOI: https://doi.org/10.1016/j.dsr.2020.103407.

Jones, A.G. et al. (2024). “Disentangling the effects of eutrophication and natural variability on macrobenthic communities across French coastal lagoons”. In: *Peer Community Journal* 4. DOI: `https://doi.org/10.24072/pcjournal.499`.

Kane, Sonila et al. (2015). “Assessment of environmental situation of Narta and Orikumi lagoon, Albania”. In: *Fres. Environ. Bull* 24.9, pp. 2975–2984.

Kankara, R.S. and U.S. Panda (2020). “Modelling of Hydrodynamics and Salinity Characteristics in Chilika Lagoon”. In: *Wetlands: Ecology, Conservation and Management*. DOI: `https://doi.org/10.1007/978-3-030-33424-6_6`.

Kareem, Kola Yusuff et al. (2022). “A Case Study of Tidal Analysis Using Theory-Based Artificial Intelligence Techniques for Disaster Management in Taehwa River, South Korea”. In: *Water* 14.14. DOI: `10.3390/w14142172`.

Kjerfve, Björn and K.E Magill (1989). “Geographic and hydrodynamic characteristics of shallow coastal lagoons”. In: *Marine Geology* 88.3, pp. 187–199. ISSN: 0025-3227. DOI: `https://doi.org/10.1016/0025-3227(89)90097-2`.

LaCasce, J.H. (2008). “Statistics from Lagrangian observations”. In: *Progress in Oceanography* 77, 1Â–29.

Lambert, Maya and Sebastián Solari (2022). “Hydrodynamic Modelling of an Intermittently Closed and Open Lagoon”. In: *Proceedings of the IAHR World Congress*, 5517 – 5525. DOI: `10.3850/IAHR-39WC2521716X2022342`.

Launder, B.E. and D.B. Spalding (1974). “The Numerical Computation of Turbulent Flows”. In: *Computer Methods in Applied Mechanics and Engineering* 3.2. DOI: `https://doi.org/10.1016/0045-7825(74)90029-2`.

Le Gouvello, D.Z.M. et al. (2024). “Dispersal corridors of neonate sea turtles from dominant rookeries in the Western Indian Ocean”. In: *Ecological Modelling* 487. DOI: `https://doi.org/10.1016/j.ecolmodel.2023.110542`.

Lehodey, P., I. Senina, and R. Murtugudde (2008). “A spatial ecosystem and populations dynamics model (SEAPODYM) – Modeling of tuna and tuna-like populations”. In: *Progress in Oceanography* 78. DOI: `https://doi.org/10.1016/j.pocean.2008.06.004`.

Lesser, G.R. et al. (2004). “Development and validation of a three-dimensional morphological model”. In: *Coastal Engineering* 51.8. Coastal Morphodynamic Modeling, pp. 883–915. ISSN: 0378-3839. DOI: `https://doi.org/10.1016/j.coastaleng.2004.07.014`.

Lira-Loarca, Andrea et al. (2022). “Wave modeling with unstructured mesh for hindcast, forecast and wave hazard applications in the Mediterranean Sea”. In: *Applied Ocean Research* 122, p. 103118. ISSN: 0141-1187. DOI: `https://doi.org/10.1016/j.apor.2022.103118`.

Liu, Yonggang and Robert H. Weisberg (2011). “Evaluation of trajectory modeling in different dynamic regions using normalized cumulative Lagrangian separation”. In: *Journal of Geophysical Research* 116. DOI: `https://doi.org/10.1029/2010JC006837`.

Liubartseva, S. et al. (2021). “Oil spill risk assessment for a Single Buoy Mooring terminal in the Port of Taranto (Southern Italy)”. In: *EGU General Assembly 2021*. DOI: `10.5194/egusphere-egu21-4662`.

Lozanos, Carlos J. and Julio Canela (1995). “The M2 tide in the Mediterranean Sea: dynamic analysis and data assimilation”. In: *Oceanologica Acta* 18.

Mackay, D. and P.J. Leinonen (1977). “Mathematical Model of the Behaviour of Oil Spills on Water with Natural and Chemical Dispersion”. In: *Rapport technique n° EPS-3-EC-77-19, Fisheries and Environmental Canada*.

Manzella, G. and A. Esposito (1982). “Current Circulation in the Ligurian Sea”. In: *Elsevier Oceanography Series* 114. DOI: `10.1016/S0422-9894(08)71245-5`.

Maréchal, David (2004). “A soil-based approach to rainfall-runoff modelling in ungauged catchments for England and Wales”. In.

Martín, M. et al. (2020). “Fifty years of eutrophication in the Albufera lake (Valencia, Spain): Causes, evolution and remediation strategies”. In: *Water Resources Research* 155. DOI: `10.1016/j.ecoleng.2020.105932`.

Mentaschi, L. et al. (2013). “Implementation and validation of a wave hindcast/forecast model for the West Mediterrenean”. In: *Proc of: 2th International Coastal Symposium*. Plymouth, UK.

Mladenov, Vladimir et al. (2017). “Breeding birds in the Narta Lagoon (SW Albania) in 2016”. In: *Acrocephalus* 39.176-177, pp. 7–25. DOI: `https://doi.org/10.1515/acro-2018-0001`.

Molcard, A. et al. (2002). “Wind driven general circulation of the Mediterranean Sea simulated with a Spectral Element Ocean Model”. In: *Dynamics of Atmospheres and Oceans* 35.2, pp. 97–130. ISSN: 0377-0265. DOI: `https://doi.org/10.1016/S0377-0265(01)00080-X`.

Neumann, B. et al. (2015). “Future Coastal Population Growth and Exposure to Sea-Level Rise and Coastal Flooding - A Global Assessment”. In: *PLOS ONE*. DOI: `https://doi.org/10.1371/journal.pone.0118571`.

Newton, Alice et al. (2018). “Assessing, quantifying and valuing the ecosystem services of coastal lagoons”. In: *Journal for Nature Conservation* 44, pp. 50–65. ISSN: 1617-1381. DOI: `https://doi.org/10.1016/j.jnc.2018.02.009`.

Núñez, P. et al. (2019). “A methodology to assess the probability of marine litter accumulation in estuaries”. In: *Marine Pollution Bulletin* 114. DOI: `https://doi.org/10.1016/j.marpolbul.2019.04.077`.

Palatella, L. et al. (2014). “Lagrangian simulations and interannual variability of anchovy egg and larva dispersal in the Sicily Channel”. In: *JGR Oceans*. DOI: `https://doi.org/10.1002/2013JC009384`.

Pisano, A. et al. (2016). “An oceanographic survey for oil spill monitoring and model forecasting validation using remote sensing and in situ data in the Mediterranean Sea”. In: *Deep Sea Research Part II: Topical Studies in Oceanography* 133. DOI: `https://doi.org/10.1016/j.dsr2.2016.02.013`.

Polinov, S., R. Bookman, and N Levin (2021). “Spatial and temporal assessment of oil spills in the Mediterranean Sea”. In: *Marine Pollution Bulletin* 167. DOI: `https://doi.org/10.1016/j.marpolbul.2021.112338`.

Putman, N.F. et al. (2014). “Numerical dispersal simulations and genetics help explain the origin of hawksbill sea turtles in Ascension Island”. In: *Journal of Experimental Marine Biology and Ecology* 450. DOI: `https://doi.org/10.1016/j.jembe.2013.10.026`.

Pérez-Ruzafa, Angel and Marcos Concepción (2012). “Fisheries in coastal lagoons: An assumed but poorly researched aspect of the ecology and functioning of coastal lagoons”. In: *Estuarine, Coastal and Shelf Science* 110. DOI: `https://doi.org/10.1016/j.ecss.2012.05.025`.

Pérez-Ruzafa, Angel et al. (2019). “Coastal Lagoons: Environmental Variability, Ecosystem Complexity, and Goods and Services Uniformity”. In: *Coasts and Estuaries*. Ed. by Eric Wolanski et al. Elsevier, pp. 253–276. ISBN: 978-0-12-814003-1. DOI: `https://doi.org/10.1016/B978-0-12-814003-1.00015-0`.

Raicevich, S. et al. (2018). “Historical ecology of semi-enclosed basins and coastal areas:Past, present and future of seas at risk”. In: *Regional Studies in Marine Science* 21. DOI: `https://doi.org/10.1016/j.rsma.2018.02.007`.

Ramos-Musalem, K. and S.E Allen (2019). “The Impact of Locally Enhanced Vertical Diffusivity on the Cross-Shelf Transport of Tracers Induced by a Submarine

Canyon". In: *American Meteorological Society*. DOI: `https://doi.org/10.1175/JPO-D-18-0174.1`.

Ray, Richard D. and Grant Foster (2016). "Future nuisance flooding at Boston caused by astronomical tides alone". In: *Earth's Future* 4.12, pp. 578–587. DOI: `https://doi.org/10.1002/2016EF000423`.

Sarretta, A. et al. (2010). "Sediment budget in the Lagoon of Venice, Italy". In: *Continental Shelf Research* 30, pp. 934–949. DOI: `https://doi.org/10.1016/j.csr.2009.07.002`.

Stiver, W. and D. Mackay (1984). "Evaporation Rate of Spills of Hydrocarbons and Petroleum Mixtures". In: *Environment Science Technology* 18.11, pp. 834–840.

Stocchino, A. et al. (2011). "Lagrangian mixing in straight compound channel". In: *Journal of Fluid Mechanics* 675, 168–198. DOI: `doi:10.1017/S0022112011000127`. URL: `http://journals.cambridge.org/action/displayAbstract?fromPage=online&aid=8273430`.

SWAN User Manual (2004). "SWAN Cycle III, version 40.41". In: *Delft University of Technology*.

Takeoka, H. (1984). "Exchange and transport time scales in the Seto Inland Sea". In: *Continental Shelf Research* 3.4, pp. 327–341. DOI: `https://doi.org/10.1016/0278-4343(84)90015-3`.

Topi, M., O. Saliaj, and K. Mersinaj (2013). "Preliminary Report for Key Biodiversity Area of Narta Lagoon". In.

Tsujio, D., K. Asano, and S. Hoxha (2024). "Mechanisms of sediment transport and seawater exchange in the Karavasta lagoon, Albania". In: *Proceedings of 38th Conference on Coastal Engineering* (Rome, Italy). 38, p. 14.2.

Umgiesser, Georg et al. (2014). "Comparative hydrodynamics of 10 Mediterranean lagoons by means of numerical modeling". In: *Journal of Geophysical Research: Oceans* 119.4, pp. 2212–2226. DOI: `https://doi.org/10.1002/2013JC009512`.

Van Sebille, E., M.H. England, and G. Froyland (2012). "Origin, dynamics and evolution of ocean garbage patches from observed surface drifters". In: *Environmental Research*. DOI: `10.1088/1748-9326/7/4/044040`.

Vaso, A., A. Miho, and C. Alain (1996). "Characteristics of Albanian lagoons and their fisheris". In: *Fisheries Research* 27.4, pp. 215–225. DOI: `https://doi.org/10.1016/0165-7836(95)00467-X`.

Wang, Y. et al. (2022). "A Lagrangian model-based physical connectivity atlas of the Red Sea coral reefs". In: *Frontiers* 9. DOI: `https://doi.org/10.3389/fmars.2022.925491`.

Warner, John C., W. Rockwell Geyer, and James A. Lerczak (2005). "Numerical modeling of an estuary: A comprehensive skill assessment". In: *Journal of Geophysical Research: Oceans* 110.C5. DOI: `https://doi.org/10.1029/2004JC002691`.

Willmott, Cort J. (1981). In: *Physical Geography* 2.2, pp. 184–194. DOI: `https://doi.org/10.1080/02723646.1981.10642213`.

Zannella, A. et al. (2007). "Hydrodynamics, transport time scales and water temperature dynamics in heavily anthropized eutrophic coastal lagoon". In: *Estuarine, Coastal and Shelf Science* 314. DOI: `https://doi.org/10.1016/j.ecss.2025.109146`.

Ze-Guo Zhang, Jian-Chuan Yin and Cheng Liu (2018). "A Modular Real-time Tidal Prediction Model based on Grey-GMDH Neural Network". In: *Applied Artificial Intelligence* 32.2, pp. 165–185. DOI: `10.1080/08839514.2018.1451220`.

Çako, V. et al. (2014). "Water Transparency As One As Of Trophic State Indices In Narta Lagoon". In: *Journal of engineering* 04, pp. 15–22.

Çomo, E. et al. (2018). “Evaluation of Phisic-Chemical Features of the Main Coastal Lagoons of Narta and Karavasta, in Alabania”. In: *Online International Interdisciplinary Research Journal* 08.